A Measurement of the Neutrino Neutral Current π^0 Cross Section at MiniBooNE

A Dissertation Submitted to the

Office of Research and Advanced Studies
of the University of Cincinnati

in partial fulfillment of the
requirements for the degree of

DOCTORATE OF PHILOSOPHY (Ph.D.)

in the Department of Physics
of the College of Arts and Sciences

2005

by

Jennifer Lynne Raaf

B.S., Virginia Polytechnic Institute & State University, 1997
M.S., University of Cincinnati, 2001

Committee Chair: Professor Randy A. Johnson

Abstract

The MiniBooNE neutrino beam and detector at Fermilab are used to study the production of neutral current π^0 events. The cross sections for neutrino interactions with mineral oil (CH_2) are reported for resonantly produced and coherently produced single π^0 events. We measure a resonant single π^0 cross section of $\sigma(\nu_\mu\,\mathcal{N} \to \nu_\mu\,\mathcal{N}\,\pi^0) = (0.0129 \pm 0.0011(stat.) \pm 0.0043(syst.)) \times 10^{-36}$ cm^2/CH_2 at a mean neutrino energy of 1.26 GeV. We measure a coherent single π^0 cross section of $\sigma(\nu_\mu\,\mathcal{A} \to \nu_\mu\,\mathcal{A}\,\pi^0) = (0.00077 \pm 0.00016\ (stat.) \pm 0.00036\ (syst.)) \times 10^{-36}$ cm^2/CH_2 at mean neutrino energy 1.12 GeV.

Acknowledgements

Well, I can't believe it's finally over. Does this mean I have to become an adult? Thankfully, my mom reassured me that this is not the case: "An adult? Noooo... look at your father!" Mom and Dad, I cannot thank you enough for the support (emotional, and financial) and love that you've given without question over the years. It only took 24 years for me to finally finish school! Think of all the vacations you'll be able to take now that I'll no longer be a drain on your bank account! And what have I learned in all those years? Probably the most important (and possibly the most disappointing) thing is this: a universal remote control does not, in fact, allow you to control the universe. Alas.

To all of my MiniBooNE partners-in-crime. Bonnie Fleming, whose magnificent haiku (sent to me in an email from across the room at the Lab E trailers while she was in the midst of *her* thesis-writing frenzy) deserves an award for so aptly describing the pain involved in actually sitting down to write your thesis:

```
rats in my cortex
feasting on my frontal lobe
ouch. that hurts a lot
```

Sam Zeller, who is probably the only person other than the Pope and Michelangelo to have worn slippers in the Sistine Chapel. And of course I cannot forget the others who were always interested and helpful: Jon Link, Hiro Tanaka, and Eric Hawker. It has been more than a pleasure to work with all of you over these past few years. Thank you for all the help you gave me.

Morgan Wascko and Jocelyn Monroe, or "MoJo" as I like to say (and I'm really hoping that will catch on.... wouldn't it be great if you could jointly be a one-name superstar?). It's always

great when your friends are also good people to work with. You both qualify, and I look forward to working with you again some day. Dave Schmitz. Well, Dave, I can honestly say that I probably wouldn't have made it through all of this without your friendship. I can say, though, that I **definitely** would have finished knitting the second sock, even without your taunting. (The second glove is a different matter... although it *is* half-finished. Maybe you'll get the pair as a birthday present some day in the distant future.) Michel Sorel, who has recently left us for the greener pastures (bluer seas?) of Valencia. Although you've only been gone for a few weeks, the office has felt strangely empty without you. I miss the fun discussions we often had during my second-hand-smoke breaks.

Ryan Patterson: For turning the "picky knob" to eleven when I wanted you to, but also for knowing when to let things slide. And for always knowing the answer immediately when I asked a question about FORTRAN. Chris Cox: As we both know, Maryland is the best state. No matter what anyone else says. Shawn McKenney: for telling such long funny stories I was almost in tears by the end. And, of course, for letting me pretend Bear was my dog...

And to the rest of the MiniBooNE crew: working on this experiment over these last years has been such a great experience. You have all helped me in big and small ways. Thank you.

And then there's Mike Kirby: You accuse me of following you?!?! The way I see it is, you've been copying me. Let's see... first there was that whole "I wanna be a physics major" thing our freshman year... and if you'll recall, *you* were the one who started out in engineering. Then there was the motorcycle purchase. Yes. That's right, **I** got a motorcycle before **you** did (and I'm sure your parents hate me for it). But aside from your blatant mimicry, I must say you've been the all-time best lab partner and friend a girl could have. Thanks for always calming me down after my (embarrassingly frequent) freak-outs and for providing all sorts of entertaining diversions over the years. Dean Hidas, my other motorcycle buddy and ever-willing Roma D's companion. I know you agree with me here... a slice is **more** than just *nice*... And now that you've successfully consumed three slices in one sitting, I guess I'll have to stop picking on you.

And to my good friends from the very beginning of this long, long process: Laurie Robinson, Aditi Sharma, Anuvrat Joshi and Moitreyee Sinha. Thank you for keeping me from quitting! Doug Hott and Jennie Pham. Thank you for always welcoming me into your home. You are always

welcome in mine. I still don't forgive you for dragging me to Graceland though.

Man-Bat (he's not Batman, he's Man-Bat!) for protecting my desk from other arch-villains. Okay, so maybe that was just in my head... but I could have sworn I saw one climbing up the side of Wilson Hall. Check the control room logbook... it's in there.

None of my important paperwork would have gotten finished without the gentle reminders and help I received from Donna Deutenberg and Melody Whitlock. Thank you! And to the UC ninjas-in-residence: John Markus, John Whitaker, and Richard Gass, and to "my shop guys" Bob Schrott, Mark Ankenbauer, and Mark Sabatelli. I know you might think I'm a little bit crazy, but just think how much *more* crazy I'd be if all of you hadn't been around!

And last, but certainly not least, to my advisor, Randy, who continues to vehemently hate split infinitives. (See? That one was good, right? I know you liked it!) Thank you for guiding me on this path, allowing me to be goofy sometimes, and always encouraging me in everything that I've done. You've set a wonderful example, and shown me how to be a good scientist over the years. (And don't even for a second think that just because I'm finally graduating, you're off the hook... I still plan to call and bug you.)

Contents

List of Tables

List of Figures

Chapter 1

Introduction

1.1 Brief History of Neutrinos

Until 1930, neutrinos weren't even a glimmer in the eye of the man who postulated them. It was Wolfgang Pauli who set the gears in motion when he suggested the existence of a weakly interacting neutral particle with the same spin as an electron and very little or no rest mass [1]. This strange proposal was put forth in a self-proclaimed "desperate" attempt to keep the law of energy conservation intact in nuclear beta decay $(n \rightarrow p + e^- + \bar{\nu}_e)$. The outgoing electron in the decay was observed to have a continuous energy spectrum, rather than the distinct energy that is dictated by momentum and energy conservation in a two-body decay. The only logical conclusion was that another particle was involved in the decay. This particle would have to interact with matter extremely weakly in order to explain why it had not been observed in experiments. In 1954, Reines and Cowan provided the first experimental evidence of neutrino-induced interactions [2] by searching successfully for a distinct experimental signature in inverse beta decay $(\bar{\nu} + p \rightarrow n + e^+)$.

In addition to the electron neutrino produced in nuclear beta decay, the existence of two other flavors of neutrino have been verified in the years since. Lederman, Schwartz, and Steinberger discovered in 1963 that the neutrino from pion decay (the muon neutrino) was distinct from the electron neutrino [3]. Tau neutrinos were then discovered by the DONUT experiment at Fermilab in 2000 [4].

After discovery of these particles, the next obvious step was to measure their masses. Exper-

iments which have directly searched for neutrino masses have only been able to set upper limits. The current bounds [5] are

$$m_{\nu_e} \quad < \quad 3 \text{ eV/c}^2,$$
$$m_{\nu_\mu} \quad < \quad 0.19 \text{ MeV/c}^2, \text{ and}$$
$$m_{\nu_\tau} \quad < \quad 18.2 \text{ MeV/c}^2.$$

Since the ν_e is consistent with the massless particle Pauli proposed, massless neutrinos were added to the growing "standard" list of particles. Far from closing the book on neutral leptons, however, further study of neutrinos indicated that they were able to transform from one type to another in a phenomenon known as neutrino oscillations. This was a surprising discovery because oscillations are a quantum mechanical effect that can only occur if the particles involved have non-zero masses. Before discussing massive neutrinos and their behavior, however, we begin with the standard model that was initially used to classify them.

1.2   Neutrinos in the Standard Model

The Standard Model of particle physics was created in an attempt to organize and describe all of the basic constituents of matter and the fundamental forces of nature, unifying the weak and electromagnetic forces. Although this model has proven an almost "unbreakable" framework since its inception, it seems to be missing a few components. It fails to explain, for instance, the hierarchy of the quark and lepton masses and the origin of flavor mixing. Extensions beyond the Standard Model are needed to begin explaining these, and investigations of these extensions are what make the field of experimental particle physics so interesting.

A partial list of particles in the Standard Model is shown in Table 1.1. The model provides an elegant description of the elementary particles and how they interact. The quarks can interact with matter through any of the fundamental forces: strong, weak, or electromagnetic (EM). The leptons do not interact via the strong force. Furthermore, the neutral leptons, or neutrinos, are even more unusual because they also do not interact electromagnetically. Unlike all other elementary particles, the neutrinos interact strictly via the weak force. Neutrino interactions occur through two types of boson exchange; the two gauge bosons which carry the weak force are the W and the Z^0. Exchange of a Z^0 is called a neutral current (NC) interaction, and exchange of a W^+ or W^-

Classification	Particles			Forces
Quarks	$\begin{pmatrix} u \text{ (up)} \\ d \text{ (down)} \end{pmatrix}$	$\begin{pmatrix} c \text{ (charm)} \\ s \text{ (strange)} \end{pmatrix}$	$\begin{pmatrix} t \text{ (top)} \\ b \text{ (bottom)} \end{pmatrix}$	Strong, Weak, EM
Leptons	$\begin{pmatrix} \nu_e \\ e \end{pmatrix}$	$\begin{pmatrix} \nu_\mu \\ \mu \end{pmatrix}$	$\begin{pmatrix} \nu_\tau \\ \tau \end{pmatrix}$	Weak Weak, EM

Table 1.1: A partial list of Standard Model particles with their broad classifications (left column), names (center column, grouped by family), and forces by which they interact (right column).

is called a charged current (CC) interaction. Fig. 1.1 shows a pictorial representation of these two types of neutrino interactions. When a W is emitted from a neutrino vertex, charge conservation at the vertex requires that a charged lepton exit the interaction.
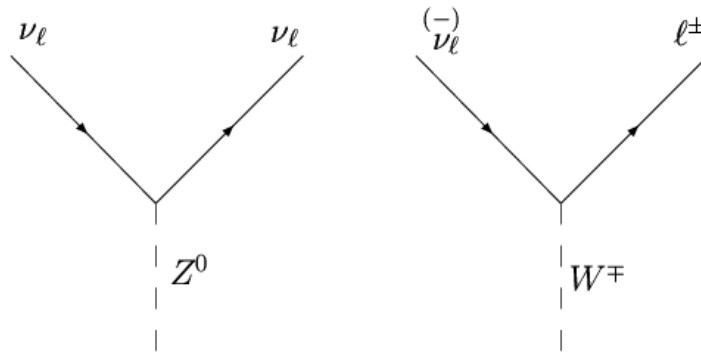
Figure 1.1: The two ways by which neutrinos interact, neutral current (left) and charged current (right) interaction.

In addition to the unusual nature of neutrinos with respect to fundamental forces, another oddity presents itself with these particles: handedness. To understand handedness, we begin by discussing helicity. The quarks and leptons in the Standard Model both fall into the larger category of "fermions," meaning they are all spin 1/2 particles that obey the Pauli principle. For a spin 1/2 particle, helicity is the projection of a particle's spin (σ) along its direction of motion $\hat{\mathbf{p}}$, with operator $\sigma \cdot \hat{\mathbf{p}}$. Helicity has two possible states: spin aligned opposite the direction of motion (negative or "left helicity"), and spin aligned along the direction of motion (positive or "right helicity").

If a particle is massive, then the sign of the particle's helicity is frame dependent. Boosting to a frame which is moving faster than the particle will cause the helicity to flip; the sign of the momentum will change but the spin will not. This is not the case for a massless particle, which travels at the speed of light. In this case, it is impossible to boost to a frame where helicity changes sign.

Handedness is related to helicity. There are two handedness states: "left-handed" (LH) and "right-handed" (RH). The helicity of a particle may be written as a linear combination of its handedness states. In the case of massless particles, including Standard Model neutrinos, handedness is identical to helicity. A massless fermion is either purely LH or RH, and in principle, can appear in either state. Massive particles have both LH and RH components.

The left- and right-handed components of a particle state (ψ) can be projected out using the helicity-projection operators

$$
\begin{aligned}
\psi_{L,R} &= \tfrac{1}{2}(1 \mp \gamma^5)\psi, \text{ and} \\
\bar{\psi}_{L,R} &= \tfrac{1}{2}\bar{\psi}(1 \pm \gamma^5).
\end{aligned}
\tag{1.1}
$$

where the γ matrices are defined as in Ref. [6].

The designation of LH and RH is important because weak interactions only take place between left-handed particle states (or right-handed antiparticle states). Because of this, only LH neutrino states (and RH anti-neutrino states) have been observed experimentally. Neither the strong nor the electromagnetic force has such a restriction; each of these forces interacts equally with LH and RH particle states.

1.3   Neutrino Oscillations and the Origin of their Mass

As mentioned earlier, neutrino flavor oscillations have been observed experimentally. Evidence for these flavor transformations has become stronger in recent years, but oscillations between neutrino flavors can only occur if the neutrinos have non-zero masses. What is the motivation for these masses? How can they be incorporated into the theory?

1.3.1   Neutrino Mass

As the neutrinos have no masses in the Standard Model, it becomes necessary to extend this model to incorporate them. In the Standard Model, the neutrinos, like their charged lepton partners, are classified as Dirac particles (where neutrinos and anti-neutrinos are distinct particles). This is not necessarily true, however; it is also possible that neutrinos and their anti-particles are identical, or Majorana particles. Either way, it is difficult to motivate why this mass should exist.

The charged leptons are assumed to obtain their masses in the same way as the W and Z^0 bosons – through the Higgs mechanism. This is achieved by introducing a spin-zero Higgs doublet (h^0, h^+) to the Lagrangian. While expectation value for the ground state of the h^+ field is zero, the ground state of the h^0 field has a non-zero vacuum expectation value, $< h^0 >= v/\sqrt{2}$. This is the supposed origin of mass. The interaction between the Higgs fields and neutrino and charged lepton is of the form

$$g_\ell \bar{\psi}_\ell^R \left(\psi_\nu^L (h^+)^\dagger + \psi_\ell^L (h^0)^\dagger \right) \tag{1.2}$$

where the Yukawa coupling constant, g_ℓ, describes the strength of the coupling between the Higgs field and the lepton. The second term in Eq. 1.2 is known as the Dirac mass term. It has the form $m\bar{\psi}\psi$, where $m = g_\ell v/\sqrt{2}$. The charged lepton masses in the Standard Model thus arise from the Yukawa interaction of these leptons with the Higgs background.

The same mechanism can be used to give the neutrinos mass, assuming they are Dirac particles like the charged leptons. A Dirac neutrino can be described using four independent states: left-handed and right-handed particles (ν_L and ν_R), and left-handed and right-handed anti-particles ($\bar{\nu}_L$ and $\bar{\nu}_R$). The ν_L and $\bar{\nu}_R$ exist in the Standard Model, interacting through the left-handed weak force. In order to introduce neutrino mass to the model, the missing states (ν_R and $\bar{\nu}_L$) must be included. Although they will "exist" in the sense that they are part of the model, they will be undetectable, or "sterile", because they cannot take part in normal weak interactions. Once the missing states are included, a Dirac mass term ($m\bar{\psi}\psi$) for the neutrino can be added to the Lagrangian. The LH and RH components of the neutrino field are projected out using Eq. 1.1 so

that the Dirac mass term is of the form

$$
\begin{aligned}
\bar{\psi}\psi &= \bar{\psi}\left[\tfrac{1+\gamma^5}{2} + \tfrac{1-\gamma^5}{2}\right]\left[\tfrac{1+\gamma^5}{2} + \tfrac{1-\gamma^5}{2}\right]\psi \\
&= \bar{\psi}_L\psi_R + \bar{\psi}_L\psi_L + \bar{\psi}_R\psi_R + \bar{\psi}_R\psi_L \\
&= \bar{\psi}_L\psi_R + \bar{\psi}_R\psi_L,
\end{aligned}
\tag{1.3}
$$

recalling that $\bar{\psi}_L\psi_L$ and $\bar{\psi}_R\psi_R$ drop out because $(\gamma^5)^2 = 1$. This has the effect of mixing the right- and left-handed states of the neutrino. If no right-handed neutrino exists, the mass term automatically vanishes. In addition, the neutrino mass has the same form as that of its charged lepton partner, $m_\nu = g_\nu v/\sqrt{2}$, but since the vacuum expectation value, v, for neutrinos must be identical to that of the other leptons, the small mass can only be due to a much weaker coupling between the neutrino and the Higgs field.

Another possibility is that the neutrino and anti-neutrino are different helicity states of the same particle, *i.e*, a Majorana particle. Then the field can be described using only two independent particle states (ν_L and $\bar{\nu}_R$, or ν_R and $\bar{\nu}_L$). This neutrino doublet is therefore its own charge conjugate, $\psi^C = \psi$, and a Majorana mass term of the form $m\bar{\psi}\psi^C$ is a natural addition to the Lagrangian. The left- and right-handed components of the field are projected out with

$$
(\psi_{L,R})^C = \frac{1}{2}(1 \pm \gamma^5)\psi^C = (\psi^C)_{R,L}
\tag{1.4}
$$

and there are two Majorana mass terms (one for left-handed neutrinos and one for right-handed neutrinos)

$$
\frac{M_L}{2}\left[\bar{\psi}_L^C\psi_L + \bar{\psi}_L\psi_L^C\right] + \frac{M_R}{2}\left[\bar{\psi}_R^C\psi_R + \bar{\psi}_R\psi_R^C\right].
\tag{1.5}
$$

These terms mix the charge-conjugate pair states of the neutrino. If $\psi^C \neq \psi$, the Majorana mass terms automatically vanish.

The total Dirac+Majorana mass term, which is the Standard Model coupling to the Higgs plus a mass from the added Majorana term, can be rewritten more compactly in matrix form:

$$
\frac{1}{2}\begin{pmatrix} \bar{\psi}_L^C & \bar{\psi}_R \end{pmatrix}\begin{pmatrix} M_L & m \\ m & M_R \end{pmatrix}\begin{pmatrix} \psi_L \\ \psi_R^C \end{pmatrix} + \text{ herm. conj.}
\tag{1.6}
$$

where m is the Dirac mass, and M_L and M_R are the left- and right-handed Majorana masses respectively. In this form, the left- and right-handed fields are coupled by a Dirac mass term, and do not have definite mass. Physical masses, m_1 and m_2, are obtained by diagonalizing the matrix.

The "See-Saw" mechanism [7–9] uses this Dirac+Majorana mass term and provides a reasonably compelling motivation for why the neutrino masses are so much smaller than the masses of the charged leptons. This mechanism considers a case where $M_L = 0$ and $m << M_R$. The diagonalization of the mass matrix yields

$$m_1 \simeq \frac{m^2}{M_R} << m$$
$$m_2 \simeq M_R.$$
(1.7)

Since m is generated by the Higgs mechanism, its mass should be of the same order of magnitude as the charged lepton of the same generation. The suppression of the physical mass state, m_1, is plausible then if m_2 is very large. The light neutrino would correspond to the neutrino currently observed in weak processes, while the heavy neutrino would not be directly observable at low energies [6].

This gives one example of an extension to the Standard Model with massive neutrinos that are Majorana particles, and in which the smallness of the neutrino mass is naturally explained by the See-Saw mechanism. It is unfortunately not a perfectly tidy model though; it is hard to justify why M_R should be so much heavier than m. Many other models, including theories with extra dimensions and grand unified theories, attempt to motivate neutrino mass and add it to the theory in an elegant way, but each of these also has its own caveats. New theories will almost certainly continue to be formulated until such time as the answer is discovered experimentally.

1.3.2 Oscillations

It is necessary to force neutrino masses into a theoretical framework that doesn't want them in order to explain that which has already been observed experimentally – flavor oscillations. If the neutrino mass is acquired through the Higgs mechanism, the mass states are likely mixtures of the weak states, as is seen with quarks. Neutrinos are *produced* in weak eigenstates and *transported* in mass eigenstates. Thus, the weak eigenstates may be written as linear combinations of the mass eigenstates, *i.e.*, a ν_α neutrino eigenstate associated with an α lepton may be written as

$$| \, \nu_\alpha \rangle = \sum_i U_{\alpha i} \, | \, \nu_i \rangle$$
(1.8)

where ν_i are the mass eigenstates and U is a unitary neutrino mass mixing matrix that performs the rotation from the mass eigenstate basis to the weak eigenstate basis. This is analogous to the quark sector, where the mixing is described by the Cabbibo-Kobayashi-Maskawa (CKM) matrix [10, 11].

The mechanics of neutrino oscillations are more clearly demonstrated for the simplified case of two generation mixing. Assuming the neutrinos are Dirac particles with definite mass, the mixing matrix is:

$$
\begin{pmatrix} \nu_e \\ \nu_\mu \end{pmatrix} = \begin{pmatrix} \cos\theta & \sin\theta \\ -\sin\theta & \cos\theta \end{pmatrix} \begin{pmatrix} \nu_1 \\ \nu_2 \end{pmatrix}
\tag{1.9}
$$

where the flavor eigenstates (ν_e and ν_μ) are expressed as a mixture of the mass eigenstates (ν_1 and ν_2) and the weak mixing angle (θ). Much like quarks, neutrinos propagate through space via the mass eigenstates, but interact via the flavor eigenstates.

If at production time, $t = 0$, we begin with a muon type neutrino,

$$
|\nu_\mu(0)\rangle = -\sin\theta|\nu_1(0)\rangle + \cos\theta|\nu_2(0)\rangle
\tag{1.10}
$$

we see that the flavor state is a superposition of two distinct mass states. This may be extended to a later time by applying the quantum mechanical time evolution operator. The flavor eigenstate now depends not only upon the mixing angle, but also upon the energies of the mass states, E_1 and E_2 respectively:

$$
|\nu_\mu(t)\rangle = -\sin\theta e^{-iE_1 t}|\nu_1\rangle + \cos\theta e^{-iE_2 t}|\nu_2\rangle.
\tag{1.11}
$$

Rewriting each of the mass states in terms of its flavor state components shows that at some later time, t, the neutrino has evolved to have some part ν_μ and some part ν_e:

$$
|\nu_\mu(t)\rangle = (\cos^2\theta e^{-iE_1 t} + \sin^2\theta e^{-iE_2 t})|\nu_\mu\rangle + \sin\theta\cos\theta(e^{-iE_2 t} - e^{-iE_1 t})|\nu_e\rangle
\tag{1.12}
$$

Thus, a pure flavor (weak) eigenstate born through a weak decay will oscillate into another flavor as the state propagates in space. The oscillation is due to the fact that each of the mass eigenstate components propagates with different frequencies if the masses are different, $\Delta m^2 = \left| m_2^2 - m_1^2 \right| > 0$. Then the probability for seeing an electron neutrino in a beam that was initially muon neutrinos is

$$
\begin{aligned}
\mathcal{P}_{osc} &= |\langle \nu_e | \nu_\mu(t) \rangle|^2 \\
&= \frac{1}{2}\sin^2 2\theta[1 - \cos(E_2 - E_1)t]
\end{aligned}
\tag{1.13}
$$

This can be put into a more recognizable form by using $E_1 = \sqrt{p^2 + m_1^2} \approx p + m_1^2/2p$ (and similar

for E_2) and $(t/p) = (tc)/(pc) = L/E$. This gives the standard form for 2-flavor oscillations:

$$P_{osc} \approx \frac{1}{2} \sin^2 2\theta \left(1 - \cos \left(\frac{(m_2^2 - m_1^2)L}{E} \right) \right)$$
$$= \sin^2 2\theta \sin^2 (1.27 \frac{\Delta m^2 (eV^2) L(m)}{E(MeV)}) \tag{1.14}$$

where the factor of 1.27 arises from replacing the $\hbar$'s and c's that were previously set to 1. Eq. 1.14 is

called the appearance probability, since flavor ν_e appears in a beam of neutrinos that was originally

ν_μ. This may also be written as a disappearance probability, the probability that ν_μ's disappear

from the beam:

$$\mathcal{P}_{osc} = |\langle \nu_\mu | \nu_\mu(t) \rangle|^2$$
$$= 1 - \sin^2 2\theta \sin^2 (1.27 \frac{\Delta m^2 (eV^2) L(m)}{E(MeV)}). \tag{1.15}$$

The use of only two neutrino types in the mixing is an oversimplification, however. The mixing

can be extended to include all three neutrino generations by taking the product of three unitary

matrices

$$U_{12} = \begin{pmatrix} \cos\theta_{12} & \sin\theta_{12} & 0 \\ -\sin\theta_{12} & \cos\theta_{12} & 0 \\ 0 & 0 & 1 \end{pmatrix},$$

$$U_{13} = \begin{pmatrix} \cos\theta_{13} & 0 & \sin\theta_{13} \\ 0 & 1 & 0 \\ -\sin\theta_{13} & 0 & \cos\theta_{13} \end{pmatrix}, \quad \text{and} \tag{1.16}$$

$$U_{23} = \begin{pmatrix} 1 & 0 & 0 \\ 0 & \cos\theta_{23} & \sin\theta_{23} \\ 0 & -\sin\theta_{23} & \cos\theta_{23} \end{pmatrix}.$$

That is,

$$U = \begin{pmatrix} c_{12}c_{13} & c_{13}s_{12} & s_{13} \\ -s_{12}c_{23} - c_{12}s_{23}s_{13} & c_{12}c_{23} - s_{12}s_{23}s_{13} & s_{23}c_{13} \\ s_{12}s_{23} - c_{12}c_{23}s_{13} & -c_{12}s_{23} - s_{12}c_{23}s_{13} & c_{13}c_{23} \end{pmatrix} \tag{1.17}$$

where $c_{ij} \equiv \cos\theta_{ij}$ and $s_{ij} \equiv \sin\theta_{ij}$. This will be expressed, for compactness and simplicity, as

$$
U = \begin{pmatrix} U_{e1} & U_{e2} & U_{e3} \\ U_{\mu 1} & U_{\mu 2} & U_{\mu 3} \\ U_{\tau 1} & U_{\tau 2} & U_{\tau 3} \end{pmatrix}.
\tag{1.18}
$$

Then, in the same manner as in the quark sector, mixing between the three neutrino generations may be related by this unitary mixing matrix

$$
\begin{pmatrix} \nu_e \\ \nu_\mu \\ \nu_\tau \end{pmatrix} = \begin{pmatrix} U_{e1} & U_{e2} & U_{e3} \\ U_{\mu 1} & U_{\mu 2} & U_{\mu 3} \\ U_{\tau 1} & U_{\tau 2} & U_{\tau 3} \end{pmatrix} \begin{pmatrix} \nu_1 \\ \nu_2 \\ \nu_3 \end{pmatrix}.
\tag{1.19}
$$

Given a 3×3 mixing matrix, the more complete form of the oscillation probability may be written as

$$
\mathcal{P}(\nu_\alpha \to \nu_\beta) = \delta_{\alpha\beta} - 4 \sum_{j>i} U_{\alpha i} U_{\beta i} U_{\alpha j}^* U_{\beta j}^* \sin^2\left(\frac{1.27 \Delta m_{ij}^2 L}{E} \right).
\tag{1.20}
$$

As in the case of 2-generation mixing, the mixing angle affects the amplitude of the oscillations, and the mass-squared difference affects the frequency of the oscillations. In turn, these fundamental parameters have an effect on how the oscillations are observed in experiments. The probability to see oscillations also depends upon two parameters which may be adjusted experimentally, L, the distance from the neutrino source to the detector, and E, the neutrino energy. For a small Δm^2, oscillations will occur slowly. In this case, if an experiment's ratio of $\frac{L}{E}$ is too small, *i.e.*, the experiment is constructed too close to the neutrino source, the probability of observing the oscillations will be very low. Similarly, it will be very difficult to detect oscillations if the mixing angle is small. Experiment designers choose their detector locations and sizes carefully in order to create experiments that probe the interesting regions of Δm^2 and $\sin^2 2\theta$.

1.4   Types of Oscillation Experiments

At the most basic level, all neutrino oscillation experiments are the same. There are only two components: a neutrino source, and a neutrino detector. Any difference between what the source produces and what the detector observes can be attributed to oscillations. This is unfortunately

not as straight-forward as it sounds due to the fact that neutrinos only interact through the weak force; most of the neutrinos produced will travel straight through the detector without interacting. It is necessary, therefore, to have very large detectors and intense sources in order to perform statistically significant experiments in reasonable amounts of time.

While all oscillation experiments consist of the same basic design, they may be placed into the gross categories of "appearance" and "disappearance" experiments. Those referred to as "appearance" experiments use a beam of neutrinos with a given flavor, ν_α, and observe neutrinos of a *different* flavor, ν_β, at some distance from the neutrino source. In this type of experiment, it is important to know if the initial neutrino beam contains some amount of ν_β (*i.e.*, it is is not purely ν_α). In this case, the fraction of ν_β must be small and well-known. Otherwise, it is impossible to tell if the detected ν_β's were part of the initial beam or if they arose from flavor oscillations.

In "disappearance" experiments, one starts with a beam of neutrinos of flavor ν_α and observes at some distance from the source *fewer* ν_α's than were initially in the beam. It is important to know the initial ν_α flux accurately in this type of experiment. If the initial flux is not well-known, it is impossible to know how many of the initial neutrinos of flavor ν_α have disappeared.

All neutrino experiments take advantage of charged current interactions (Fig. 1.1 right) in order to distinguish the type of neutrinos they observe. The flavor of the charged lepton that exits a charged current interaction tags the flavor of the neutrino that was involved, *e.g.*, an electron neutrino interaction will always produce an electron in the final state of a charged current interaction.

Oscillation experiments, both appearance and disappearance, have a difficult quest: detecting particles that rarely interact, and when they do, with interactions that only tag the incoming neutrino flavor *part* of the time. The seemingly impossible challenge comes with a big reward, though: experiments can begin to close in on the answer of the neutrino masses and mixing angles.

1.5 Neutrino Oscillation Landscape

There have been many experiments over the years that have contributed to the current understanding of the oscillation landscape. Flavor oscillations in neutrinos originating at the Sun are
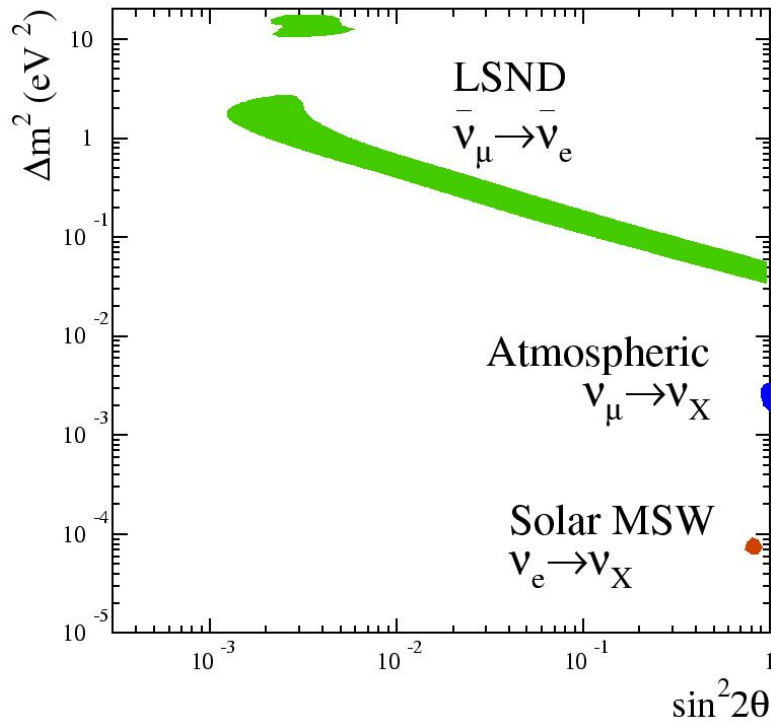
Figure 1.2: The current landscape of neutrino oscillation allowed regions, mapped as a function of Δm^2 and $\sin^2 2\theta$.

now well-established [12–17]. In addition, measurements from the Kamiokande, Super Kamiokande (Super-K), MACRO, K2K, and Soudan2 experiments also indicate the existence of oscillations in neutrinos from the atmosphere [18–22]. When these results are considered in conjunction with results from reactor experiments [23–25], and the accelerator-based LSND experiment [26], the landscape of oscillations is quite full. The current understanding of the allowed regions for neutrino flavor oscillations is shown as a map of the fundamental oscillation parameters $(\Delta m^2, \sin^2 2\theta)$ in Fig. 1.2.

It is clear from this representation that the combined results from all experiments indicate that there are three distinct values of Δm^2. If there are only three neutrino flavors, it is not possible to explain all three allowed regions by oscillations (unless CPT violation [27, 28] or some other exotic scheme is invoked) because it must be true that

$$\Delta m_{12}^2 + \Delta m_{23}^2 = \Delta m_{13}^2. \tag{1.21}$$

This is clearly not the case for the allowed regions shown in the figure:

$$10^{-5} + 10^{-3} \neq 1. \tag{1.22}$$

The only region of this oscillation landscape that has not been rigorously tested is the region of high Δm^2 ($\Delta m^2 \simeq 1$ eV^2), where the LSND signal (indicated by the long band of green on the figure) lies.

This signal comes from the accelerator-based Liquid Scintillator Neutrino Detector (LSND) Experiment which took place at Los Alamos National Laboratory. The experiment saw evidence for the appearance of $\bar{\nu}_e$'s in a $\bar{\nu}_\mu$ beam [26] using the Los Alamos LAMPF beam of 800 MeV protons. Protons interacted with a water target, and the resulting mesons decayed to muons and neutrinos. The neutrino signals were detected by photomultiplier tubes in a liquid-scintillator-filled tank [29] located at $L = 30$ meters from the neutrino source. The reported excess of $\bar{\nu}_e$'s was observed in a region of parameter space (Δm^2 *vs.* $\sin^2 2\theta$) in which neutrino oscillations have not been fully ruled out by other experiments; confirmation of this signal is crucial.

1.6 The MiniBooNE Oscillation Search

The Mini Booster Neutrino Experiment (MiniBooNE) at Fermilab was designed with the intention of resolving the issue of the unconfirmed LSND signal. The details of the experiment will be discussed in detail in Chapter 3, but a brief overview will be presented here along with the predicted oscillation sensitivity.

MiniBooNE, like LSND, is an accelerator-based oscillation experiment. The neutrino beam is created by directing 8 GeV protons from the Fermilab Booster onto a beryllium target. Proton interactions in the target material produce a secondary beam of mesons that subsequently decay to produce a neutrino beam with mean energy ~ 750 MeV. The detector is located 541 m from a neutrino source in the Booster neutrino beam line. This results in an experimental $\frac{L}{E}$ of ~ 0.72 m/MeV which is similar to that of LSND ($\frac{L}{E} \simeq 0.75$ m/MeV); the two experiments are sensitive to the same ranges in oscillation parameter space.

The oscillation analysis at MiniBooNE will be "blind," where the analysis is developed based on Monte Carlo simulations and a small sample of data. Once the analysis has been finalized, it

will be applied to the blinded data. This method was agreed upon by the collaboration for several reasons. Most importantly, a blind analysis is not susceptible to the unintentional biases that might be introduced if all of the data were immediately available. Secondly, since the LSND result is controversial, it is important gain the confidence of the physics community before releasing a result that will serve to end the controversy.

MiniBooNE's predicted sensitivity to ν_e appearance with 1×10^{21} protons on target is shown in Fig. 1.3. The dark (light) blue region on the plot shows the 90% (99%) confidence level allowed areas of parameter space corresponding to the LSND final result. The solid blue, red, and black lines are the 90% confidence level, 3σ, and 5σ sensitivity lines predicted for MiniBooNE; MiniBooNE will be sensitive to everything to the right of each solid line at the level indicated.
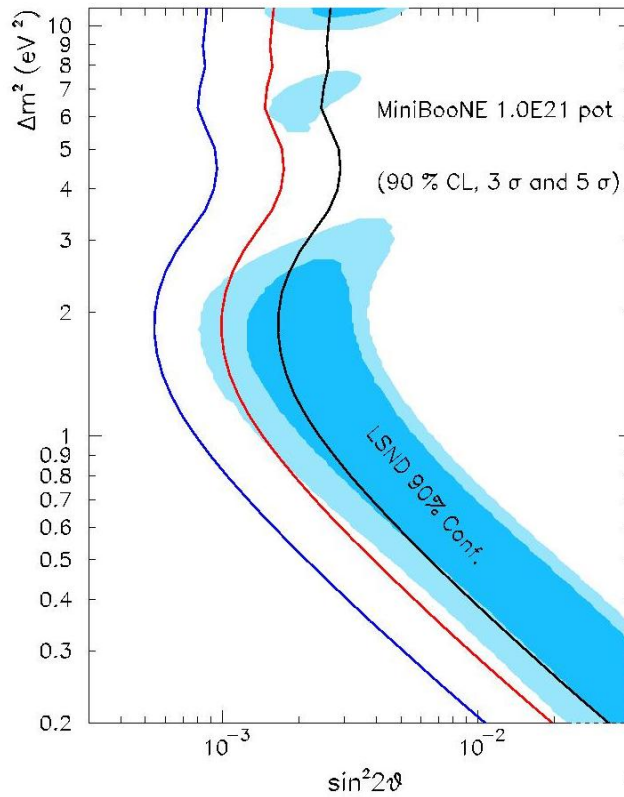
Figure 1.3: MiniBooNE's predicted sensitivity to oscillations for 1×10^{21} protons on target overlaid on the LSND allowed region as a function of Δm^2 and $\sin^2 2\theta$ [30].

1.7 Synopsis of this Thesis

The thesis is organized into 7 additional chapters. Chapter 2 presents the theory of neutrino production of neutral current π^0's by resonant and coherent processes. Chapter 3 describes the experimental setup, including the beam, the detector, and the electronics used for data acquisition. Also discussed in this chapter is the calibration of detector components, and their response to light produced in the detector. Chapter 4 gives an overview of the simulation programs used to model physics processes in MiniBooNE. Chapters 5 and 6 present the elements for the neutral current π^0 analysis: event selection and analysis procedures. A discussion of the systematic errors follows in Chapter 7. Finally, the results of the neutral current π^0 cross section measurement are presented in Chapter 8.

Chapter 2

Neutral Current Single π^0 Cross Sections

This chapter discusses the main theoretical models for neutral current production of single π^0's in neutrino interactions. We begin with a discussion of the dominant mechanism, which is resonant production, and follow with a discussion of coherent production. The cross section for these processes at energies relevant to MiniBooNE is not at all well-measured, as will be shown in the final section of this chapter.

2.1 Resonant π^0 Production Theory

Resonant production of π^0's is the dominant process for single π^0 production. It occurs when a baryon resonance is excited and subsequently decays back to its ground state nucleon, emitting one or more mesons, such as π^0's, in the process. One model for the cross section of this production mechanism is that of Rein and Sehgal [31].

The model uses the relativistic quark model proposed by Feynman, Kislinger, and Ravndal (FKR model) in 1971 [32]. In the FKR model, a nucleon is treated as the ground state of a three-quark system that is held together by harmonic forces [33]. Excitations of the three-dimensional modes of the oscillator system correspond to baryon resonances. The formulation provides matrix elements of the vector and axial vector currents that can be used to describe the transitions between
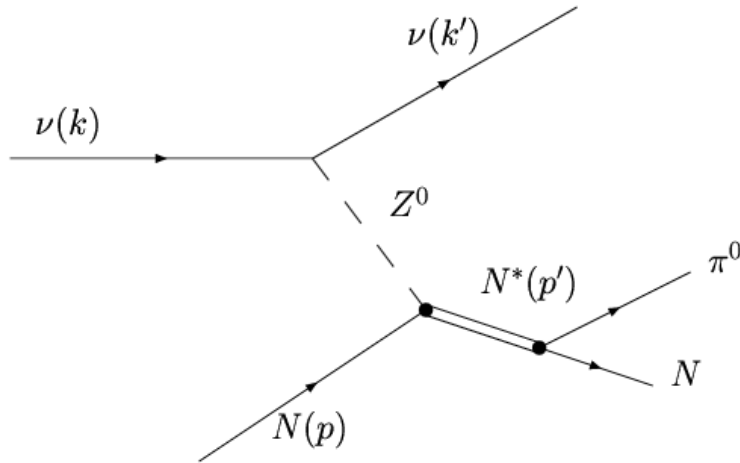
Figure 2.1: Feynman diagram for resonant production of neutral current single π^0's.

the ground state and resonant states. The model does not perfectly describe the baryon resonances though. Form factors must be introduced to mimic the fall-off with Q^2 (the negative of the four-momentum squared) of all quasi-elastic reactions.

The resonance production of single π^0's can be described in the usual fashion, as an interaction of two currents:

$$\mathcal{M}(\nu\mathcal{N} \to \nu\mathcal{N}\pi) = \frac{G_F \cos\theta_C}{\sqrt{2}} J_L^\mu J_\mu^N \tag{2.1}$$

where G_F is the Fermi constant, J_L^μ is the leptonic current, and J_μ^N is the hadronic current. The Feynman diagram[1] for this process is shown in Fig. 2.1. In the first step of the process, we consider only *production* of the resonant state ($\nu\mathcal{N} \to \nu\mathcal{N}^*$). Later, the *decay* of the resonance ($\nu\mathcal{N}^* \to \nu\mathcal{N}\pi$) will be addressed.

The leptonic current is given by

$$J_L^\mu = \bar{u}_\nu(k')\gamma^\mu(1-\gamma_5)u_\nu(k), \tag{2.2}$$

which may be decomposed into polarization states of the intermediate Z^0 vector boson: left-handed (e_L^μ), right-handed (e_R^μ), and scalar (e_S^μ). The decomposition depends on the frame of reference; the most useful frame to describe resonant production is the rest frame of the resonance. In this frame, the leptonic current may be written as

$$\bar{u}_\nu(k')\gamma^\mu(1-\gamma_5)u_\nu(k) = -2\sqrt{2}E\sqrt{\frac{-q^2}{Q^2}}\left[u \cdot e_L^\mu - v \cdot e_R^\mu + \sqrt{2uv} \cdot e_S^\mu\right] \tag{2.3}$$

---

[1]All Feynman diagrams in this document were created using `JaxoDraw v 1.2-0` [34], which is downloadable from `http://altair.ific.uv.es/~JaxoDraw/`.

where $u = (E_\nu + E'_\nu + Q)/2E_\nu$ and $v = (E_\nu + E'_\nu - Q)/2E_\nu$ are expressed in terms of initial (final) lepton energy, E_ν (E'_ν), and Q is the modulus of the 3-momentum transfer in the laboratory frame.

Since the exact makeup of the hadronic current, J^N_μ, is unknown, it is standard to write the reaction in terms of unitless form factors, such that

$$J^N_\mu = 2m_{N^*}F^N_\mu, \tag{2.4}$$

where m_{N^*} is the resonance mass.

The full matrix element for production of the resonant state

$$\mathcal{M}(\nu\mathcal{N} \rightarrow \nu\mathcal{N}^*) \quad = \quad \frac{G_F \cos\theta_C}{\sqrt{2}} \left[\bar{u}_\nu(k')\gamma^\mu(1-\gamma_5)u_\nu(k)\right]\langle\mathcal{N}^*|J^N_\mu|\mathcal{N}\rangle \tag{2.5}$$

may be written in terms of resonance rest frame quantities, using Eq. 2.3 and Eq. 2.4, as

$$-4G_F\cos\theta_C m_{N^*}E_\nu\left(\sqrt{\frac{-q^2}{Q^2}}\langle\mathcal{N}^*|ue^\mu_L F_\mu - ve^\mu_R F_\mu|\mathcal{N}\rangle + \frac{m_N}{m_{N^*}}\sqrt{2uv}\sqrt{\frac{-q^2}{Q^{*2}}}\langle\mathcal{N}^*|e^\mu_S F_\mu|\mathcal{N}\rangle\right) \tag{2.6}$$

where Q^* refers to the rest frame quantity ($Q^* = Qm_N/m_{N^*}$). This can then be rewritten in the form

$$-4G_F\cos\theta_C m_{N^*}E_\nu\left(\sqrt{\frac{-q^2}{Q^2}}\langle\mathcal{N}^*|uF_- - vF_+|\mathcal{N}\rangle + \frac{m_N}{m_{N^*}}\sqrt{2uv}\langle\mathcal{N}^*|F_0|\mathcal{N}\rangle\right) \tag{2.7}$$

where

$$\begin{aligned}
F_+ &= e^\mu_R F_\mu, \\
F_- &= e^\mu_L F_\mu, \text{ and} \\
F_0 &= \sqrt{-q^2/Q^{*2}}e^\mu_S F_\mu.
\end{aligned} \tag{2.8}$$

Then the production cross section of a single resonance is found by squaring the matrix element and averaging (summing) over initial (final) spins:

$$\frac{d\sigma}{dq^2 d\nu} = \frac{1}{32\pi m_N E^2_\nu} \cdot \frac{1}{2}\sum_{\text{spins}}|\mathcal{M}(\nu\mathcal{N} \rightarrow \nu\mathcal{N}^*)|^2 \frac{1}{2\pi} \cdot \frac{\Gamma}{(W-m_{N^*})^2 + \Gamma^2/4}. \tag{2.9}$$

The factor after the squared matrix element is a Breit-Wigner function accounting for the finite width of the resonance. Since the matrix element, $\mathcal{M}$, in Eq. 2.7 has three terms due to the

polarization of the intermediate vector boson, the resulting cross section also has three terms:

$$\sigma_L(q^2, W) = \frac{2\pi m_{N^*}}{m_{N^*}^2 - m_N^2} \frac{1}{2} \sum_{j_z} |\langle \mathcal{N}, j_z - 1 | F_- | \mathcal{N}^*, j_z \rangle|^2 \frac{1}{2\pi} \cdot \frac{\Gamma}{(W - m_{N^*})^2 + \Gamma^2/4}$$

$$\sigma_R(q^2, W) = \frac{2\pi m_{N^*}}{m_{N^*}^2 - m_N^2} \frac{1}{2} \sum_{j_z} |\langle \mathcal{N}, j_z + 1 | F_+ | \mathcal{N}^*, j_z \rangle|^2 \frac{1}{2\pi} \cdot \frac{\Gamma}{(W - m_{N^*})^2 + \Gamma^2/4}$$

$$\sigma_S(q^2, W) = \frac{2\pi m_{N^*}}{m_{N^*}^2 - m_N^2} \left(\frac{Q^2}{-q^2} \right) \frac{m_N^2}{m_{N^*}^2} \frac{1}{2} \sum_{j_z} |\langle \mathcal{N}, j_z | F_0 | \mathcal{N}^*, j_z \rangle|^2 \frac{1}{2\pi} \cdot \frac{\Gamma}{(W - m_{N^*})^2 + \Gamma^2/4}.$$

$$(2.10)$$

The matrix elements in the above equations are just the helicity amplitudes for the production of the resonance [31]. Once a resonance has been created, the second step is to determine its *decay* amplitudes. In the case of a single resonant state, only the width of the resonance and its branching ratio are important. In reality, the $\mathcal{N}\pi$ final state can be fed by several nearby resonances, which decay to the same final state simultaneously. One result of extending the model to account for this is that the various resonances may interfere, but this is only true for resonances which have the same spin and orbital angular momentum [31].

The decay amplitudes are easily determined by isospin analysis. As an example, the reaction $\nu p \to \nu p \pi^0$ is decomposed into its isovector and isoscalar partial amplitudes, shown below. The final state, $|p\pi^0\rangle$, has isospin $|I, I_3\rangle = |1/2, +1/2\rangle|1, 0\rangle$ which allows for contributions from both $|\Delta^+\rangle = |3/2, +1/2\rangle$ and $|N^*\rangle = |1/2, +1/2\rangle$ resonances. Then the coefficients for the partial amplitudes are found using Clebsch-Gordan rules:

$$\mathcal{A}(\nu p \to \nu p \pi^0) = \frac{2}{3} A_3^{NC} + \frac{1}{3} A_1^{NC} - \sqrt{\frac{1}{3}} S_1^{NC} \tag{2.11}$$

where A_3^{NC} (A_1^{NC}) are the reduced amplitudes for producing the isovector part of the isospin $\frac{3}{2}$ ($\frac{1}{2}$) final state, and S_1^{NC} is the reduced amplitude for the isoscalar part.

For neutral current channels, the $\Delta(1232)$ resonance is the dominant mechanism contributing to the interactions. This is shown at the generator-level[2] in Fig. 2.2 for the sum of resonant channels $\nu n \to \nu n \pi^0$ and $\nu p \to \nu p \pi^0$. The decay amplitudes of these resonances may be split into factors that have physical meaning. The first is a Breit-Wigner factor (see Eq. 2.31 of Ref. [31]), and the second is related to the branching ratio of the resonance into the $\mathcal{N}\pi$ final state. The final factor is the sign of the decay amplitude, important in the case of possible interference between resonances.

---

[2]MiniBooNE uses the `Nuance` neutrino cross section Monte Carlo, which will be discussed later in Chapter 4.
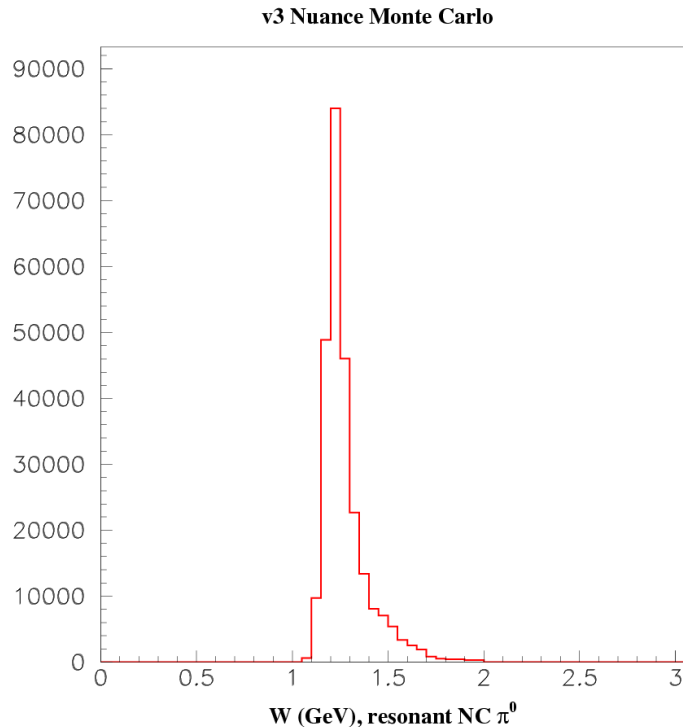
Figure 2.2: Generator-level plot of invariant mass for neutral current single π^0 production with the MiniBooNE and cross section Monte Carlo and event generator.

Unfortunately, the full amplitude described by the two factors attributed to the production and subsequent decay of a resonance are not sufficient for a general description of pion production by resonant excitation. A further complication arises if the study of $\mathcal{N}^*$-decay angular distributions is undertaken. The problem is that the calculated amplitude refers only to a single helicity component of all resonances that contribute to the same $\mathcal{N}\pi$ final state, but *all* helicity components should be taken into account.

Ref. [33] gives a detailed description of the framework needed to properly describe the amplitudes, taking multiple helicity states into account. The matrix element may be written

$$\mathcal{M}_{fi}(\nu\mathcal{N} \rightarrow \nu\mathcal{N}\pi^0) = \frac{G_F \cos\theta_C}{\sqrt{2}} \sum_{I=\frac{1}{2},\frac{3}{2}} a_I \mathcal{M}_{fi}^I. \tag{2.12}$$

where because there are four possible combinations of helicity states for the initial- and final-state nucleon, there are four amplitudes, $\mathcal{M}_{fi}$, for each isospin, I. In addition, the polarization of the intermediate vector boson must be taken into account, contributing three amplitudes for each of the four combinations of helicity states. In all, there are 12 helicity amplitudes that must be considered

for each vector and axial vector current interaction [33]. A partial wave expansion of the helicity amplitudes is carried out in order that each amplitude properly describe $\mathcal{N}\pi$ states with definite angular momentum and parity, *i.e.*, Δ and $\mathcal{N}^*$ resonances. The details of the expansion are so complicated that Rein and Sehgal "banished [them] to the Appendix" of Ref. [31].

2.1.1 Nonresonant Background

The main difference of the Rein and Sehgal cross section model as compared to the FKR quark model is the addition of some background amplitude, labelled "nonresonant" background. This was deemed necessary by comparison with data. The background contribution is added incoherently to the resonant cross section as a nucleon-like resonance amplitude ($|I, I_3\rangle = |1/2, 1/2\rangle$), except that the Breit-Wigner factor is replaced by a tunable scaling factor. It only affects the $I = 1/2$ parts of the cross section.

2.2 Coherent Production Theory

In coherent NC π^0 production, a neutrino interacts with an entire complex nucleus rather than the individual constituents of the nucleus ($\nu A \rightarrow \nu A \pi^0$). The process is referred to as "coherent" because all of the nucleons in the nucleus respond in phase, *i.e.*, the overall scattering amplitude is a sum of constructively interfering amplitudes from the individual nucleons. Thus, the nucleus recoils as a whole, without breaking up. There are several conditions for coherence, since the nucleus must remain unaltered:

1. The momentum transferred to any nucleon must be small enough that the nucleon remains bound in the nucleus, *i.e.*,

$$|\mathbf{k}|c(\text{MeV}) < \frac{\hbar c(\text{MeV} \cdot \text{fm})}{R(\text{fm})}$$

   where R is the nuclear radius.

2. There may not be any transfer of charge, spin, isospin, or any other quantum numbers. For example, if isospin were not conserved, the individual amplitudes for neutrons and protons would have opposite signs, destroying coherence.
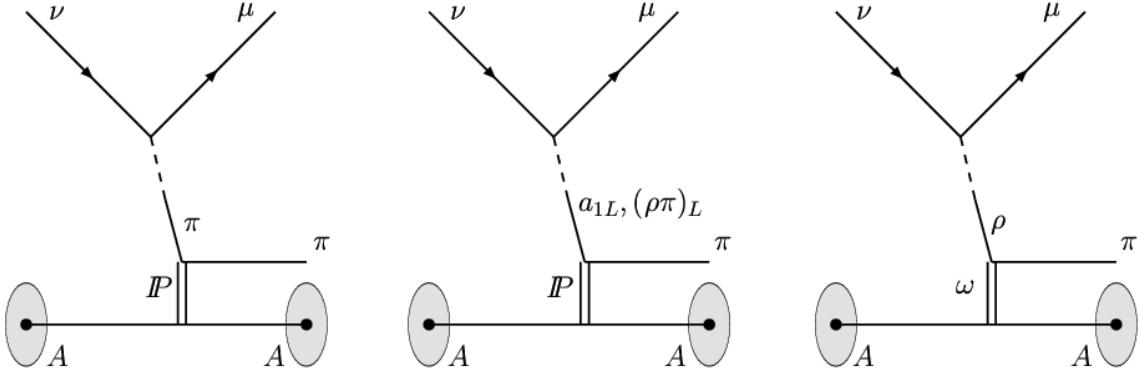
Figure 2.3: Several allowed Feynman diagrams for coherent π^0 production. (Reproduced from Ref. [35].)

3. For scattering angles $\theta > 0$, processes are suppressed by a factor $\sin^2 \theta \leq (1/R\nu)^2$, since $k_T \simeq \nu \sin \theta \leq 1/R$ [35].

For coherent processes, it is convenient (and sufficient for this discussion) to view the weak current as a superposition of virtual hadron states. The uncertainty principle allows these virtual states to fluctuate to *real* states for periods of time on the order of the "coherence" length:

$$l_c c = \Delta t_c \simeq \frac{2\nu}{Q^2 + m^2} \tag{2.13}$$

where m is the mass of the real hadron state [35]. If the coherence length is greater than the radius of the target nucleus (which is the same as saying that if the real hadron state exists for a time longer than the interaction time), the weak current will behave like a real hadron current.

There are a number of accepted theoretical models in use that attempt to create a framework to suitably describe the process; however, the predictions of these models vary widely [36–40]. There is even disagreement as to which Feynman diagrams contribute the most to this process; three allowed diagrams are shown in Fig. 2.3.

Although the existing models do not agree in many aspects, they each adhere to the requirements for coherence that were listed previously. Each model is built on the basis of Adler's theorem [41], relating the neutrino scattering cross section $\sigma(\nu_\mu \mathcal{N} \to \mu X)$ to the pion scattering cross section $\sigma(\pi \mathcal{N} \to X)$ at $Q^2 = 0$. Since the vector current is conserved (CVC hypothesis [42]), the vector contribution to the cross section vanishes at $Q^2 = 0$. The axial current is only partially conserved (PCAC hypothesis [43–45]), thus the cross section at $Q^2 = 0$ is entirely due to the axial current.

It is necessary to extrapolate to non-zero Q^2 to study the process, however, due to the limitations of experiments.

The extrapolation to obtain a more general cross section for a larger range of Q^2 typically uses the method of hadron dominance[3]. This method treats interaction currents as a superposition of hadrons. The Vector Meson Dominance (VMD) model [46], used in electromagnetic interactions, is a more specific form of hadron dominance. In the VMD model, the electromagnetic current is treated as a superposition of the lightest vector mesons. The transition amplitude for $\gamma + \alpha \rightarrow \beta$ can then be related to the sum of transition amplitudes for vector mesons:

$$\mathcal{A}(\gamma + \alpha \rightarrow \beta) = \sum_{V=\rho^0,\omega,\phi} \frac{e}{g_V} \frac{m_V^2}{Q^2 + m_V^2} \mathcal{A}(V + \alpha \rightarrow \beta) \tag{2.14}$$

An extension of the model to weak interactions treats the individual components of the weak current as a superposition of the lightest mesons: the ρ meson is used for the vector current component, and the π and a_1 mesons (and non-resonant $\rho\pi$ states) are used for the axial current. The a_1 is considered dominant (or more likely, the $\rho\pi$ states, which are virtually indistinguishable from the a_1 since the mass of the $\rho\pi$ system is very near the a_1 mass) [35, 38, 47]. For small but non-zero Q^2 ($Q^2 \leq 1\text{GeV}^2$), the vector current contribution is suppressed by a factor proportional to Q^2/m_ρ^2; at larger Q^2 it is suppressed by a factor proportional to $\sin^2\theta$, as mentioned previously. Interference of the vector and axial vector components is at worst small (an upper limit was established by Piketty and Stodolsky [48]), and only relevant in cases where the same final state can be produced by a ρ and an a_1. In the case of single pion production, there is no vector-axial vector interference. Additionally, Kopeliovich and Marage point out that vacuum fluctuations to a π must contribute very little (or nothing, if the lepton mass is neglected) to the axial vector current since a pion pole contribution would be extremely small (or vanish) when contracted with the lepton tensor. Following the calculations of the VMD model, a cross section can then be obtained in terms of the (assumed dominant) a_1 meson scattering component and extrapolated to higher Q^2 with an a_1 propagator. Taking into account additional contributions to the cross section from other mesons requires a more general propagator. This is achieved by the introduction of a parameter termed

---

[3]An alternative approach is based on using dispersion relations to compute amplitudes in the complex Q^2 plane. Although formally valid, the approach is of little use for $Q^2 \geq 1\text{GeV}^2$ because it requires much (non-existent) experimental information on the amplitudes of many hadronic systems [35].

the axial mass, m_A. It is expected to have a value near that of the a_1 meson. The cross section for non-zero Q^2 is then written as

$$\frac{d^2\sigma(\nu\mathcal{A} \to \nu\pi\mathcal{A})}{dxdy} = \frac{G^2}{2\pi^2} f_\pi^2 m_N E_\nu (1-y) \left(\frac{m_A^2}{Q^2 + m_A^2}\right)^2 \sigma(\pi\mathcal{A} \to \pi\mathcal{A}). \tag{2.15}$$

where x and y are Bjorken dimensionless variables:

$$x = \frac{Q^2}{2m_N\nu}$$

$$y = \frac{\nu}{E_\nu}.$$

The various theoretical formulations agree up to this point[4]. This means that the difference in the approaches must be found in how the pion-nucleus scattering cross section is approximated. The Rein and Sehgal formulation [36] will be described here, followed by a brief picture of the Belkov and Kopeliovich model [38].

2.2.1   Rein and Sehgal Formulation

The optical theorem relates the forward scattering part of the elastic scattering amplitude to the total cross section for the same particles:

$$\mathrm{Im}f(\theta = 0) = \left(\frac{k}{4\pi}\right)\sigma_{\mathrm{tot}}^{\pi\mathcal{N}} \tag{2.16}$$

where $f(\theta)$ is the elastic scattering amplitude and k is the center of mass momentum. The differential cross section may be written in terms of the scattering amplitude as

$$\frac{d\sigma}{d\Omega} = |f(\theta)|^2$$
$$= [\mathrm{Im}f(\theta)]^2 + [\mathrm{Re}f(\theta)]^2. \tag{2.17}$$

At $\theta = 0$, it is then evaluated in terms of the forward scattering part (using Eq. 2.16):

$$\left.\frac{d\sigma}{d\Omega}\right|_{\theta=0} = |f(0)|^2$$
$$= \left(\frac{k\sigma_{\mathrm{tot}}^{\pi\mathcal{N}}}{4\pi}\right)^2 + [\mathrm{Re}f(0)]^2 \tag{2.18}$$
$$= \left(\frac{k\sigma_{\mathrm{tot}}^{\pi\mathcal{N}}}{4\pi}\right)^2 \left(1 + \frac{\mathrm{Re}f(0)}{\mathrm{Im}f(0)}\right)$$

---

[4] Belkov and Kopeliovich differ in their opinion on what form should be used for the propagator to extrapolate to higher Q^2, but they continue by showing that the form used by Rein and Sehgal is adequate since the Q^2 dependences are close for the two forms.

The ratio of the real and imaginary parts of the forward scattering amplitude is defined as $r \equiv \text{Re} f(0)/\text{Im} f(0)$. The differential cross section can also be rewritten in terms of Lorentz-invariant t, the negative square of the four-momentum transferred by the scattered pion:

$$\left.\frac{d\sigma}{dt}\right|_{t=0} = \frac{(\sigma_{\text{tot}}^{\pi\mathcal{N}})^2}{16\pi}(1 + r^2) \tag{2.19}$$

In their paper, Rein and Sehgal use a pion-nucleon cross section $(\sigma_{\text{tot}}^{\pi\mathcal{N}})$ that is an average from measurements of pion-deuteron scattering; they approximate this average cross section by a sequence of linear functions [36].

To carry this into the framework of coherent pion production, a scattering cross section for pions on *nuclei* is needed instead of the cross section for pions on *nucleons*. This is achieved by the addition of a nuclear form factor, $F_{\mathcal{A}}(t)$, to the expression for the cross section:

$$\frac{d\sigma(\pi\mathcal{A} \to \pi\mathcal{A})}{dt} = A^2 |F_{\mathcal{A}}(t)|^2 \left.\frac{d\sigma(\pi\mathcal{N} \to \pi\mathcal{N})}{dt}\right|_{t=0} \tag{2.20}$$

where A is the atomic mass number of the nucleus. Rein and Sehgal choose the nuclear form factor to be represented by

$$|F_{\mathcal{A}}(t)|^2 = e^{-b|t|}F_{\text{abs}}. \tag{2.21}$$

The slope parameter, b, is found empirically by

$$b = \frac{1}{3}R^2, \quad (R = R_0 A^{\frac{1}{3}}), \tag{2.22}$$

where Rein and Sehgal use $R_0 = 1.0$ fm from measurements of R for aluminum. The F_{abs} factor is included to describe the effects of pion absorption in the nucleus. The nucleus is treated as a homogeneous sphere with uniform density in the calculation, so that the factor takes the form

$$F_{\text{abs}} = e^{-<x>/\lambda} \tag{2.23}$$

with $<x> = 3/4\,R$ and $\lambda^{-1} = \rho\,\sigma_{\text{inel}} = A(4/3\pi R^3)^{-1}\sigma_{\text{inel}}$. This leads to the simple form

$$F_{\text{abs}} = e^{-\frac{9A^{1/3}}{16\pi R_0^2}\sigma_{\text{inel}}}. \tag{2.24}$$

Data tables for the inelastic $\pi\mathcal{N}$ cross section were approximated by linear segments, as was done earlier for the average total pion-nucleon cross section. The form of the coherent pion production cross section in the Rein and Sehgal formulation is

$$\frac{d^3\sigma(\nu\mathcal{A} \to \nu\pi\mathcal{A})}{dxdydt} = \frac{G^2}{2\pi^2}f_\pi^2 m_N E_\nu(1-y)\left(\frac{m_A^2}{Q^2 + m_A^2}\right)^2 A^2 \frac{(\sigma_{\text{tot}}^{\pi\mathcal{N}})^2}{16\pi}(1 + r^2)e^{-b|t|}F_{\text{abs}}. \tag{2.25}$$

One problem with this formulation, as pointed out by Belkov and Kopeliovich [38], is that the crude description of the absorption contradicts the nature of coherent production. As absorption increases, the total pion-nucleus cross section should *increase*, and in the limit of scattering from a black disk (*i.e.*, total absorption), the cross section should reach a maximum of $2\pi R^2$. The exponential function in Eq. 2.24 clearly does not exhibit this behavior.

2.2.2 Belkov and Kopeliovich Formulation

The Belkov and Kopeliovich model of coherent pion production follows what is termed the Glauber-Gribov formalism[5] (see Appendix A of Ref. [35], and references within for a detailed derivation). This assumes that the scattering amplitude for hadron-nucleus interactions is one minus the product of amplitudes for the hadron *not* to interact with any of the target nucleons [35]. Another difference of their model, in comparison to the Rein and Sehgal model, is that the momentum transfer is divided into its longitudinal and transverse components. As with the Rein and Sehgal formulation, the optical theorem is used to write the hadron-nucleus scattering cross section in terms of the forward component:

$$\frac{d\sigma(h\mathcal{A})}{dt} = \left.\frac{d\sigma(h\mathcal{A})}{dt}\right|_{t=0} e^{B_L t_{min}} e^{B_T(t - t_{min})} \tag{2.26}$$

where t is related to the longitudinal and transverse components of the momentum transfer by $-p_L^2 \approx t_{min}$ and $-p_T^2 \approx t - t_{min}$. The minimum possible momentum transfer occurs when the angle between the incoming and outgoing particle is zero (*i.e.*, when the transverse component vanishes). In comparison with Eq. 2.25, the Belkov and Kopeliovich form is similar:

$$\frac{d^3\sigma(\nu\mathcal{A} \to \nu\pi\mathcal{A})}{dxdydt} = \frac{G^2}{2\pi^2} f_\pi^2 m_N E_\nu (1 - y) \left(\frac{m_A^2}{Q^2 + m_A^2}\right)^2 \frac{(\sigma_{tot}^{\pi\mathcal{A}})^2}{16\pi} e^{-B_T|t'|} e^{-B_L|t_{min}|} \tag{2.27}$$

where t has been rewritten as the variable $t' = t - t_{min}$. The values of B_T and B_L are calculated using the Glauber method, with a Woods-Saxon model of nuclear charge density [50] (as opposed to the simple uniform density homogeneous sphere used by Rein and Sehgal). The result of using a more sophisticated nuclear form factor (hidden in B_L and B_T in the expression above) to extend

---

[5]In an earlier paper, Lackner [49] also used Glauber's theory to describe coherent pion production by neutrino interactions. He did not, however, have corrections for inelastic scattering (Gribov's extension to the Glauber formalism). The Rein and Sehgal formalism is based on Lackner's work, but uses a simplified treatment of the effects of nuclear size and absorption.

from nucleon to nucleus cross sections is that the cross section of Eq. 2.27 exhibits the proper behavior as absorption increases.

2.2.3 Other Models

It is only right to mention also the work of Paschos and Kartavtsev [37], who agree with the ideas described above, but acknowledge the difficulty of computing the coherent cross section accurately. They perform a calculation that takes into account the amplitudes for the various allowed Feynman diagrams, but rely on available data in order to estimate the coherent cross section at lower and higher energies.

Finally, the model of Kelkar *et al.* [39] addresses coherent pion production mediated by Δ excitation in the nucleus. It uses a far more detailed model of the nuclear physics that accounts for nuclear medium effects on the Δ. As a result, the prediction for the coherent cross section at 1 GeV neutrino energy is dramatically suppressed in comparison to the predictions of other models.

The coherent cross section predictions of several of the models discussed here (and a few others) are shown as a function of neutrino energy in Fig. 2.4. Included are `Nuance` (the cross section Monte Carlo program used by MiniBooNE)[6], NEUGEN [51], the Marteau model [40], the Paschos-Kartavtsev model [37], and the model of Kelkar *et al.* [39]. The two data points are from experiments that measured the cross section for coherent π^0 production at 2 GeV and 3.5 GeV respectively. As seen in the figure, the predictions of the various cross section models vary widely.

As an ending note, we mention one interesting feature of coherent π^0 production that was not discussed earlier: the consequence of the lack of interference between the vector and axial vector parts of the cross section. This means that coherent production essentially conserves parity, and as a result, the cross section for neutrino coherent π^0 production should be the same as that for anti-neutrino coherent π^0 production. Appendix C discusses constraints that can be placed on theoretical models by measurements made with both neutrinos and anti-neutrinos.

---

[6]The prediction shown here does not include the effects of pion absorption, which lower the cross section; absorption effects are included at a later stage in the event generation code.
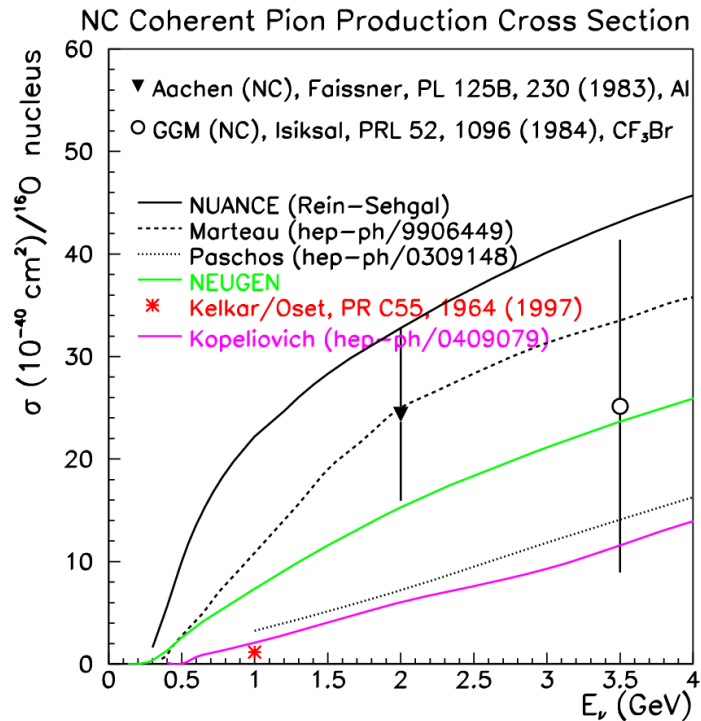
Figure 2.4: Low energy coherent neutral current single π^0 production as a function of neutrino energy. A recent correction to the `Nuance` generator (version 3.004) results in a predicted coherent π^0 production cross section essentially identical to that shown for NEUGEN.

2.3 Existing Measurements

While there is an abundance of data for charged current single pion production (both resonant and coherent), there are very few measurements of neutral current single pion production. Most of those that do exist are reported as ratios of neutral current to charged current cross sections. The results of existing ratio measurements for resonant single π^0 production are shown in Table 2.1.

The only existing measurement of the neutral current resonant single π^0 cross section that is not a ratio to the charged current cross section comes from 1970's bubble chamber data from Gargamelle [56]. A re-analysis performed by Eric Hawker (in collaboration with members of the original experiment) is shown in with cross section predictions from two neutrino cross section Monte Carlos in Fig. 2.5. The predictions agree with the datum at its energy, but there is currently no confirmation of agreement at other energies.

An additional measurement comes from K2K, who report the ratio of single π^0 events to their

Experiment	Target	Measurement	Ref.	Channel
ANL	H_2, D_2	0.51 ± 0.25	[52]	
ANL	H_2, D_2	0.09 ± 0.05	[53]	$\dfrac{\sigma(\nu_\mu p \to \nu_\mu p \pi^0)}{\sigma(\nu_\mu p \to \mu^- p \pi^+)}$
GGM	propane/freon	0.22 ± 0.04	[54]	
ANL	H_2, D_2	0.17 ± 0.08	[52]	
ANL	H_2, D_2	0.12 ± 0.04	[53]	$\dfrac{\sigma(\nu_\mu p \to \nu_\mu n \pi^+)}{\sigma(\nu_\mu p \to \mu^- p \pi^+)}$
GGM	propane/freon	0.13 ± 0.03	[54]	
ANL	H_2, D_2	0.11 ± 0.02	[53]	$\dfrac{\sigma(\nu_\mu n \to \nu_\mu p \pi^-)}{\sigma(\nu_\mu p \to \mu^- p \pi^+)}$
GGM	propane/freon	0.18 ± 0.05	[54]	
ANL	H_2, D_2	0.38 ± 0.11	[55]	$\dfrac{\sigma(\nu_\mu n \to \nu_\mu p \pi^-)}{\sigma(\nu_\mu n \to \mu^- n \pi^+)}$
GGM	propane/freon	0.45 ± 0.11	[56]	
A-P	Al	0.40 ± 0.06	[55]	$\dfrac{\sigma(\nu_\mu p \to \nu_\mu p \pi^0) + \sigma(\nu_\mu n \to \nu_\mu n \pi^0)}{2\sigma(\nu_\mu n \to \mu^- p \pi^0)}$
CIR	Al	0.17 ± 0.04	[57]	
CIR	Al	0.248 ± 0.085	[58]	

Table 2.1: Existing experimental measurements of NC/CC single pion production ratios.

inclusive ν_μ charged current sample [59]

$$\frac{\sigma(1\pi^0)}{\sigma(\nu_\mu \text{CC})} = 0.064 \pm 0.001_{\text{stat}} \pm 0.007_{\text{syst}}.$$

For coherent π^0 production, the first observation was reported in 1983 by the Aachen-Padova Collaboration [60]. It revealed itself as an excess at small angles in the distribution of the angle between the incoming neutrino and the π^0. Other signals were seen in the Gargamelle bubble chamber at CERN [56, 61], the SKAT experiment at Serpukhov [62], the 15' bubble chamber at FNAL [63, 64], and the CHARM experiment [65]. The only two measurements near MiniBooNE energies were that of Aachen-Padova and Gargamelle, shown in Table 2.2.
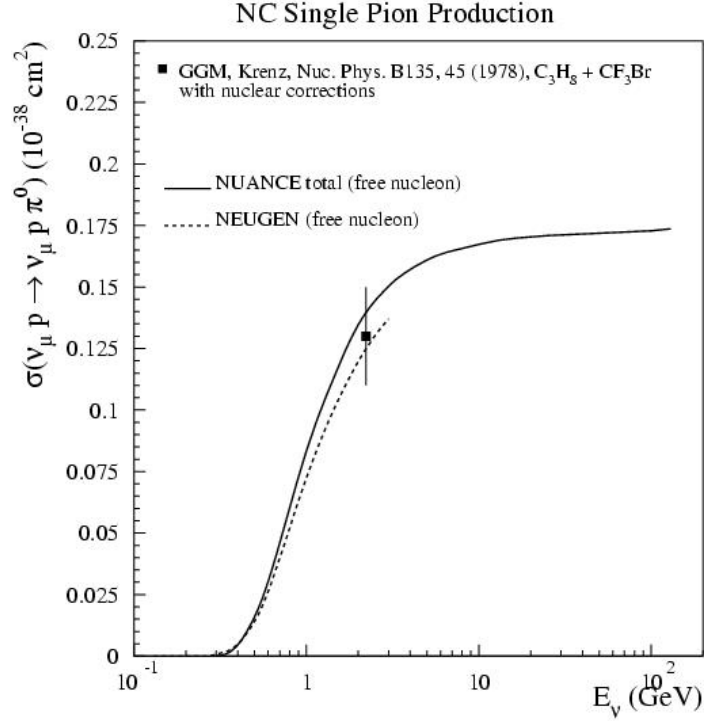
Figure 2.5: Neutral current single π^0 production cross section on protons as a function of neutrino energy.

Experiment	Target	$< E_{\overset{(-)}{\nu}} >$ (GeV)	Cross section (10^{-40}) cm^2/nucleus	Reference
Aachen-Padova	Al	2	$\sigma_\nu = 29 \pm 10$ $\sigma_{\bar\nu} = 25 \pm 7$	[60]
Gargamelle	freon	2	$\sigma_\nu = 31 \pm 20$ $\sigma_{\bar\nu} = 45 \pm 24$	[61]

Table 2.2: Coherent single pion cross section measurements near MiniBooNE energies.

Chapter 3

MiniBooNE

MiniBooNE is the initial stage of the Booster Neutrino Experiment at Fermi National Accelerator Laboratory in Batavia, Illinois. As discussed briefly in Section 1.6, the main goal of this experiment is to study the region of oscillation parameter space, Δm^2 *vs.* $\sin^2 2\theta$, which contains the LSND result. That result has been interpreted as $\bar{\nu}_\mu \to \bar{\nu}_e$ oscillations, but has yet to be confirmed. On the way to answering the remaining question of the LSND signal, MiniBooNE will collect more than 1 million neutrino interactions on pure mineral oil (CH_2), enabling the experiment to also address interesting non-oscillation physics such as the cross section measurement discussed in this work.

This chapter will give an overview of the experiment, including discussions of the beamline and target, detector hardware, calibrations, and detector response.

3.1   General Overview of Experiment

A schematic representation of the experiment is shown in Fig. 3.1. The MiniBooNE neutrino beam is produced by 8 GeV kinetic energy protons from Fermilab's proton synchrotron, known as the Booster. The protons are incident on a beryllium target, and produce a secondary beam of mesons through interactions in the target. The target is located inside a device called a horn, which creates a toroidal magnetic field to focus the charged mesons created in the proton-beryllium interactions. The mesons are sign-selected (by positive or negative charge) in the horn and directed to a 50 meter
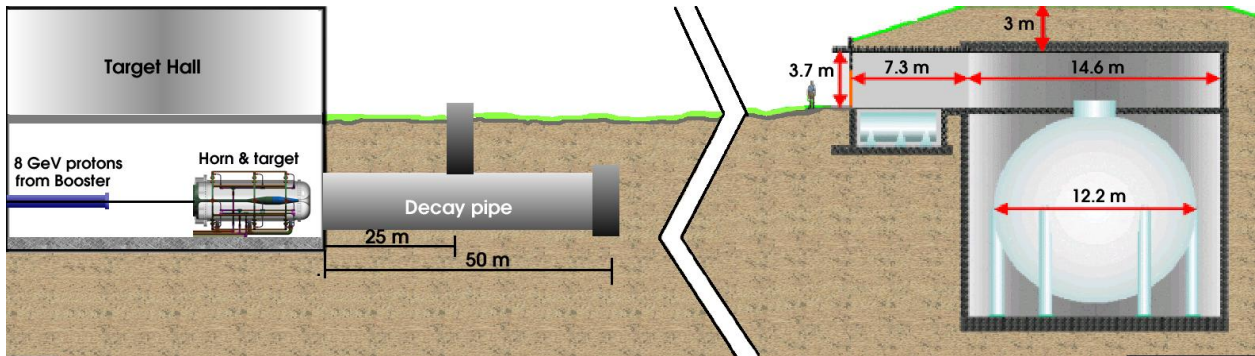
Figure 3.1: A schematic representation of the MiniBooNE beamline and detector, not to scale.

decay region. As the name implies, this is where most of the mesons decay to create the tertiary beam of neutrinos. Any mesons that do not decay in this region are stopped by an absorber located at the downstream end of the decay region. The tertiary beam, consisting of mostly muons and neutrinos, must travel through approximately 500 meters of earth to reach the detector. Since the earth stops all charged particles, the beam is purely neutrinos by the time it reaches the detector. The detector consists of a 610 cm radius spherical tank made of carbon steel. It resides in a cylindrical concrete structure that is below ground; the top of the detector is at grade level. The rate of cosmic rays entering the detector is reduced by approximately 3 meters of earth overburden that cover the detector.

The detector itself is instrumented with photomultiplier tubes and filled with undoped mineral oil. It is separated into two optically isolated concentric regions: the inner "tank" region and the outer veto region. There are 1280 photomultiplier tubes (PMTs) in the tank region (10% coverage) and 240 in the veto region.

The neutrinos may interact with nucleons in the detector medium. When they do, both Čerenkov radiation and scintillation light are produced as the charged particles from the interactions travel through the mineral oil. The light is detected by the photomultiplier tubes, and the pattern of light in the tank region is used to tag the type of interaction that produced it. Light creation and propagation will be discussed further in Section 3.6. The veto region detects charged particles entering or exiting the tank region; it is primarily used to reject cosmic muons. Additionally, it provides a means by which to identify uncontained events and events that arise from interactions in the dirt surrounding the detector building.

3.2 Beam

3.2.1 Primary Beam

MiniBooNE is part of the Fermilab 8 GeV Fixed Target Facility. Fig. 3.2 shows how the Booster primary beam is extracted into the 8 GeV beamline. The beam skirts the edge of the Main Injector, travelling through a beam pipe near the MI-10 service building to reach the 8 GeV beamline.
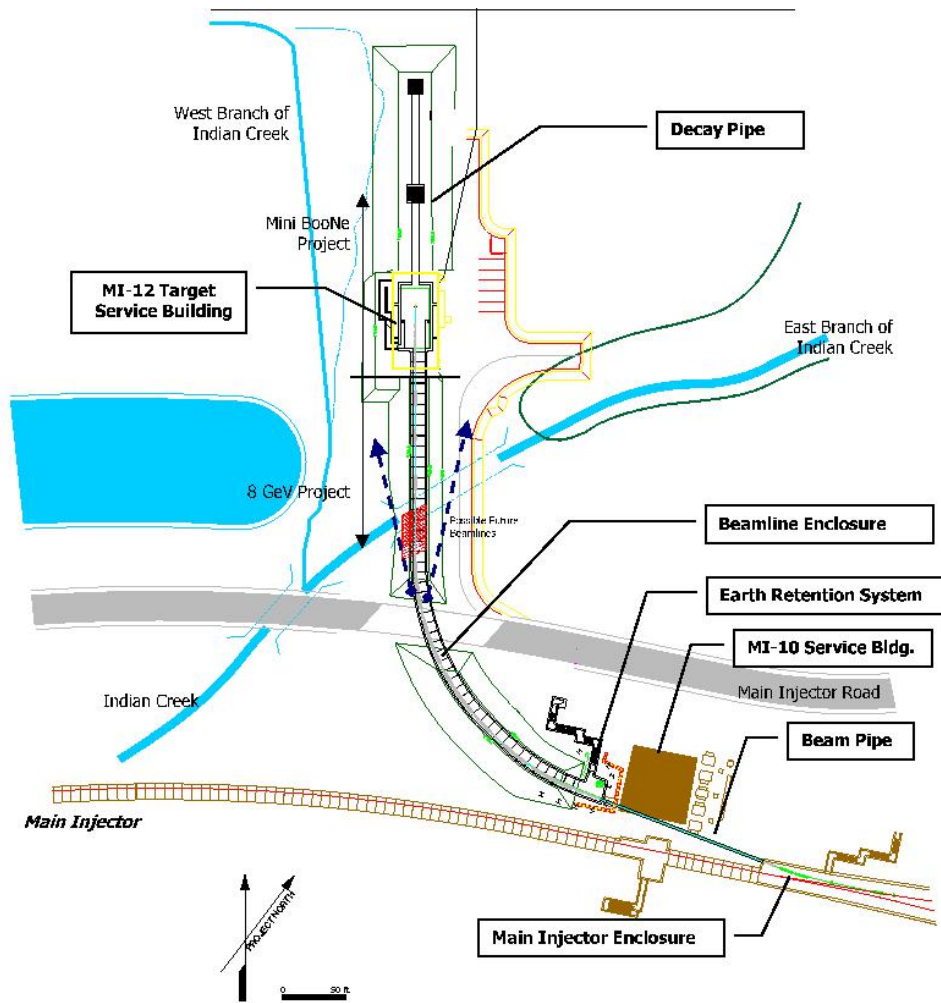
Figure 3.2: Booster fixed target facility with schematic of 8 GeV beamline [66].

The proton beam that is extracted from the Booster has 8 GeV kinetic energy (8.9 GeV/c momentum). At design intensity, protons arrive from the Booster in a 1.6 μs pulse at a rate of up to 5 Hz with $\sim 5 \times 10^{12}$ protons per pulse. The 8 GeV beamline transports the proton beam from MI-10 to the MiniBooNE target. Beam position, profile, and intensity are monitored with BPMs (beam position monitors), multiwires, and toroids respectively.

A program called Autotune [67] is used to keep the beam on target, with the proper angle and position. A donut collimator and a loss monitor are installed upstream of the target, however, as a safeguard against mistuned beam. These devices trip off the beam if it moves too far from its nominal position, preventing large amounts of energy from being deposited in the horn [66].

3.2.2   Horn and Target

The Booster protons strike a 71 cm beryllium target; proton interactions in the target produce short-lived hadrons (as well as protons and neutrons). The target is located inside a magnetic focusing device called a horn, which transports current to generate a focusing magnetic field in the volume between two coaxial conductors.

The MiniBooNE horn is a masterpiece of engineering, designed by Bartoszek Engineering [68] to satisfy a number of requirements and constraints. The primary requirement was to create a magnetic field with the correct focusing characteristics to produce the desired secondary beam of mesons. It was designed to withstand stresses due to target heating and cooling, radiation damage, as well as a high repetition rate.

A schematic drawing of the horn is shown in Fig. 3.3. Its total length is 73 inches (185.4 cm). The radius of the inner conductor varies from 0.87 inches (2.2 cm) to 2.58 inches (6.54 cm); the inner radius of the outer conductor is 11.81 inches (30.0 cm). Current flows along the inner conductor and back along the outer conductor (although the polarity can be reversed if desired) to produce a toroidal magnetic field that is contained in the volume between the two coaxial conductors. The shape of the inner conductor and the magnitude of the current were optimized with GEANT [69] to maximize the ν_μ flux between 0.5 and 1 GeV at the detector while minimizing flux above 1 GeV.

Current is supplied to the horn through air-cooled striplines that attach to its upstream end. The horn operates at an average pulse rate of 5 Hz. It carries 170 kA of current in a 143 μs long pulse that repeats 10 times in a row with 1/15 second between each pulse. The horn then turns off until approximately 2 seconds before the first pulse in the next train is due to arrive from the Booster. It is cooled with water (from our radioactive water (RAW) system) that is sprayed onto the inner conductor through vibration-isolated nozzles attached to the outer conductor. Stainless steel bellows form the junction between the nozzles and the outer conductor, providing a water-

Figure 3.3: Solid model rendering of MiniBooNE horn [68]. The outer conductor is rendered transparent to show the coaxial inner conductor. Striplines are connected to the upstream end (left side of drawing) and current travels along the inner conductor and back along the outer conductor.
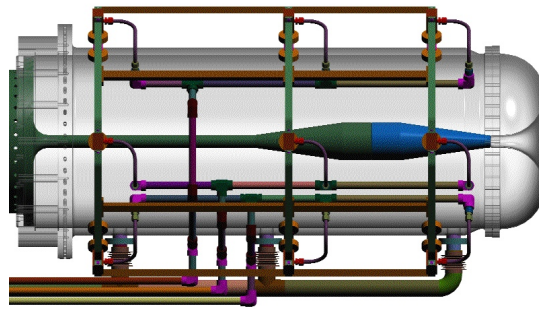
Figure 3.4: Solid model rendering of MiniBooNE horn with support structure for water system [68]. Outer conductor rendered transparent to show spacing of cooling nozzles along inner conductor.

tight connection that is relatively uncoupled from vibrations of the outer conductor. The entire RAW system is supported by a rigid truss that surrounds but does not touch the horn, shown in Fig. 3.4.

The horn survived 96 million pulses, nearly reaching its design lifetime of 100 million pulses. In August, 2004, it developed a ground fault that made it unsafe to operate. It was replaced with a spare horn during the 2004 Fall shutdown, and the spare has been operating smoothly.

Inside the horn, the beryllium target intercepts the primary 8 GeV proton beam, providing material for the primary interactions that yield mesons which decay to neutrinos. Although the target is located inside the horn, it is physically separate from the horn assembly to allow extraction of the target without removing the horn in the event of target failure. Beryllium was chosen as

the target material to minimize the beam power load on the target cooling system, minimize the remnant radioactivity due to proton exposure, have a high pion production yield, and be resistant to material fatigue due to the large number of beam cycles it must endure [70]. Some of the relevant properties of beryllium are listed in Table 3.1.

Density	1.85 g/cm^3
Interaction length	40.7 cm
Specific energy loss (MIP)	1.59 MeV/cm
Specific heat	3.3 J/(cm^3 K)
Young's modulus	3.1×10^{11} GPa

Table 3.1: Properties of beryllium.
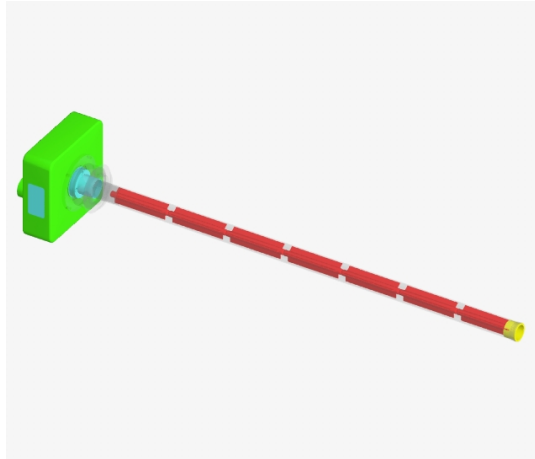
Figure 3.5: Solid model rendering of MiniBooNE target assembly [68]. The outer beryllium tube is rendered transparent to show the seven slugs. The aluminum manifold (green block on left side of drawing) has passages that allow air to flow through the target assembly.

The target consists of seven cylindrical beryllium slugs, two concentric beryllium tubes, an aluminum manifold piece, and a stainless steel bellows that makes electrical contact with the horn inner conductor. Fig. 3.5 shows a model of the target. Each slug is four inches long and 1 cm in diameter. Three radial cooling fins (not shown in figure) are placed symmetrically around the axis. The target is made up of these slugs, rather than one solid piece, in order to minimize forces due to off-axis, asymmetric heat loads from the proton beam. The outer beryllium tube serves as both a support for the inner tube and as an air duct for target cooling. The upstream ends of

both the inner and outer tubes are connected to the aluminum manifold block, which is attached to the stainless steel bellows to make electrical contact with the horn and prevent arcing between the horn and target assemblies.

3.2.3   Decay Region

The focused beam exiting the horn consists mainly of unscattered and scattered primary protons and positively charged mesons. These particles travel into a 50 m long decay pipe of 36 inch radius that is closed at both ends and filled with air. The proton beam 50 m from the target is $100 - 150$ mm wide, and the secondary meson beam is even more divergent.

At the downstream end of the decay pipe, a permanent beam absorber (the "50 m absorber") stops all hadrons and low-energy muons. There is also an intermediate absorber located 25 m from the target which can be lowered into the beam to provide systematic checks of signal versus background for the oscillation search.

When the horn is operated in "neutrino mode," the secondary beam is dominated by π^+'s with energies around 2 GeV. (As mentioned earlier, the polarity of the horn may be reversed to run in "antineutrino mode," where the secondary beam would then be π^-'s.) The primary decay mode of the pions is $\pi^+ \rightarrow \nu_\mu \mu^+$ (99.988% of the time). Since muons have a relatively long lifetime, most will reach the end of the decay region and be stopped by the 50 m absorber. Any that decay, however, will produce a ν_e that "contaminates" the pure ν_μ beam.

Although the secondary beam is mostly pions, there are also some kaons produced in the target. These are another source of ν_e contamination. To help constrain the kaon-induced ν_e background, a kaon monitor was installed just off-axis of the decay pipe. A 17 m long drift pipe intersects the main decay pipe roughly 10 m upstream of the 50 m absorber, leading to the kaon monitor – called the Little Muon Counter (LMC). It sits at an angle of 7º from the main decay region, and is designed to observe muons from K decay. These muons typically have higher energies and larger transverse momenta than muons from π decay, since the kaon mass is larger than the muon mass. Studies of the muons detected by the LMC will provide an important constraint on the number of ν_e's from kaons in the beam. A more detailed description of the LMC may be found in Ref. [71].
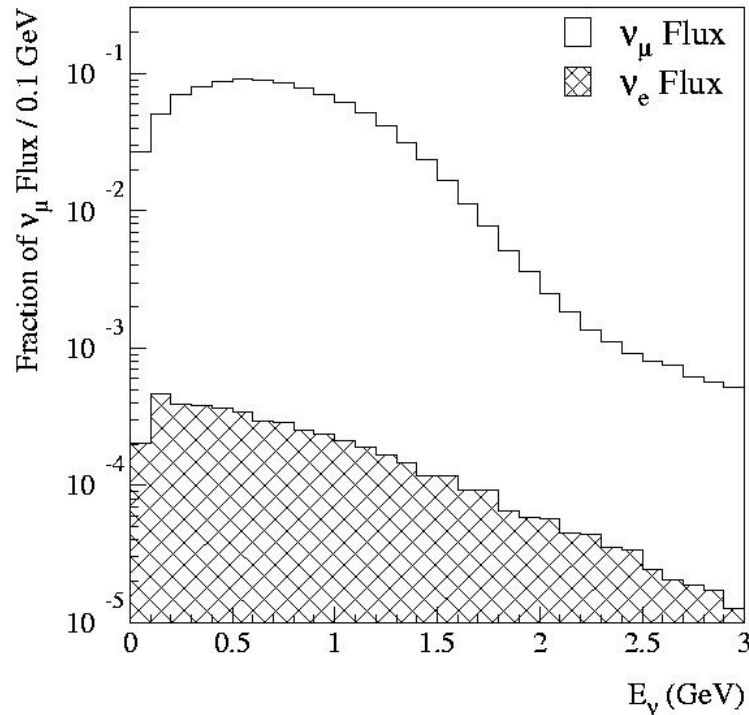
Figure 3.6: Predicted ν_μ and ν_e flux distributions as a function of neutrino energy in MiniBooNE.

3.2.4 Neutrino Flux

In creating a low energy neutrino beam, a compromise must be made between large numbers of interactions and low average energy. Higher energy neutrinos have a larger interaction cross section. This would provide a larger number of neutrino events, but also a larger number of background events. In particular, the two largest sources of background for the oscillation search, neutral current π^0's and intrinsic beam ν_e's, are larger at higher energies. This was an important consideration in determining the optimal beam energy for the experiment.

The predicted ν_μ and ν_e fluxes at a distance of 541 m from the target for a 6.1 m radius detector on the z-axis are shown in Fig. 3.6. The ν_μ spectrum peaks at 0.6 GeV, and the mean ν_μ energy is ~ 0.75 GeV. The intrinsic ν_e background is predicted to be 0.6% of the ν_μ flux. Discussion of the simulation that produced this distribution may be found in Chapter 4 and in Ref. [72].

Although some intrinsic ν_e flux is unavoidable, as described in the previous section, it is important to keep the relative amount as small as possible and well understood. The predicted energy dependence of this intrinsic ν_e background (hatched histogram in Fig. 3.6) is different than

the energy dependence an oscillation signal would have (ν_e's with a ν_μ-like energy dependence, unfilled histogram in figure). The shape difference between the two samples will help greatly in the oscillation search.

3.3   Detector
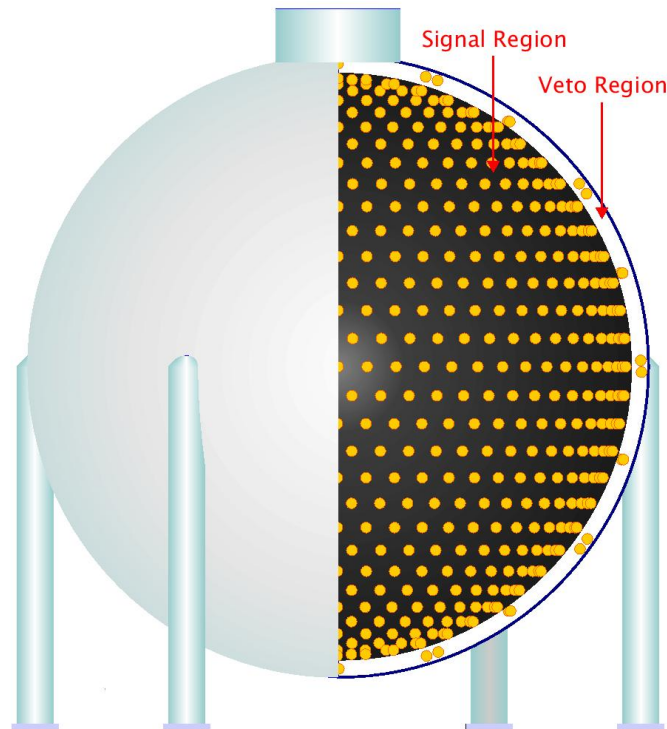
Figure 3.7: MiniBooNE detector with cut-away showing inner signal volume and outer veto shell.

The MiniBooNE detector, shown in Fig. 3.7, is a 6.1 m radius carbon steel sphere. An inner structure at 5.75 m radius supports 1280 8-inch Hamamatsu photomultiplier tubes (PMTs) that are pointed toward the center of the tank. These inner PMTs provide 10% coverage of the main detector region. The volume shell between the 5.75 m radius PMT support structure and the 6.1 m radius detector wall is the veto region. It identifies entering or exiting particles with 240 PMTs mounted on the inner wall of the detector.

A photograph of these two regions in the detector is shown in Fig. 3.8. Surfaces of the detector are painted to provide high reflectivity in the veto volume and low reflectivity in the main volume. Reflection of light in the main volume of the detector can cause Čerenkov light to appear isotropic

and delayed, like scintillation light. The effect of reflections would be degradation of particle identification; thus, surfaces in the main volume are painted black to be non-reflective. The veto volume is painted white to maximize the total light collected by the sparse array of photomultiplier tubes. The entire tank is filled with 807 tons of pure mineral oil; the usable volume for physics analyses is approximately 445 tons.
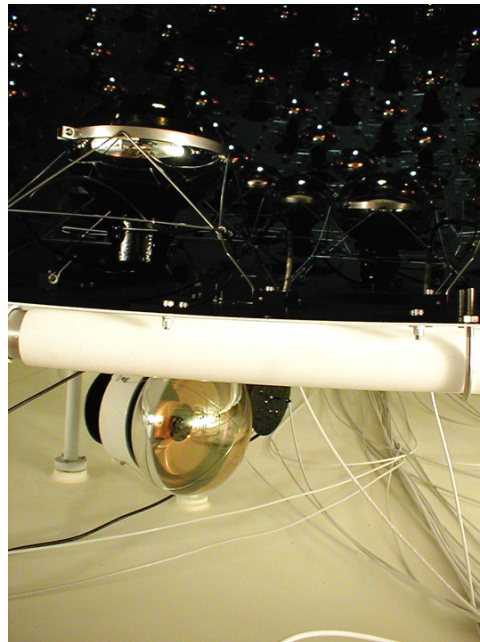
Figure 3.8: Photograph inside MiniBooNE detector. Black main tank region is separated from white veto region by phototube support structure.

The tank access and electronics area is situated directly above the detector vault, shown in Fig. 3.9. This area provides an open space for access to the opening at the top of the detector and to the tank vault. The detector building also contains the preamplifier electronics for the photomultiplier tubes as well as the data acquisition electronics. A raised floor houses a Faraday cage structure that surrounds the top access opening, providing a shielded area for the photomultiplier tube signal cables. Eight racks containing the preamplifier electronics sit atop the Faraday cage. The area beneath the raised floor is used to route cables from the preamplifier electronics to the data acquisition racks and to route cool air to the electronics racks from below.
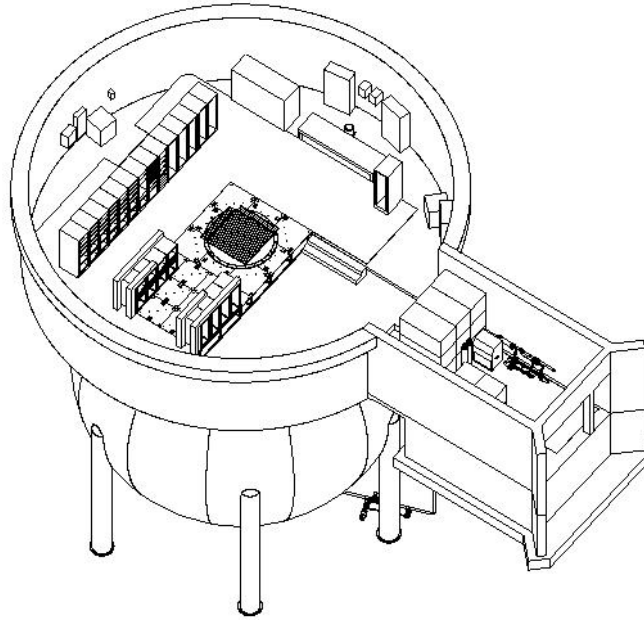
Figure 3.9: MiniBooNE detector plant [73]. Covering structures and earth overburden are not shown.

3.3.1 Overburden

An earth overburden covers the MiniBooNE detector building. The earth is formed into a truncated conical shape centered over the detector. The minimum earth equivalent that a cosmic ray particle must traverse to enter the detector is ~ 3 m, except in the region around the entrance to the building. This keeps the cosmic ray muon rate through the detector under 10 kHz. Since the neutrino beam is pulsed, arrival time of the beam is known precisely. Further shielding from cosmic rays arriving coincidentally with the beam is unnecessary.

3.3.2 Oil

Neutrino interactions in the detector occur primarily in the mineral oil, since $\sim 95\%$ of the detector tonnage is oil. The remaining volume is filled by the PMTs, their support structure, cables, and the steel of which the detector is made. Interactions with these other possible nuclear targets and with the dirt surrounding the detector are negligible after a fiducial volume requirement is applied in physics analyses.

The MiniBooNE detector system holds approximately 950,000 liters of oil. A request for bids

[74] was released on July 18, 2001, leading to submission of ten oil samples from six different vendors. The oil was required to be Light Mineral Oil (Industrial NF grade) with the following properties certified by the manufacturer

- Density: Specific gravity between 0.76 and 0.87 as measured via the American Society for Testing and Materials (ASTM) D 4052 or ASTM D 1298

- Viscosity: Less than 34.5 cSt at 40 °C as measured via ASTM D 445

- Color: Greater than or equal to 30 Saybolt Color units as measured via ASTM D 156

A more dense oil provides more interactions in the detector. The oil must be recirculated, however, which imposed an upper limit on the viscosity of the oil (and an implicit maximum density). In addition, it was important that the oil be clear to the light detected by the PMTs (wavelengths from 320 nm to 600 nm) [75], implying a minimum attenuation length.

Additional properties requested were high index of refraction, a small dispersion over the wavelength range 320 to 600 nm, low reactivity with materials in the detector, and a small amount of scintillation light. Based on these specifications and the results of testing performed, Marcol 7, an Exxon/Mobil product manufactured by Penreco, was chosen for the MiniBooNE detector. The results of measurements of the relevant oil properties are shown in Table 3.2.

Density	0.845 ± 0.001 g/cm^3
Refractive index (at $\lambda = 589.3$ nm, temp=20.0 °C) [76]	1.4684 ± 0.0002
Attenuation length (at 400 nm)	14 ± 2 m

Table 3.2: Results of some of the tested properties of MiniBooNE oil, Marcol 7.

The detector was filled, and may be recirculated, with the chosen oil via a pipe attached to a valve at the bottom of the detector. The inlet valve penetrates the tank wall; most of the oil is directed to the main volume of the tank via a coaxial fitting. This design was implemented because studies indicated that most of the oil circulation would occur in the veto region if oil were not supplied directly to the main volume. At the top of the detector is an overflow weir connected to an outlet that is routed to a stainless steel cylindrical overflow tank. The overflow tank has a 2500

gallon capacity ($\sim 1\%$ of the detector capacity), shown on the right side of Fig 3.10. This tank allows for thermal expansion of the oil in the detector and provides a means by which the oil can be recirculated. Its top is below the level of the mineral oil in the detector so that overflow oil from the detector will run to the overflow tank under the influence of gravity alone. There are pumps to move the oil from the overflow tank if necessary. The coefficient of expansion for mineral oil is about 0.1% per 1 °C. The overflow tank is kept 1/2 full; the allowed temperature range of the oil is about 10 °C.
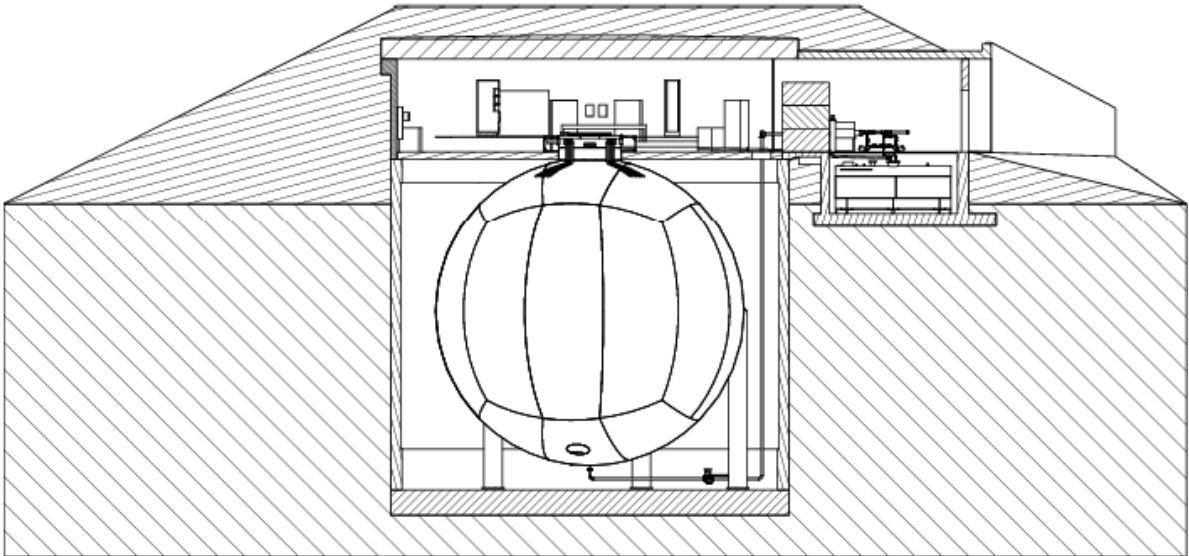
Figure 3.10: Elevation of MiniBooNE detector and building, showing overflow tank [73].

3.3.3 Photomultiplier Tubes

The inner region of the detector is lined with 1280 8-inch photomultiplier tubes. These PMTs collect light from neutrino interactions occurring in the inner detector region. The outer veto region holds another 240 PMTs, positioned to maximize detection of light produced during interactions of charged particles entering from outside the detector, such as cosmic rays. Of the 1520 PMTs in the MiniBooNE detector, 1197 are inherited from LSND and the other 323 were purchased from Hamamatsu [77]. The LSND PMTs are 8-inch diameter, 9-stage, Hamamatsu model R1408 PMTs; the new PMTs are 8-inch, 10-stage, Hamamatsu model R5912 PMTs – an upgraded version of the R1408. The technical specifications for both of these types of photomultiplier tubes may be found in Ref. [78].

Each PMT was tested prior to installation in the detector to characterize its charge and timing response [79], and to determine its proper operating voltage. Dark current, time jitter, charge resolution, double-pulsing, and pulse shape were also recorded for each PMT.

The main signal region of the detector is instrumented with all of the R5912 PMTs and those R1408 PMTs whose test results showed the best performance. The remaining R1408 PMTs are mounted in the veto region, where performance requirements are less stringent. Each PMT in the signal region is affixed in its location with a wire frame whose feet are anchored to the phototube support structure (PSS). A schematic diagram of a PMT in its wire frame is shown in Fig. 3.11.
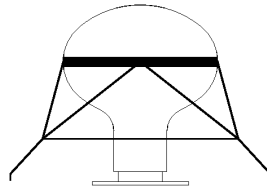
Figure 3.11: The wire support frame used to attach PMTs in the main tank region of the detector [73].

The PMTs are arranged in the detector in the pattern shown in Fig. 3.12. This map uses a projection where distance along the tank wall is preserved.
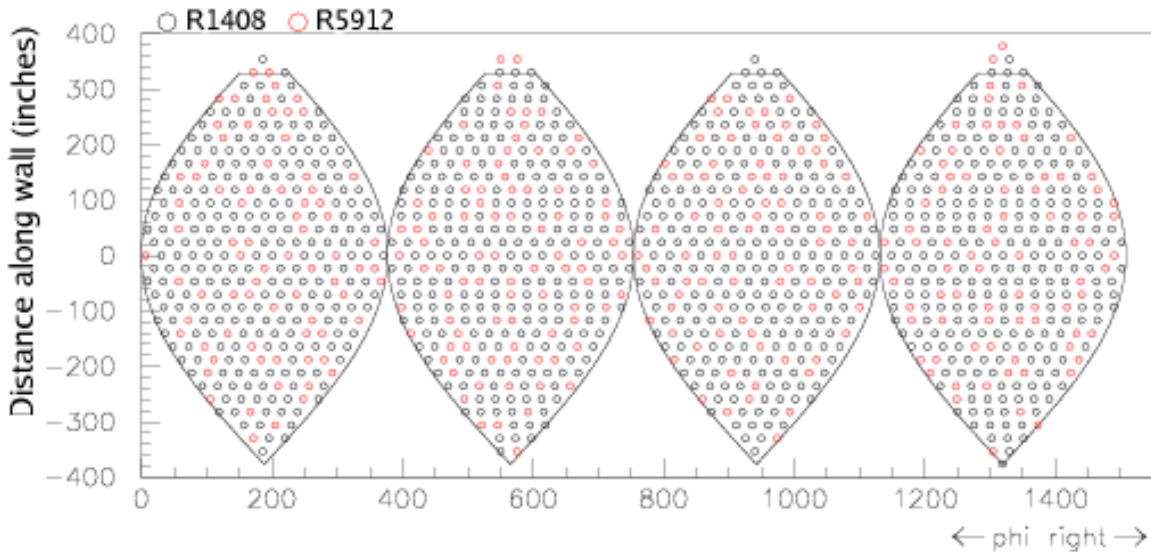
Figure 3.12: Map of PMT locations in main tank. LSND PMTs (R1408) shown in black, new PMTs (R5912) in red.

3.4 Data Acquisition & Triggering

Much like the majority of the PMTs, the MiniBooNE data acquisition system (DAQ) is built from existing LSND hardware. It works on the same principles, but has been modified to meet the different needs of MiniBooNE. Signals from each PMT travel via a single coaxial cable to the electronics area, where they are "picked off" in the circuitry of the HV/pre-amp cards and sent to the DAQ. The coaxial cables are routed through the veto region of the detector to a light-tight exit port in the tophat.

The PMTs are operated at an average of 1800 V, but individual voltages are set for each PMT to ensure a roughly uniform gain throughout the detector. The amount of voltage each PMT receives is regulated by a step-down resistor located on a preamplifier card in the electronics area above the detector. PMT signals are amplified and integrated. Instead of performing a full digitization of the PMT signal waveforms, the integrated charge (Q) and time (T) are digitized every 100 ns, where we define 100 ns as a "clock tick."

A schematic representation of the digitization for one channel is shown in Fig. 3.13. The pre-amplified PMT signal, V_{pmt}, is integrated in a capacitive circuit located on a charge/time board (QT board), generating a second signal, V_q. If V_{pmt} crosses a threshold corresponding to approximately 0.25 photoelectrons, a discriminator is fired, starting a linear time ramp (V_t). The time signal is also digitized to allow a precise determination of the time at which the PMT signal crossed the threshold. This is necessary since MiniBooNE event reconstruction requires better than 100 ns time accuracy. Two clock ticks after the PMT signal crosses threshold, the time ramp is reset to baseline.

The entire QT system consists of 12 VME crates. Each crate contains 16 cards with 8 channels per card, resulting in 1536 available channels to serve the 1520 PMTs in the detector. There are 10 crates for "tank" PMTs and the 2 remaining crates host the veto PMT channels. Fig. 3.14 shows a schematic diagram of the circuitry for a single PMT channel. Each channel digitizes the charge and time information for a particular PMT and stores the information in a circular buffer (dual-port sRAM) at an address determined by the 11 bits of the 10 MHz system clock. This address is known as the time-stamp address (TSA). The data are continuously digitized and written to the circular buffer, which wraps around every 2048×100 ns $= 204.8$ μs. Data are read from the circular buffer
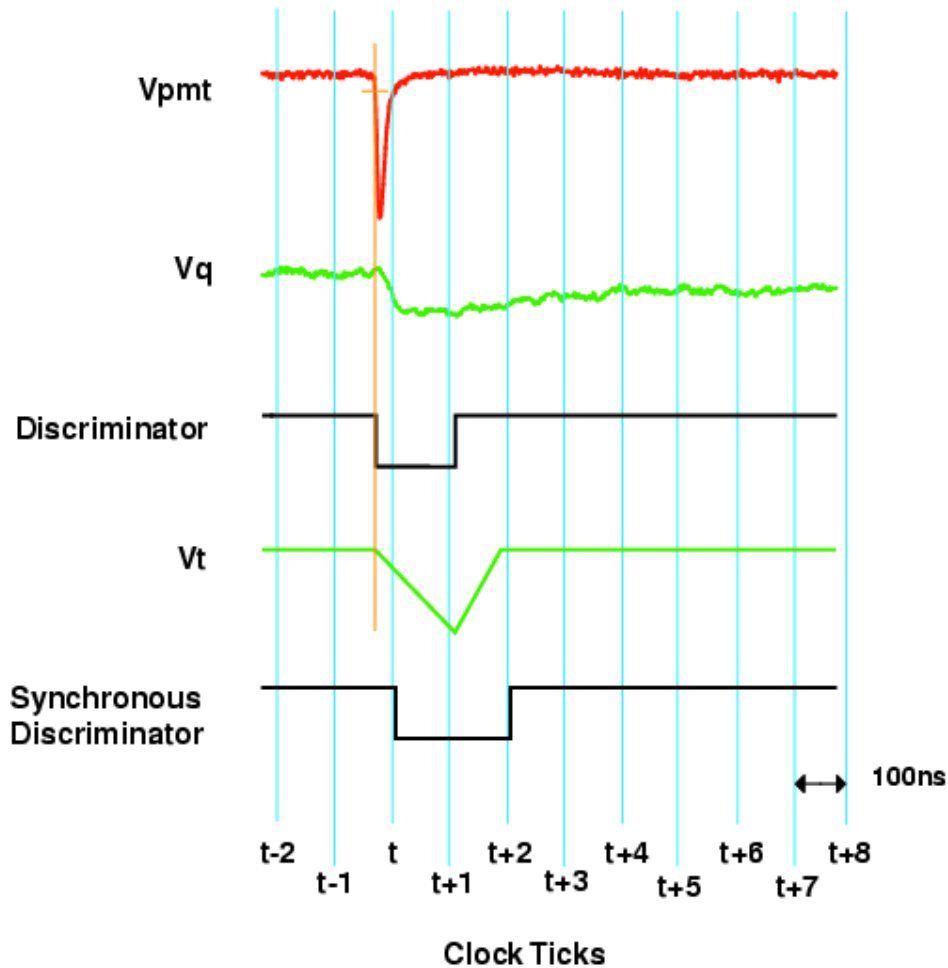
Figure 3.13: Schematic representation of MiniBooNE PMT charge and time digitization [73].

for TSAs that are requested by the trigger.

If the trigger decision is too slow ($> 204.8\mu s$) in asking for data from a particular set of TSAs, the circular buffer will be overwritten, and the data of interest will be lost. A latency filter is applied to all analyzed data to reject beam events in which this occurs [80]. This will be discussed again in Section 5.1. The fraction of beam events rejected by this filter is typically a few tenths of a percent.

The triggering system examines bit patterns to determine whether or not a particular DAQ time window (set of TSAs) should be read out from the circular buffer. Each VME crate contains a single-board computer (SBC) in addition to its 16 QT cards. When trigger conditions are met, the data from the TSAs of interest are retrieved from the circular buffer and loaded into a QT FIFO memory. The 128 channels of data in each VME crate are retrieved by the SBC via the VME bus,

zero-suppressed in software, and shipped to the DAQ host computer (called hal9000[1]) where they are assembled and written to disk.
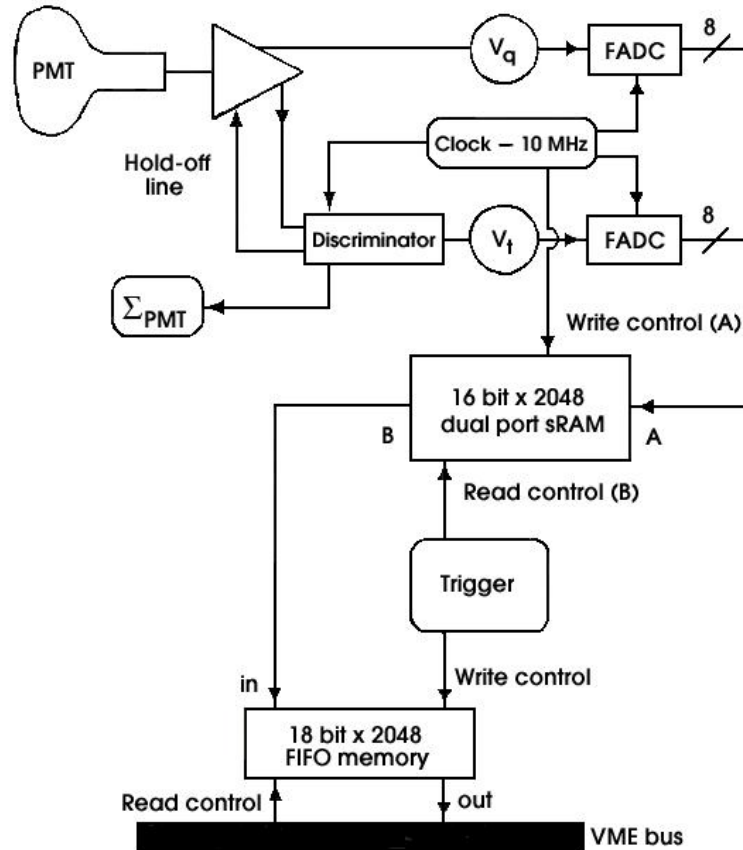
Figure 3.14: Schematic diagram of data acquisition electronics for a single PMT channel [73].

Each QT crate also contains a PMT sum card which counts the number of channels that caused the discriminator to fire in the last 2 clock cycles (200 ns). This information is routed to the trigger crate, which contains "main" and "veto" sum cards. These cards take the "sum of sums" for main and veto crates separately to give an overall number of PMT signals in the main and veto regions of the detector.

3.4.1   Trigger Conditions

There are a number of different hardware triggers, both internal and external, that cause data to be written to disk. Internal triggers are based on information from the main and veto sum cards

---

[1]Any resemblance to fictional characters living or dead was completely intentional. However, our hal9000 has never locked us out of the detector building. Yet.

Trigger bit	Threshold
DET1	Tank hits ≥ 10
DET2	Tank hits ≥ 24
DET3	Tank hits ≥ 200
DET4	Tank hits ≥ 100
DET5	Tank hits ≥ 60
VETO1	Veto hits ≥ 6
VETO2	Veto hits ≥ 4

Table 3.3: Internal trigger bits and their thresholds.

in the trigger crate. The external triggers assert bits in the trigger memory by way of 4 BNC connections on the front of the trigger card.

There are 7 internal hardware trigger bits (DET1-DET5, VETO1, and VETO2). These bits are asserted if simple requirements are met, *e.g.*, the main (veto) sum card indicates the presence of a minimum number of PMT signals in the main (veto) detector region. Table 3.3 shows the 7 internal trigger bits and the thresholds above which they are asserted.

The 3 broad categories of external trigger are beam, strobe, and calibration. External trigger signals (labelled $E1 - E4$) are input on the front of the trigger card, as mentioned above. The beam trigger takes precedence over all other triggers. All neutrino-induced events described in following sections are based on this trigger condition.

- **Beam trigger (E1)** – Booster timing information is transmitted to all areas of the Fermilab complex by way of fiber optics. Two timing signals from the Booster are relevant for the MiniBooNE beam trigger: "1D" and "1F" (named as 2-digit hexadecimal numbers). A 1D indicates the Booster is preparing for a beam pulse to MiniBooNE. This signal is sent 35 ms before the 1F signal. A 1F is the Booster extraction synchronization signal. It precedes the extraction kick by 320 μs, and the beam takes $1-2$ μs to travel to the target. Fig. 3.15 shows the relationship between 1D and 1F signals and the trigger TTL signals initiated by them. A coincidence of TTL 1 and TTL 2 sets the MiniBooNE beam trigger E1 bit. The duration of the beam spill is 1.6 μs, and TSAs corresponding to 19.2 μs are written to disk, starting

4.6 μs before the neutrinos arrive at the detector.
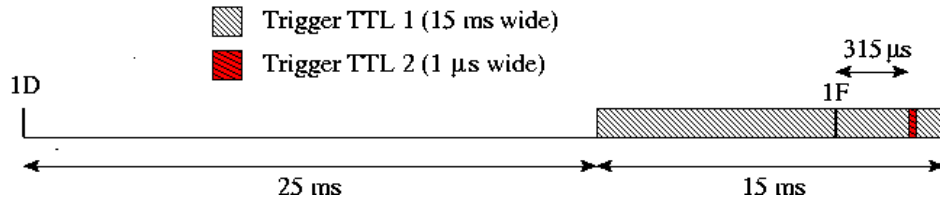
Figure 3.15: Booster timing signals "1D" and "1F" used in MiniBooNE beam trigger.

- **Strobe trigger (E2)** – This trigger bit is shared by the strobe, debuncher, follower, and NuMI triggers based on the width of the NIM pulse sent from the E2 bit into the trigger. In a strobe event, the trigger requests 19.2 μs of detector activity based on signals from a pulse generator set to a frequency of 2.01 Hz, allowing for unbiased studies of detector activity when no beam is delivered. Debuncher events are triggered on a signal from the accelerator complex indicating that beam is about to be injected to the target at the anti-proton source. Follower events are delayed 20 μs from a beam or strobe event, designed to look for neutron capture and other events associated with a neutrino event. NuMI events are due to off-axis decays in the NuMI tunnel[2], and decay at rest of π's and K's at the NuMI dump (located directly below MiniBooNE). Details of the NuMI trigger design may be found in Ref. [81].

E2 trigger type	Width of E2 pulse	Activity
FOLLOWER	150 ns	Single pulse delayed 20μs from beam or strobe.
STROBE	350 ns	19.2μs of detector activity.
DEBUNCHER	550 ns	Triggered on signal \$81 from accelerator complex (beam injected to target at anti-proton source)
NuMI	750 ns	Open window to look for events from NuMI ν's

Table 3.4: E2 external trigger bit sub-categories.

---

[2]Details of the NuMI/MINOS experiment may be found at `http://www-numi.fnal.gov/`

- **Calibration trigger (E3)** – This trigger bit is also shared by several triggers. There are four types of calibration events, shown in Table 3.5.

Calibration type	Width of E3 pulse	Activity
CALIB_CUBE	150 ns	Cube trigger
CALIB_LASER	450 ns	Laser trigger
CALIB_TRACKER	650 ns	4-plane tracker coincidence OR cube + tracker
CALIB_BEAM	850 ns	Laser in time with non-MiniBooNE Booster shot

Table 3.5: E3 external trigger bit sub-categories.

- **Hardware 'OR' (E4)** – The E4 bit is a NIM hardware OR of the E1-E3 bits and the internal bits. If the E4 bit is asserted, the trigger registers the time and the current state (on or off) of ALL comparator and E-bit settings..

Various logical combinations of these bits are used to form software trigger windows and hold-offs. See Appendix A for more details of these trigger designations.

When a trigger condition is met, the following information is written to disk for each PMT channel: the clock tick number that occurred just before the discriminator fired ($t-1$ in Fig. 3.13, and the "quad" for that event (four digitized V_q values and their corresponding V_t's). This is not to say that only one quad may be written for each event; multiple quads are written for events in which the trigger requests a larger time window. In the case that the electronics channel for a PMT is saturated with charge ($\gtrsim 20$ PEs), the full event cannot be reconstructed with only one quad of information. A variation on the quad scheme is used in this case; concatenation of consecutive quads (in software) allows for full retrieval of the event information.

3.5 Detector Calibration

The data acquisition system records raw times and charges for each hit in an event, allowing for measurement of the intrinsic charge and time resolution of the PMTs without effects of smearing associated with the DAQ itself. This smearing makes it necessary to have a calibration system to provide information on PMT charge and time response as well as energy response of the detector. Since a particle's energy is determined by the number of photoelectrons detected by the PMTs, it is critical that the PMTs be properly calibrated. Not only is it important to know the relative time response of PMTs, but also the variation of time response with pulse height (time slewing). These are crucial for the event reconstruction and particle identification algorithms.

Calibrations are performed using two different apparatus [3]: the laser calibration system, and the cosmic ray muon calibration system.

3.5.1 Laser Calibration System

The MiniBooNE laser calibration system consists of a pulsed diode laser and four dispersion flasks. Short pulses of laser light are transmitted via optical fibers to each of the dispersion flasks installed at various locations in the detector. This system is used primarily to quantify and monitor individual PMT properties such as gain and timing. It also allows for *in situ* monitoring of the oil attenuation length over the lifetime of the experiment. A schematic diagram of the laser/flask system is shown in Fig. 3.16.

The diode laser generates pulses with widths ≤ 100 ps. A switch box allows transmission of the laser light pulses to one of the four dispersion flasks via an optical fiber. The laser system is pulsed at 3.3 Hz continuously and asynchronously with the accelerator during normal data-taking. Each dispersion flask is 10 cm in diameter, filled with a dispersive medium called Ludox®. Laser light sent to a flask illuminates all of the PMTs with roughly equal intensities.

In addition to the four flasks, there is a bare fifth optical fiber that emits light in a cone of $\sim 10°$, illuminating PMTs in a small circle near the bottom of the detector. It is used to study light scattering in the detector. The locations of the four flasks and the bare fiber are shown in

---

[3]Don't you think "apparati" should be a word?
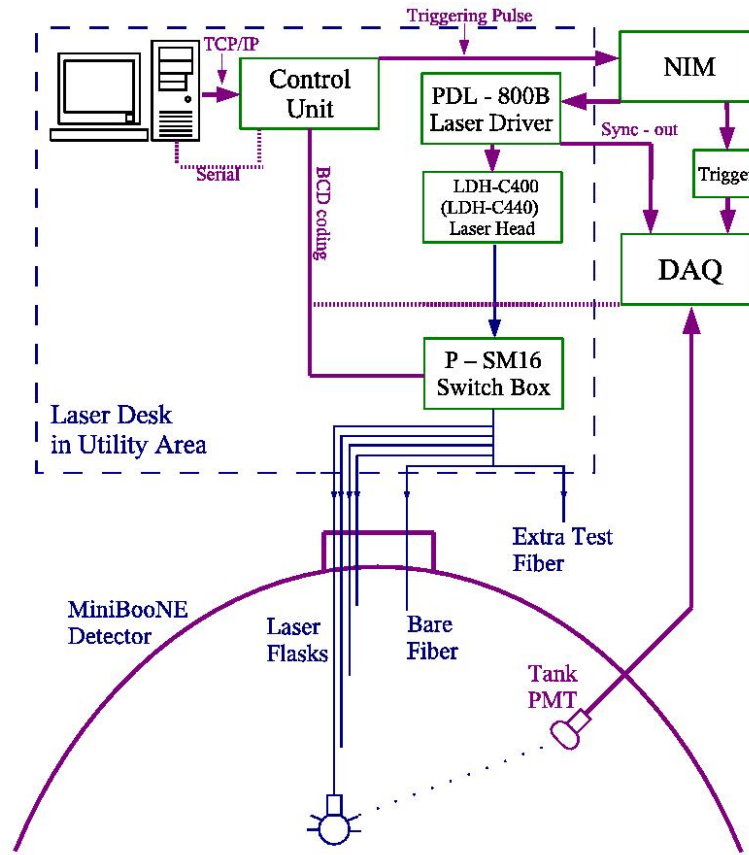
Figure 3.16: MiniBooNE laser calibration system [82].

Table 3.6, where the origin is at the center of the detector, and positions are quoted in beam coordinates (z-axis along beam direction, y-axis toward detector tophat).

PMT Gain and Timing Calibration

The gains of individual PMTs are resolved by fitting the single photoelectron peak for each PMT in low light intensity runs. Time slewing corrections are needed to account for the fact that larger PMT signals fire the discriminator earlier than smaller signals. These corrections are calculated separately for R1408 PMTs and R5912 PMTs using timing information from the relevant PMT channels for runs covering a range of light levels. The gains and slewing corrections are stored in look-up tables; new tables are produced approximately every four days.

As discussed earlier, the raw data consist of "quads," the uncalibrated charges and times associated with TSAs for a particular hit as well as an offset that gives the timing of the first TSA in the quad relative to the beginning of the event. The calibration algorithm takes the raw values

Device	x (cm)	y (cm)	z (cm)	radius (cm)
Flask 1	-0.3	-4.1	1.5	4.4
Flask 2	144.9	96.1	-126.4	215.0
Flask 3	1.7	-0.8	83.7	83.7
Flask 4	-80.0	203.9	-24.1	220.3
Bare fiber	82.0	540.0	65.0	550.0

Table 3.6: Laser flask and bare fiber positions in beam coordinates (z along beam, y toward tophat, $\tan\phi = z/x$).

for each quad (reported in ADC counts) and transforms them into charges (in photoelectrons) and times (in ns).

A brief, simplified overview of the method is given here. For more detail, please see Ref. [83]. The first step in the procedure uses the first three T_{ADC} values of the quad (see Fig. 3.13) to determine t_{raw}, the raw time (in ns) that the discriminator fired relative to the clocktick that preceded it. Since a hit in the detector produces a known, measured charge shape, $V_{\mathrm{q}}(t)$, on the QT board, the newly determined raw time can be used to determine which points along the $V_{\mathrm{q}}(t)$ curve correspond to the digitized Q_{ADC} values. The raw charges, q_{raw}, are determined by finding the normalization of $V_q(t)$ that best fits the Q_{ADC}s associated with that hit. A charge-dependent time slewing correction, $t_{\mathrm{slew}}(q)$, is then read from a lookup table using the raw charge determined in the previous step. In the final step, the calibrated hit time and charge are calculated as:

$$t = t_{\mathrm{raw}} + t_{\mathrm{slew}}(q_{\mathrm{raw}}) + t_{\mathrm{offset}} + t_{\mathrm{start}}$$
$$q = \frac{q_{\mathrm{raw}}}{\mathrm{gain}}$$

(3.1)

where t_{offset} is a PMT-dependent calibration constant that accounts for timing differences due to differing cable lengths and dynode structures and t_{start} is the coarse time (a multiple of 100 ns) from the beginning of the event to the clocktick that precedes the discriminator firing.

These calibrations are performed primarily with the flask located at the center of the detector, but the calibrations are cross-checked using the other three flasks and a sample of electrons from cosmic muon decay. The corrected time distribution for R5912 PMTs is shown in Fig. 3.17 with a

logarithmic vertical scale to enhance important features, such as scattering, that will be discussed further in Section 3.6.
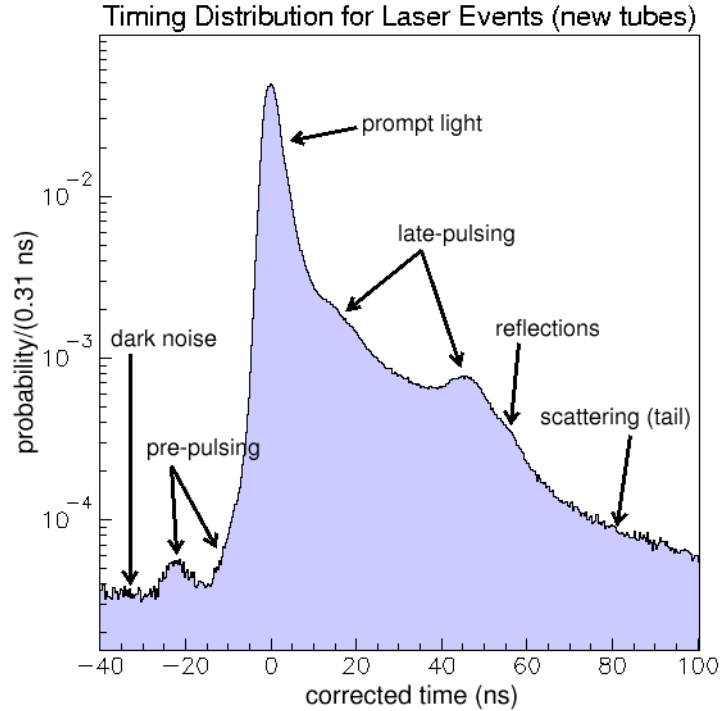
Figure 3.17:   Corrected timing distribution of R5912 PMTs for light from laser flask 1.

3.5.2   Cosmic Ray Muon Calibration System

The cosmic ray muon calibration system consists of a muon tracker located above the detector, and scintillator cubes located inside the detector. This system uses through-going muons as well as stopping muons and their decay electrons. The stopping muons providing a sample with known direction and path length.

The muon tracker is a 2 layer scintillator hodoscope that determines the positions and directions of muons entering the detector. It is divided into 2 sets of 2 layers, providing two sets of coordinates by which the position and direction may be determined. Seven optically isolated cubes made of scintillator are situated at various positions (detailed in Table 3.7) in the main volume of the detector, providing additional information for those muons which traverse or stop in them. An optical fiber joined to each scintillator cube is attached at its other end to a 1-inch PMT located

outside of the detector.

Device	x (cm)	y (cm)	z (cm)	radius (cm)
Cube 1	-18.6	371.2	59.2	376.4
Cube 2	40.8	170.1	44.5	180.5
Cube 3	40.8	273.9	44.5	280.5
Cube 4	15.6	511.7	-57.6	515.2
Cube 5	-60.8	540.7	15.1	544.3
Cube 6	-45.2	538.1	-36.9	541.3
Cube 7	57.9	471.5	-13.5	475.2

Table 3.7: Scintillator cube positions in beam coordinates (z along beam, y toward tophat, $\tan \phi = z/x$).

Fig. 3.18 shows a schematic diagram of the system for a muon which passes through the muon tracker, stops in a scintillation cube, and decays. This calibration system provides a precise calibration of the energy, direction, and position of muons for the range of muon energies of primary interest to the experiment (60 to 800 MeV).

A muon that stops in a cube and decays, producing an electron, will have a distinct signature of two light pulses in time-delayed coincidence. Since the cubes are only a few centimeters on a side, the stopping position of these muons is known to an accuracy of a few centimeters. The starting position can be determined with similar accuracy using the muon tracker. Once the range is known, the muon energy may be determined to $\sim 3\%$ [84]. This energy resolution is dominated by fluctuations in energy loss (range straggling).

Approximately 1000 muons per month stop in each cube; about half of these have clean muon and electron signals separated by more than 1 μs [82]. The uncertainty in the muon energies in these samples are almost entirely due to range straggling, and the absolute energy determination for these events is between 1% and 2% for $E_\mu > 200$ MeV.
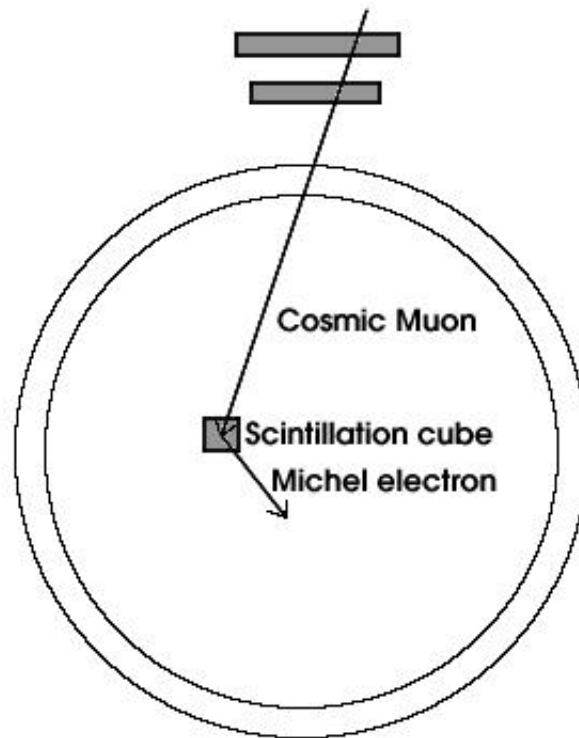
Figure 3.18: A schematic diagram of the muon tracker and a scintillation cube.

Absolute Energy Calibration

The energy distribution of electrons from the decay of stopped muons (Michel electrons) is well known; the measured energy distribution of these electrons, shown in Fig. 3.19, may be used to determine both the energy scale and energy resolution for low energy electrons. Large samples of Michel electrons, from both stopping cosmic ray muons and muons produced in neutrino interactions, have been collected and analyzed. The measured energy resolution from this large dataset is 14.8% at 52.8 MeV. The Michel electrons provide a very useful calibration of the energy scale and resolution at the low end of the energy region of interest to MiniBooNE.

In addition to its usefulness in determining the absolute energy calibration of the detector, the cosmic muon calibration system is also used to study the detector oil optical model. It provides a clean sample of muons whose exact event topologies are known through measurements that are independent of the PMTs in the detector. This allows a careful study of the space and timing characteristics of photon emissions from muons spanning a broad range of energies ($15-800$ MeV).
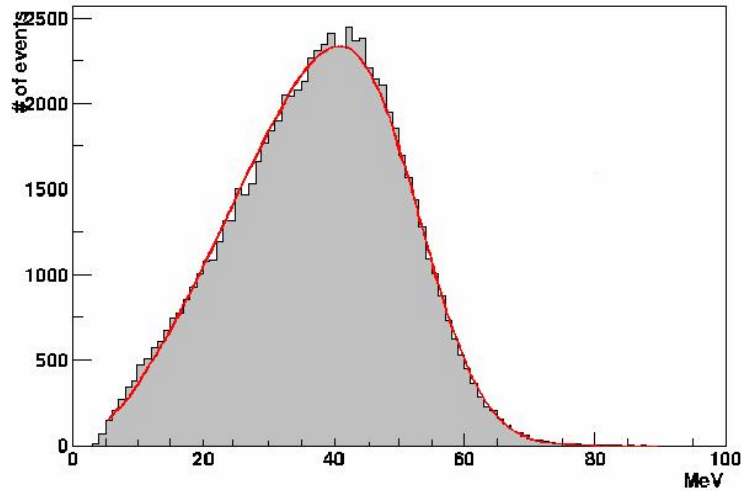
Figure 3.19: The observed Michel electron energy distribution (histogram) compared to a best fit curve (solid line) obtained by smearing the theoretical energy distribution with a Gaussian whose width is proportional to $\sqrt{E}$. The energy resolution determined from the fit is 14.8% at 50 MeV.

3.6 Detector Response

The photomultiplier tubes detect both Čerenkov and scintillation photons produced by charged particle interactions in the detector. They are sensitive to photons in the wavelength range $\sim$ 300 nm $< \lambda <$ 650 nm

3.6.1 Čerenkov Light

Čerenkov light is produced in a medium with index of refraction n, when a charged particle travels faster than the speed of light in that medium. Since the speed of light in a medium is dependent upon its index of refraction, the particle must travel with speed $\beta > 1/n$, where $\beta = v/c$, the speed of the particle divided by the speed of light in vacuum. In these circumstances, a cone of light is emitted with the following property:

$$\cos\theta_C = \frac{1}{n\beta}. \tag{3.2}$$

A schematic representation of Čerenkov radiation is shown in Fig. 3.20.

The amount of Čerenkov radiated light is given by

$$\frac{d^2N}{dxd\lambda} = \frac{2\pi\alpha z^2}{\lambda^2}\left(1 - \frac{1}{\beta^2 n^2(\lambda)}\right) = \frac{2\pi\alpha z^2}{\lambda^2}\sin^2\theta_C, \tag{3.3}$$
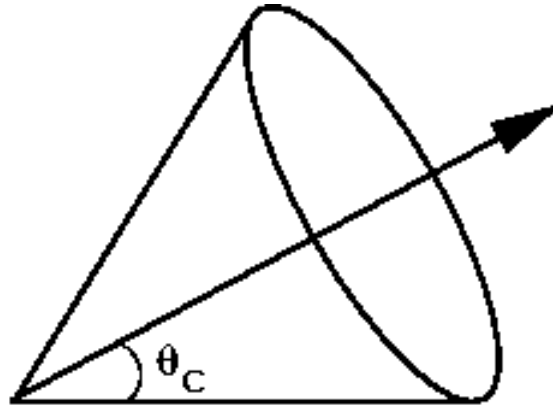
Figure 3.20: Čerenkov radiation.

where $\alpha = e^2/(\hbar c)$ is the fine structure constant, ze is the particle's charge, x is the particle's path length, and λ is the wavelength of emitted light [5]. The index of refraction as a function of wavelength has been studied for Marcol 7 mineral oil at a temperature of 20 ± 0.1 °C [75, 76], and may be described by a Cauchy expansion

$$n(\lambda) = n_D + B \left(\frac{1}{\lambda^2} - \frac{1}{\lambda_D^2} \right) \tag{3.4}$$

where λ is the photon wavelength in nm in air, $\lambda_D = 589.3$ nm is a Fraunhofer D line of the sodium doublet, $n_D = 1.4684 \pm 0.0002$ is the refractive index at λ_D, and the parameter $B = (4240 \pm 157)$ nm^2. Fig. 3.21 shows the measured wavelength dependence of the refractive index; the two lines are the upper and lower error bounds on the measurement.

3.6.2   Scintillation Light and Fluorescence

In addition to the Čerenkov light, charged particles travelling through mineral oil deposit energy, which has the effect of exciting electron states of oil molecules in their path. The isotropic, delayed light that is emitted during de-excitation of the molecules is called scintillation light.

Fluorescence is a related process, where the molecular electron states are excited by optical photons instead of charged particles. As with scintillation light, the fluorescence light produced during the de-excitation of the target molecules is isotropic and delayed. The outgoing photons have longer wavelengths than the initial optical photons that excited the molecule.

In both cases, the emission wavelength and time spectra are dependent on the chemical composition and molecular structure of the mineral oil. These spectra have been studied experimentally
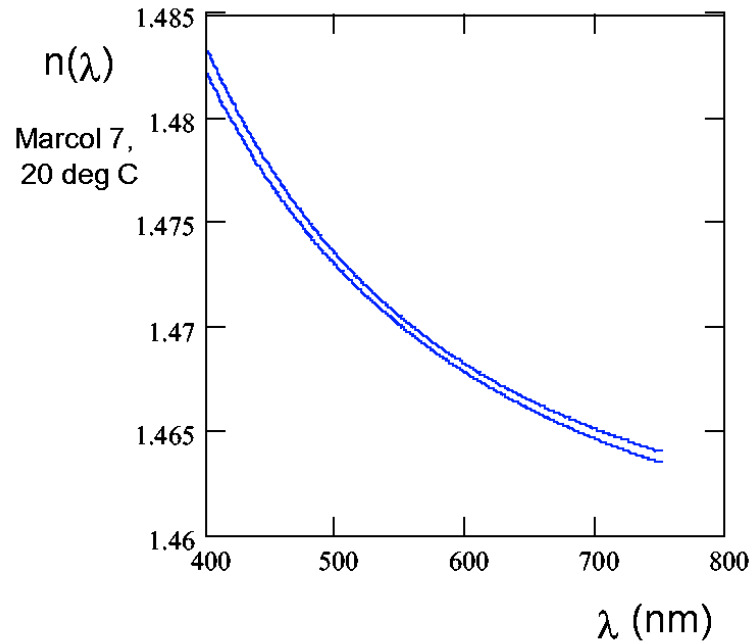
Figure 3.21: Measured index of refraction as a function of wavelength for Marcol 7 mineral oil at 20 ± 0.1 °C.

for Marcol 7 mineral oil.

Scintillation and fluorescence light in mineral oil do not follow the dE/dx energy loss distribution expected from particles passing through matter. Instead, the light yield is lower (energy loss higher) due to recombination and quenching effects between excited molecules [85]. The distribution can be described by

$$\frac{dE'}{dx} = \frac{dE/dx}{1 + k_B(dE/dx)} \tag{3.5}$$

where $k_B = 0.014$ g/(MeV cm^2) is Birk's constant for mineral oil [86].

Both *in situ* and *ex situ* measurements of the scintillation and fluorescence properties of Marcol 7 have been performed. These include measurements of scattering length, Rayleigh and Raman scattering wavelength dependence, compressibility, scintillation strength and time spectra, time-resolved fluorescence, fluorescence excitation and emission spectra, and extinction rates in the oil.

Scattering measurements

Scattering is defined as the deflection of optical photons; it is due to interactions with molecules in the oil. The two main types of scattering seen in Marcol 7 are Rayleigh and Raman scattering.

Rayleigh scattering is caused by thermodynamic fluctuations in the mineral oil that can cause light to scatter if there are local changes in the optical properties of the oil. This scattering that arises from density perturbations does not change the wavelength of the photons. In contrast, Raman scattering results in wavelengths that are red-shifted with respect to the initial photon wavelength because some of the photon's energy is lost to vibrational or rotational excitation. Neither of these types of scattering should be confused with scattering due to particulate contamination in the oil.

Scattering was first seen as a late-time tail in a timing distribution of light from laser flask 1 (see Table 3.6) in the detector, shown in Fig. 3.17. The initial study of this timing feature was performed *in situ* by the Louisiana State University (LSU) group, who used unpolarized 397 nm laser light with the bare fiber in the detector [87]. The angular distribution of the scattered light was seen to be consistent with Rayleigh scattering in this study. Further investigation of the scattering was undertaken by the Princeton group using a goniometer [88]. This more in-depth *ex situ* measurement verified the expected angular distribution of scattered light for polarized incident light of wavelengths 442 nm and 532 nm. The relative amounts of Rayleigh scattering from isotropic density fluctuations and Rayleigh scattering from anisotropic density fluctuations, integrated over all angles, was found to be 1:0.27 at these two wavelengths. In order to extend the study, additional measurements were made by the Fermilab Scintillation Detector Development Group using a spectrophotometer [89]. Here, in addition to the Rayleigh scattering seen by the Princeton group, Raman scattering was also measured at 90 degrees to the incident light. The ratio of overall Rayleigh to Raman scattering at this angle was measured to be approximately 1:0.04. After correcting for the angular distributions of both the Rayleigh and the Raman scattering, the dominant contribution to scattering in the MiniBooNE oil was found to arise from isotropic Rayleigh scattering ($\sim 75\%$), while anisotropic Rayleigh scattering was found to contribute $\sim 20\%$ and Raman scattering $\sim 5\%$.

Fluorescence measurements

Fluorescence occurs when a molecule absorbs a photon, resulting in an excited electron state of the molecule which returns to its initial state by emitting a longer wavelength photon. For this reason, various "fluors" are sometimes intentionally added to a scintillating material in order to shift the

wavelength of the scintillation light. Although this is not the case for MiniBooNE oil, no less than three fluorescent species ("fluorophores") have been identified for 285 nm excitation light[4] in the Marcol 7 [90].

The time-resolved fluorescence measurements were carried out at Johns Hopkins University using a 285 nm pulsed laser [90]. The emitted light intensity was recorded at 32 distinct wavelengths (from 295 nm to 450 nm in 5 nm steps) for 10 minutes at each wavelength. A global fit was performed on the 32 resulting datasets, allowing multiple exponential hypotheses. One of the fluorophores is known to be Vitamin E (whose time-resolved fluorescence emission is best described by two decay lifetimes: the primary $\tau = 1.16$ ns, and secondary $\tau = 0.41$ ns), which is added to the mineral oil by the manufacturer as an antioxidant and stabilizer.

In addition to time-resolved measurements, emission and excitation fluorescence spectra were recorded for the oil. For a given excitation wavelength, the fluorescence spectrum was recorded for a range of emission wavelengths. Simlarly, for a given emission wavelength, the intensity of the fluorescence was recorded for a range of excitation wavelengths. An example of the measured emission spectrum for 300 nm excitation light is shown in Fig. 3.22.

De-oxygenating typically increases the intensity of fluorescence by depopulating electronically excited states of fluorescent molecules. However, deoxygenation tests in the Marcol 7 showed less than a 1% effect, in agreement with predictions from studies of the solubility of O_2 in mineral oil [91].

Scintillation measurements

Measurements of the scintillation properties of the Marcol 7 were made using two different methods. The first measurements were conducted at the Indiana University Cyclotron Facility (IUCF), where the ionization loss of 180 MeV protons (below the 341 MeV Čerenkov threshold) in the oil was studied. Results from these studies showed scintillation light with a timing constant of $\tau \sim 19$ ns.

---

[4]The phrase "no less than three" is used because time-resolved spectroscopy is used to identify fluorophores by fitting the output light intensity as a function of time with multiple exponential functions. The time-resolved fluorescence intensity for a single fluorophore is often found to require more than one exponential function to accurately describe the spectrum. In the case of Marcol 7, a fit with six exponentials describes the data well; including seven or more exponentials also works well but returns lifetimes that are shorter than the time resolution of the instrument.
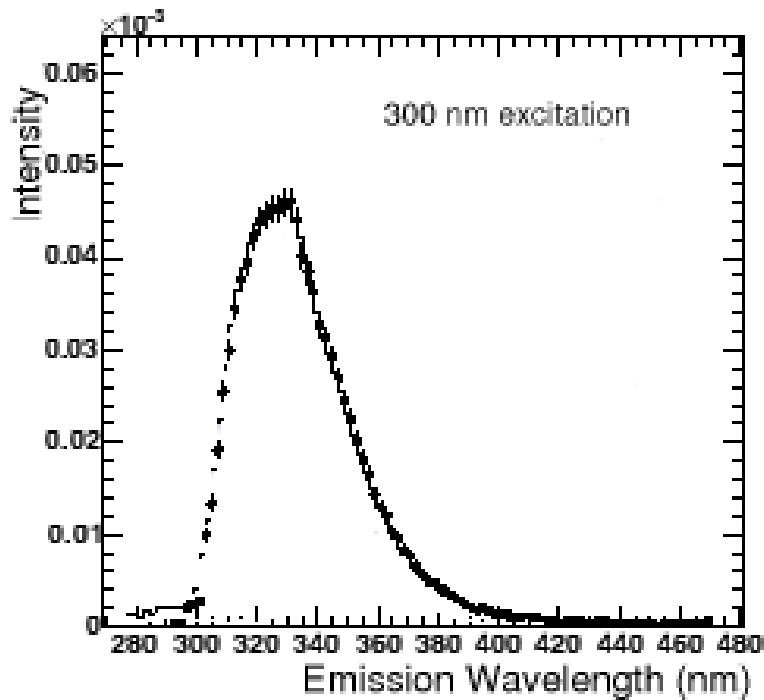
Figure 3.22: Intensity of emitted fluorescence as a function of wavelength for 300 nm excitation light.

A complementary set of measurements were made with cosmic ray muons using a scintillation test chamber designed by Narumon Suwonjandee and Randy Johnson [92]. Fits to the cosmic ray data were also found to have a timing constant of $\tau \sim 19$ ns. As a further check, this test device was taken to IUCF and placed in the proton beam, where the results were also found to be in agreement with results from the original IUCF test apparatus.

3.6.3   Attenuation Length

The initial studies of attenuation length (extinction) in the oil were performed with an apparatus which scanned a range of wavelengths and measured the relative transmission of light through a 1.6 meter sample of oil. A second device was used to determine the absolute attenuation length by varying the path length of oil through which 460 nm light was directed [93]. The combined results of these two tests were used to decide which oil to use in the MiniBooNE detector. A detailed explanation of the 1.6 meter test device may be found in Appendix B.

Since the range and application of these two devices was limited, further tests were performed

by both the Fermilab Scintillation Detector Development Group (FNAL) and the Johns Hopkins University group (JHU). The results of all attenuation measurements are summarized in Fig. 3.23. All samples of oil tested were drawn from the MiniBooNE detector. The extinction rate (inverse of attenuation length) is plotted for a range of wavelengths. The JHU measurement, shown by the solid blue line, were performed with a spectrophotometer and 1 cm cell and compared to transmission of the light through water (corrected for reflections). Similar measurements were made with comparison to cyclohexane instead of water, indicated by the solid red line. For these measurements, absorption in the cyclohexane is the cause of the disagreement at wavelengths below 270 nm. The FNAL group also used a spectrophotometer, but the measurements were made for various path lengths of oil and compared to air, shown by the black lines (dotted, dashed, dot-dash, and solid). As with the JHU measurements, corrections for reflection were applied, and additional corrections for focusing effects in the instrument were applied. The wavelength-dependent 1.6 m tester result is normalized to the absolute measurement made at 460 nm; both of these are shown in maroon. The Princeton scattering measurements, discussed earlier, are shown in pink for the isotropic and anisotropic components of the scattering rate. Also shown in pink is the predicted rate of isotropic Rayleigh scattering. The measured emission and excitation fluorescence spectra, also discussed earlier, were analyzed using Singular Valued Decomposition (SVD) to extract the dominant spectral components. The sum of the fluorescence rates for this analysis is shown in gold. The spectra of four fluors found in these measurements are shown by the purple, solid maroon, turquoise, and green lines. The spectrum of fluor 3 agrees well with the separately studied spectrum of Vitamin E.

Extinction Rate for MiniBooNE Marcol 7 Mineral Oil
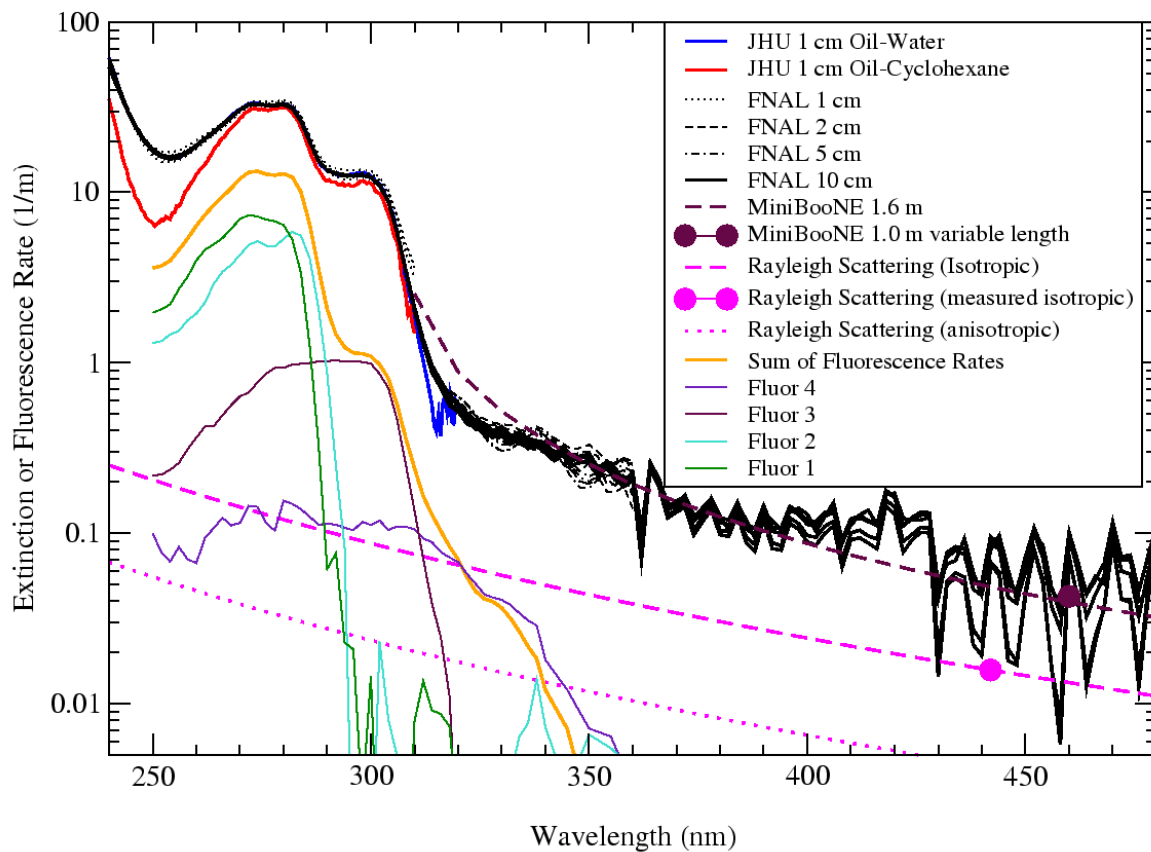
Figure 3.23: Results from all attenuation measurements made for the Marcol 7 mineral oil [94]. A description of each of the measurements may be found in the text.

Chapter 4

Simulation

There are several Monte Carlo programs used in the simulation of MiniBooNE processes. The first is called `BooNEG4Beam` which models particle production in proton-beryllium collisions in the MiniBooNE target, secondary particle propagation, and decay to neutrinos. The neutrino fluxes predicted by `BooNEG4Beam` are input to `Nuance` [95], which simulates the neutrino cross sections and generates events. The interactions modeled by `Nuance` are fed into the detector Monte Carlo simulation, called `BooDetMC`. Finally, the output of `BooDetMC` passes to a simulation of the data acquisition electronics, `MCthroughDAQ`, where the Monte Carlo events are output in a form that is identical to MiniBooNE detector data.

4.1   Beam Monte Carlo

Neutrino flux predictions for all neutrinos relevant to MiniBooNE (ν_μ, $\bar{\nu}_\mu$, ν_e, $\bar{\nu}_e$) are made with two simulation programs. `BooNEG4Beam` is a GEANT4-based Monte Carlo simulation [96] that models the geometry and materials in the MiniBooNE target hall and decay region, as well as the physics processes that govern interactions of the particles involved in neutrino production. The package generates events with the proper beam characteristics and simulates the passage of particles through all materials present in the target hall and decay region. The output of the GEANT4 simulation is fed into another Monte Carlo program that generates kinematic distributions for the neutrinos from pion, kaon, and muon decays. This program also makes the predictions for the final neutrino

fluxes at the MiniBooNE detector, as was shown in Fig. 3.6. A more detailed discussion of the MiniBooNE neutrino flux predictions may be found in Ref. [72].

4.2   Cross Section Monte Carlo and Event Generator

The simulation of all neutrino interactions relevant for MiniBooNE is performed by the `Nuance` neutrino cross section Monte Carlo and event generator [95]. It was originally developed to simulate atmospheric neutrino interactions in the IMB detector, but was adapted for Super-K and K2K. It is currently in use by a number of neutrino experiments in addition to MiniBooNE and those mentioned above, including KamLAND, MINOS, SNO, and several future experiments (*e.g.*, FINeSSE [97], MINERνA [98], NOνA [99], T2K [100], and UNO [101]).

`Nuance` is a FORTRAN-based Monte Carlo program that takes as input the detector configuration and the predicted fluxes (ν_μ, $\bar{\nu}_\mu$, ν_e, $\bar{\nu}_e$) from `BooNEG4Beam`. The program works in two stages:

1. For a given detector configuration and selected processes, the program produces a "rates" file. This occurs at the beginning and is saved to a file, since it involves nasty integrations that should only need to be performed once per detector configuration / input flux.

2. The second step is optional. If enabled, the code will generate events for input to the Mini-BooNE detector Monte Carlo.

`Nuance` models 99 distinct interactions, both neutral current and charged current, in the energy range $10^{-1} < E_\nu < 10^3$ GeV. Individual or multiple processes may be selected for a given set of generated events. The processes are shown in Table D.1.

The relevant physics models that are implemented by `Nuance` are

- the Llewellyn-Smith expression for the quasi-elastic cross section on free nucleons [102];

- the Rein and Sehgal resonance cross sections [31];

- the Bodek-Yang [103] deep inelastic scattering (DIS) cross section at large invariant mass, W, and momentum transfers, Q^2; and

- the Smith-Moniz relativistic Fermi gas model for quasi-elastic scattering from nucleons bound inside a nucleus [104].

Only a subset of the interaction types will be (briefly) discussed here, with concentration on those which comprise the signal or background populations for this analysis. A full description of these and other interactions modeled in `Nuance` can be found in Ref. [95], and references therein.

Quasi-elastic scattering

Charged current quasi-elastic interactions comprise nearly 40% of the events observed in the Mini-BooNE detector. Since mineral oil is the target in MiniBooNE (approximated as CH_2), all of the neutrinos in CCQE interactions will scatter from a nucleon bound in carbon. The form factors used to describe this process are parameterized in terms of the vector mass (m_V) and the axial mass (m_A). The `Nuance v3.000`[1] values for these parameters are $m_V = 0.84$ GeV and $m_A = 1.03$ GeV. The vector mass has been measured with great accuracy in electron scattering experiments, but the axial mass is much less well known. The main source of theoretical error in the quasi-elastic cross section is the uncertainty in the value of m_A, which can only be extracted from neutrino scattering data.

There are a number of nuclear effects that can change the quasi-elastic cross section. `Nuance` includes the combined effects of Fermi motion of the target nucleon, Pauli blocking, and nuclear binding. The result is a suppression of the quasi-elastic cross section; the suppression decreases with increasing neutrino energy.

In the NC π^0 analysis, CCQE events make up $\sim 10\%$ of the background, as will be shown in Section 5.3.

Single pion production

The simulation of single pion production is based on Rein and Sehgal's model (discussed in Sec. 2.1), where the dominant production is mediated by a baryon resonance. `Nuance` generates single pions via both resonant and non-resonant channels. For neutrino energies near 1 GeV, single pion

---

[1]This is the version that MiniBooNE used at the time of this writing.

production is dominated by the $\Delta(1232)$ resonance; however, the `Nuance` model includes all known resonances[2] in the invariant mass region $W < 2$ GeV. One difference between the original Rein and Sehgal paper and the `Nuance` implementation is that the `Nuance` model has been further updated to include improved knowledge of the baryon masses and additional non-strange resonances up to 2 GeV [95]. The form factors used to describe resonance production are assumed to be identical to those used for quasi-elastic scattering (see Ref. [102]), except that the pseudoscalar form factor of the nucleon is neglected for these events. The value of the axial mass that is used in `Nuance` for resonant pion production is $m_A = 1.1$ GeV. Additionally, there are two extra reactions included that reduce the number of pions produced in the final state. "Pion-less Δ decay" ($\Delta N \rightarrow NN$ and $N^*N \rightarrow NN$) can reduce the number of pions by anywhere from 10 to 50%. The decay rate is not well-measured, and therefore this is not included in the program as a distinct process. It appears as an *ad hoc* suppression (20% for $I_3 = \pm\frac{1}{2}$ reactions, and 10% for $I_3 = \pm\frac{3}{2}$ reactions). The second reaction is a radiative Δ decay ($\Delta \rightarrow N\gamma$), which has a 0.5% branching ratio and may be an important irreducible background for the MiniBooNE ν_e oscillation search.

For simulation of coherently produced pions, `Nuance` implements the Rein and Sehgal coherent production model [36] for the cross section and event kinematics. This model was discussed in Section 2.2. The value of the axial mass that is used in `Nuance` for coherent pion production is $m_A = 1.03$ GeV.

A related, but not identical, reaction included in the `Nuance` coherent pion production channels is diffractive pion production. Here, instead of interacting with the entire nucleus, the neutrino interacts with a free nucleon; however, the dynamics of coherent and diffractive pion production are the same. A discussion of this process may be found in Ref. [33]. It contributes only a very small amount to the overall cross section for single pion production.

Multiple pion production

Interactions in which multiple pions are produced in the final state are simulated in `Nuance` using a combination of resonant and DIS production mechanisms. Resonant states are treated by the

---

[2]A total of 18 higher mass resonances are included in addition to the prominent $\Delta(1232)$ resonance. Interference between resonances with identical isospin is taken into account [95].

Rein and Sehgal model up to ~ 2 GeV. Deep inelastic scattering events follow the Bodek-Yang prescription. All of the included reactions are shown in Table D.1. Multiple pion events contribute only $\sim 5\%$ to the background in the NC single π^0 analysis.

Final state interactions

Particles produced in neutrino interactions with CH_2 have the chance to re-interact before exiting the nucleus. The catch-all phrase "final state interactions" (FSI) is used here to describe interactions that might transform the topology of an event.

Nuance simulates FSI by tracking hadrons through the nucleus in steps of 0.2 fm, calculating an interaction probability at each step. The probability for interaction is based on measured $\pi - N$ and $N - N$ cross sections and angular distributions, shown in Fig. 4.1. As a result, particles (and their interaction products) may interact several times before exiting the nucleus. The final state interactions modeled by Nuance that may affect pion production include:

- absorption – a pion disappears inside the nucleus,

- charge exchange – $\pi^+ n \rightarrow \pi^0 p$, $\pi^0 p \rightarrow \pi^+ n$, $\pi^0 n \rightarrow \pi^- p$, $\pi^- p \rightarrow \pi^0 n$,

- elastic and inelastic (re)scattering – a pion maintains its identity, but is deflected,

- recoiling nucleon scattering – a nucleon may rescatter and produce pions in the final state, or rescatter several times until it reaches the surface of the nucleus, producing multiple nucleons in the final state, and

- nuclear de-excitation – the nucleus is excited to a higher energy level; it decays electromagnetically to its ground state via the emission of a few-MeV γ. (This process, although included, has little to no effect on the NC π^0 analysis because the energy of the γ is so low.)

4.3   Detector Monte Carlo

The simulation of the MiniBooNE detector response to particles traversing the materials it contains is handled by BooDetMC, a GEANT3-based program [69]. It takes the events generated by Nuance
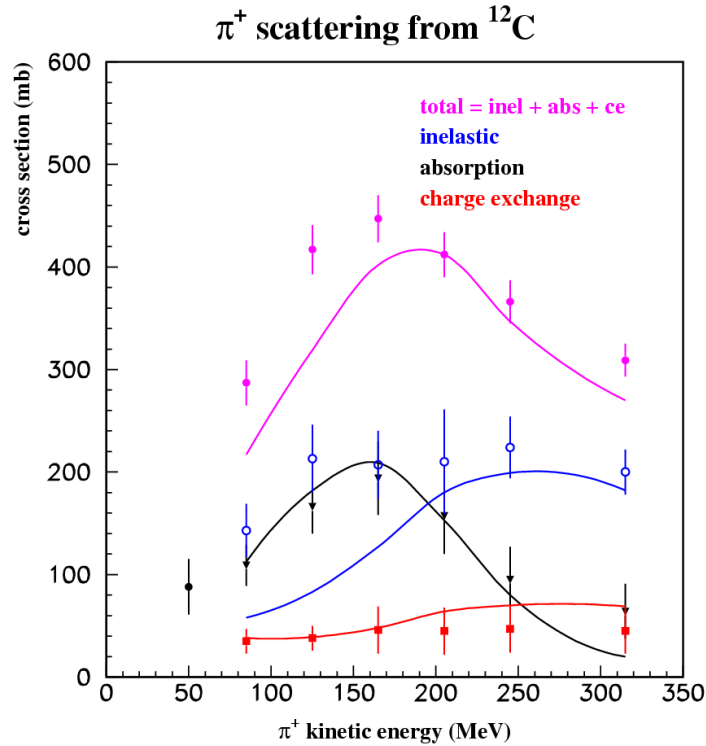
Figure 4.1: Cross sections for $\pi - N$ scattering experiments that measured π^+ absorption, π^+ inelastic and elastic scattering, and π^+ charge exchange. The solid lines are Nuance parameterizations of these cross sections. Dots are experimental data.

and assigns a density-weighted interaction vertex (no interactions occur in the vacuum inside each PMT, and more interactions per unit volume occur in the steel of the detector wall than in the mineral oil). Once the vertex location is decided, the simulation takes the final state particles generated by `Nuance` and steps them through the detector, accounting for geometrical volume boudaries, diffuse and specular reflection of detector materials, PMT quantum efficiency, and the properties of the particle being tracked (dE/dx, δ-ray production, Bremsstrahlung, multiple scattering, hadronic interactions, etc.) [105]. Hadronic interactions are treated with the GFLUKA hadronic interaction model, rather than the GEANT default model (GHEISHA).

The oil optical model parameters are defined on the basis of results from benchtop measurements of various properties. Of particular note are:

- Reflection coefficients for white and black surfaces

- PMT quantum efficiency parameters: from Hamamatsu, corrected for air-glass reflection

- PMT relative efficiency as a function of angle relative to the PMT axis

- Oil refractive index and group velocity parameters

- Oil attenuation length from $250 - 650$ nm in steps of 5 nm

- Polarization-dependent Rayleigh scattering

- Isotropic Raman scattering with λ^4 scattering length model

- Scale rates and lifetimes of individual fluorophores

- Fluorescence excitation and emission spectra from $250 - 650$ nm in steps of 5 nm

- Scintillation emission rates for individual fluorophores.

The number of Čerenkov and scintillation photons and their hit times are recorded for each final state particle. These quantities are used in the reconstruction algorithms. In addition, the "truth" information for each final state particle is retained (4-momentum, vertex, creation time, interacting neutrino type) for cross checks and systematic studies.

The final step of the detector simulation does not take place in `BooDetMC`, since it involves simulation of the data acquisition electronics (discussed in Section 3.4) instead of the detector itself. The output from `BooDetMC` gives the photon arrival times at the face of the PMTs. The final step, a FORTRAN program called `MCthroughDAQ`, smears hit times and charges to determine these quantities at the PMT anode. The smearing functions were derived from *ex situ* measurements made with a MiniBooNE PMT. For each PMT, the program simulates the integration of charge by the DAQ electronics and fires a simulated discriminator if the charge threshold is crossed. Finally, `MCthroughDAQ` outputs simulated "quads," just like true detector data, so that both data and Monte Carlo may be treated in exactly the same way in reconstruction algorithms.

4.4 Strobe Overlay

None of the programs described above simulates PMT dark noise or cosmic rays coincident with the beam. These are introduced to the Monte Carlo via a program called `CombineEvents`. It

combines information from MiniBooNE detector strobe triggers (see Section 3.4.1) with Monte Carlo events. The output is typically called "<Monte Carlo sample>+strobe." By this method, the program properly combines dark noise or cosmic rays occurring during the beam window *if a neutrino interaction occurred* (which is 100% of the time in Monte Carlo). It does not simulate events in which no neutrino interaction occurred, but a cosmic ray interacted or PMT dark noise caused activity during the beam window. This turns out to be a reasonable approximation, since only a very small fraction of events of this type will pass the event selection cuts. This will be discussed further in Section 5.1.

The Monte Carlo samples used for this analysis are called "cocktail+strobe," indicating the presence of a strobe overlay on a "cocktail" sample of neutrino interactions (ν_μ, $\bar{\nu}_\mu$, ν_e, $\bar{\nu}_e$ in the quantities suggested by the beam MC flux prediction).

Chapter 5

Data Reduction and Event Selection

This chapter describes the selection and reconstruction of neutral current π^0 events. Since these events are a small fraction of the overall number of neutrino events collected, and there are only a few measurable variables in the relevant events, it is important to select and reconstruct them correctly.

5.1 Event Preselection

5.1.1 Trigger and Latency Criteria

Event selection begins with a sample of all events with a "beam" type trigger, as discussed in Section 3.4.1. The data for the full 19.2 μs surrounding the beam spill are saved for each beam trigger. The latency filter mentioned in Section 3.4 is applied to these triggers. This ensures that the requested TSAs from the circular buffers have not been overwritten or corrupted, which only happens for a very small fraction of beam events ($< 1/10000$) [106].

5.1.2 Subevent and Multiplicity Criteria

Events which pass the trigger and latency criteria are passed to a low-level algorithm that breaks each event into more easily reconstructible "subevents."

The SplitEvent algorithm [107] divides tank events into clusters of PMT hits where consecutive hits are separated by no more than a specified minimum time gap. Any cluster having more than 10 PMT hits (including both tank and veto hits) is defined as a subevent. The minimum timing gap between consecutive subevents is 10 ns, which was chosen as the optimal separation based on data and Monte Carlo studies. Therefore, by definition, there are no more than 10 ns between consecutive hits in any given subevent. The algorithm is important for separating events into clusters that can be properly handled by the reconstruction algorithms. It is additionally useful in identifying activity other than the primary beam interaction that occurred during the beam spill. For example, if a muon is produced during the interaction, the electron from its decay may be identified as a second cluster of hits occurring later in time – a second subevent. The algorithm is also particularly useful for rejecting events that are not neutral current π^0 production; since π^0's decay promptly ($\sim 10^{-17}$ seconds), no second subevent is expected. A requirement of one and only one subevent is applied to events passing the trigger and latency criteria.

Having selected events with exactly one subevent, a further requirement on tank and veto multiplicity suppresses events associated with cosmic ray activity. Cosmic rays coincident with the beam spill are eliminated by requiring fewer than 6 hits in the veto region ($N_{veto} < 6$). A further requirement of greater than 200 hits in the main tank region ($N_{tank} > 200$) eliminates most events in which a cosmic muon entered the detector before the beam window, stopped, and decayed, leaving an electron. The veto multiplicity requirement also ensures that the event is fully contained, *i.e.*, that no charged particles from the neutrino interaction produce light in the veto region.

The effect of these selection requirements on simulated neutrino events is shown in Table 5.1. The event sample is comprised of more than 3 million inclusive events generated by the Nuance neutrino event generator [95]. These events were propagated through the detector Monte Carlo simulation and reconstructed with the Analysis Framework. The table displays the efficiency of consecutive cuts on "signal" and "background" events. Signal events are defined as resonant and coherent neutral current single π^0 production. Background events are charged current quasi-elastic (CCQE), neutral current elastic (NCE), charged current resonant (CC Res), neutral current resonant single charged pion production (NC Res), and all other interaction types (Other). The single subevent requirement is quite efficient on the signal events, leaving approximately 75%. A large fraction of the CC events are eliminated by this cut. Charged current events typically have a stop-

ping muon which decays; the resulting Michel electron often causes a second subevent to appear in these events. Adding a tank multiplicity requirement eliminates many of the NC elastic events, since these typically consist of a single recoiling nucleon that doesn't produce much Čerenkov light in the detector. The NC resonant charged pion events are more difficult to eliminate with the simple preselection requirements discussed here, but these events will be further reduced with later requirements. All in all, the precuts perform reasonably well in eliminating large fractions of the background events, while leaving a comparably large fraction of the signal.

Selection	NC Single π^0		Background				
	NC Res	NC Coh	CCQE	NCE	CC Res	NC Res	Other
No cuts	1	1	1	1	1	1	1
1 subevent	0.747	0.769	0.297	0.651	0.133	0.521	0.206
$N_{veto} < 6$	0.659	0.664	0.102	0.625	0.052	0.485	0.092
$N_{tank} > 200$	0.462	0.577	0.091	0.022	0.049	0.222	0.085

Table 5.1: Fraction of the original number of each type of Monte Carlo event surviving consecutive preselection requirements, organized by interaction type. Each consecutive selection cut includes all of the previous cuts. The sample consists of 3.2 million inclusive Nuance events generated in a 500 cm radius.

The effect of the preselection cuts on beam data, with the exception of the subevent requirement, is demonstrated in Fig. 5.1. Each of the three panels shows the average time of tank PMT hits in the *first* subevent recorded in the MiniBooNE detector (the single subevent criterion is not applied here). The top panel is the average tank time before any cuts have been applied; the beam spill peaks clearly above the background during the expected beam arrival window ($4.6 - 6.2 \ \mu$s). The distribution beneath the beam spill is due to subevents created by background processes. The center panel shows the effect of requiring less than 6 hits in the veto region, removing many of the background events arising from cosmic rays which arrive coincident with the beam spill. The bottom panel demonstrates the final reduction of non-beam backgrounds from events coincident with the beam spill. A large fraction of the events eliminated by this cut are due to neutral current elastic scattering, where very little Čerenkov light is produced. Many of the other events are

from muons that entered the tank before the trigger window, but decayed during the beam spill to produce coincident electrons.

The simple subevent and multiplicity precuts greatly reduce the non-beam-induced events; the ratio of beam:non-beam events after these cuts greater than 1000:1. To cross-check the non-beam-related background rejection, the same selection cuts are applied to strobe events ("beam" events without beam), shown in Fig. 5.2. These events should be identical to beam events, apart from the lack of beam delivery. With the applied tank and veto multiplicity criteria, the rejection factor for strobe events is $(2.44 \pm 0.12) \times 10^{-4}$.

5.2   Event Reconstruction

A chain of reconstruction algorithms are applied to events which pass the event preselection process detailed above, providing a number of levels of reconstruction for each event. The three stages of reconstruction are:

- **StancuFastFit**– The first stage of event reconstruction; a fast single-ring fitter which provides a rough estimate of the event time and vertex based on a timing likelihood.

- **StancuFullFit**– The second stage of event reconstruction; a refined single-ring fitter. The result of the StancuFastFit algorithm is used as input, and the event timing and vertex are more precisely determined using a time and charge likelihood.

- **StancuPi0Fit**– The third stage of event reconstruction for this analysis; a two-ring fitter. The time and vertex information determined by the StancuFullFit algorithm is used as the starting point for this algorithm. Each event is fit under the assumption of two γ rings from the decay of a π^0.

All of these algorithms were written by Ion Stancu; a detailed description of each algorithm may be found in the technical notes listed in Ref. [108]. Only a brief description will be given here.
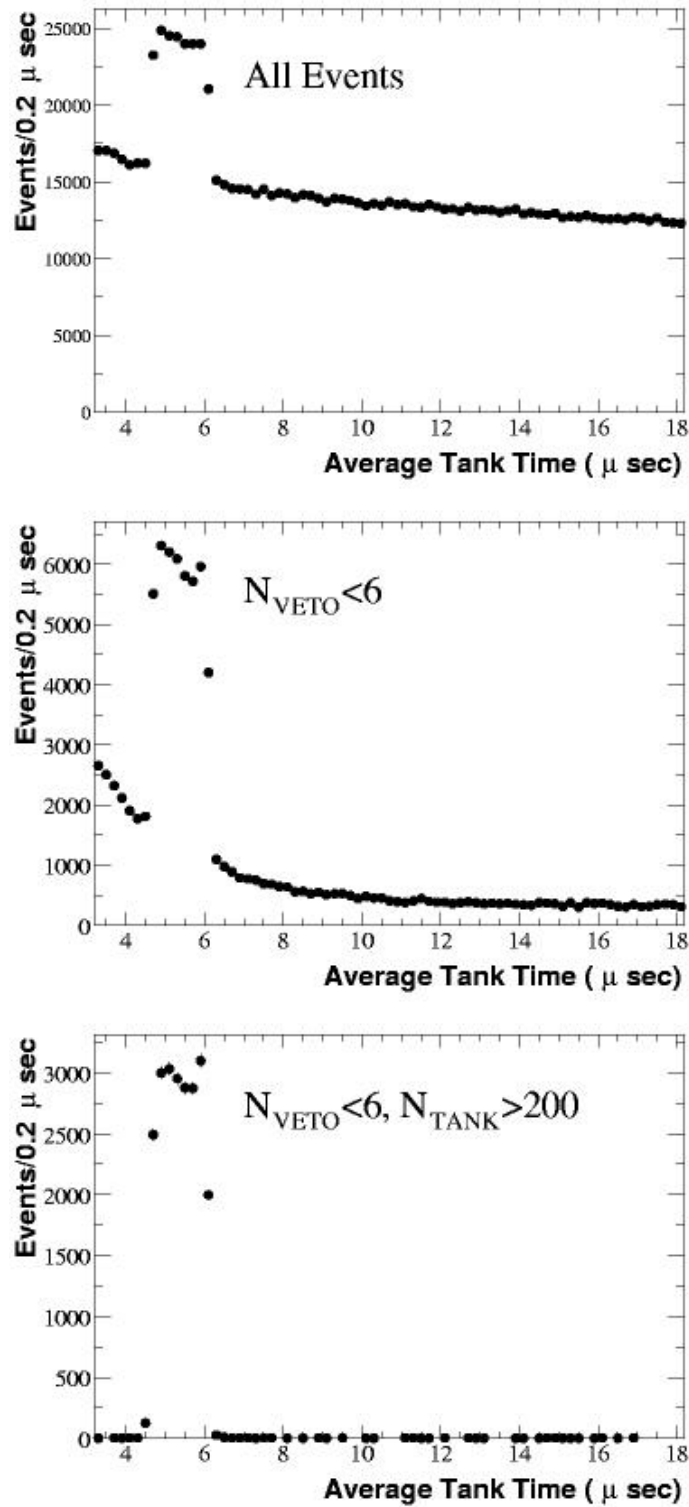
Figure 5.1: Timing distribution of events in beam trigger window with no cuts (top), $N_{veto} < 6$ (center), and $N_{veto} < 6$, $N_{tank} > 200$ (bottom).
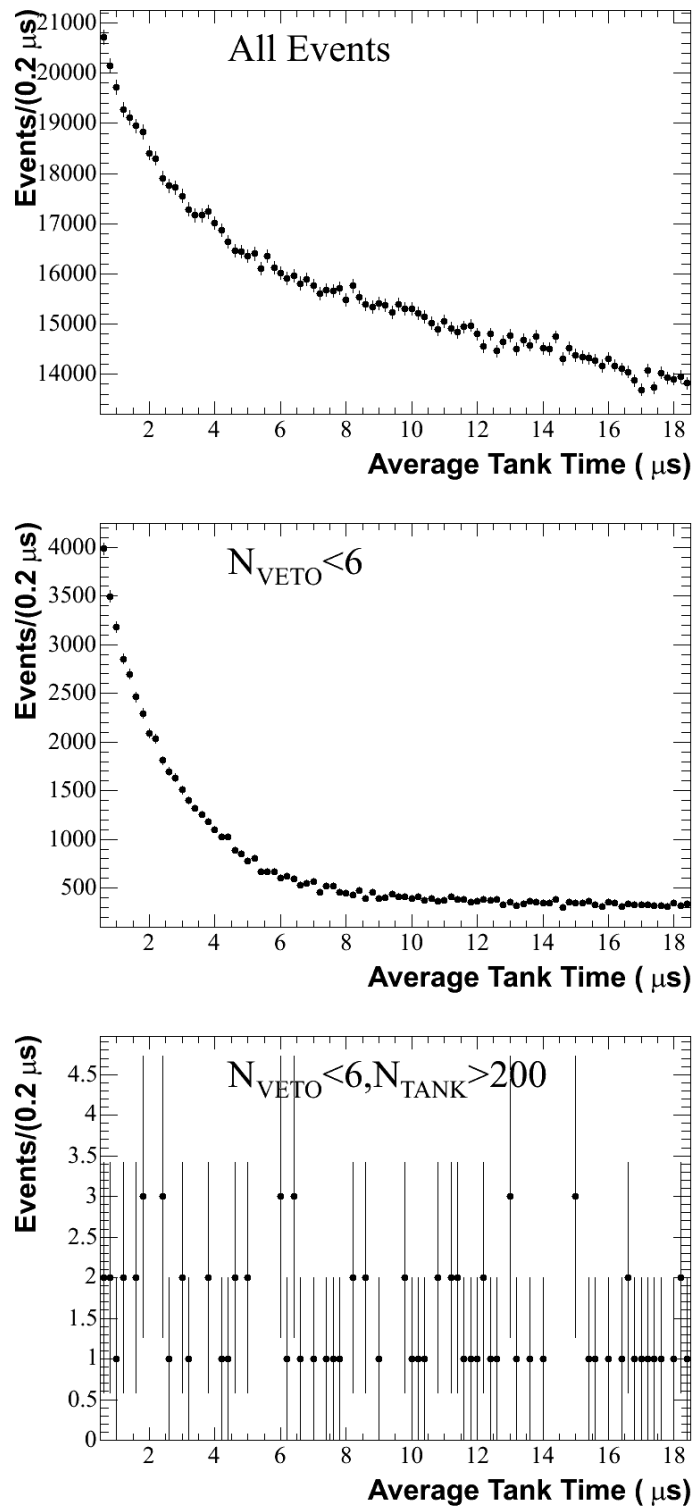
Figure 5.2: Timing distribution of events in strobe triggers with no cuts (top), $N_{veto} < 6$ (center), and $N_{veto} < 6$, $N_{tank} > 200$ (bottom).

5.2.1 StancuFastFit

The Stancu fast fitter is a time likelihood fit which uses only the timing and location of hit PMTs to roughly determine an event's 4-vertex and direction. During this stage of the fitting, events are assumed to be electron-like. In electron-like events, it is a good approximation to assume that the light in the event comes from a single point, since the tracks are typically short and most of the light is prompt Čerenkov light. While a basic χ^2 minimization can do well in determining the event 4-vertex in this case, the fast fitting algorithm uses a slightly more sophisticated method that is less susceptible to bias – maximization of a timing log likelihood. The probability to measure a set of hit times $(t_i)_{i=i,N}$ at N PMTs, given an event vertex $\alpha \equiv (x_0, y_0, z_0, t_0)$, is given by the product

$$p((t_i); \alpha) = \prod_{i=1}^{N} p(t_i; \alpha) = \left(\frac{1}{\sqrt{2\pi}\sigma} \right)^N \prod_{i=1}^{N} \exp\left(-\frac{t_{corr,i}^2}{2\sigma^2} \right). \tag{5.1}$$

where $t_{corr,i} = t_i - t_0 - r_i/c_n$. Turning this around, we search instead for the most likely event 4-vertex given a measured set of times at N PMTs with locations $(\vec{r}_i)_{i=1,N}$. This is achieved by maximizing the above probability with respect to α. Equivalently, one can minimize the negative log of the likelihood function:

$$-\ln \mathrm{P}((t_i); \alpha) = N \ln(\sqrt{2\pi}\sigma) + \frac{1}{2\sigma^2} \sum_{i=1}^{N} (t_i - t_0 - \frac{r_i}{c_n})^2 \tag{5.2}$$

which is fully equivalent to a non-weighted χ^2 minimization, since N is constant in a given event. In the above equation, the distance from the ith hit PMT to the current best estimate of the vertex vector position, $\vec{r}_0 = (x_0, y_0, z_0)$, is given by $r_i = \sqrt{(x_i - x_0)^2 + (y_i - y_0)^2 + (z_i - z_0)^2}$, and c_n is the speed of light in a medium with refractive index, n. No information from the Čerenkov rings is used at this stage; the Čerenkov and scintillation light in the event are assumed to have the same timing offset, t_0, and width, σ. The starting vertex position is taken to be the charge-averaged position of all the hit PMTs, and the starting time is chosen to agree with this position and the times and positions of hit PMTs. Minimization is performed with MINUIT [109]. After its completion, a "corrected" time is calculated for each hit PMT using the vertex from the minimization and correcting for time of flight. Hits with a corrected time of less than ~ 4 ns are considered "prompt," and contain mostly Čerenkov light with only a small contamination from scintillation light. A track direction is estimated by taking a charge-weighted average of the prompt hit direction cosines with respect to the minimized vertex. An approximate energy of the particle is then determined using

the total charge in the main region of the detector and the distance of the minimized vertex from
the optical barrier. The final step estimates the strength of Čerenkov and scintillation light in the
event by dividing the total energy of the particle by two proportionality constants that have been
previously determined using a sample of Michel electrons from cosmic muon data.

5.2.2   StancuFullFit

The Stancu full fit algorithm uses the 4-vertex, direction, and energy determined in the fast fit
as its starting values. Here, a more refined negative log likelihood is minimized. In addition to a
timing likelihood similar to that used in the fast fitter, there is also a charge likelihood. While the
fast fitting algorithm described above ignores the fact that we cannot literally count the number of
photoelectrons (PEs) in an event, the full fitting algorithm addresses this issue. The StancuFullFit
algorithm calculates the predicted charge, μ_i, at each PMT and uses a modified timing likelihood
that takes the charge-dependence of the PMTs into account.

Assuming the event is an electron, the current estimate of the position and direction are used
to calculated the expected charge in each PMT. The predicted charge is given by

$$\mu_i = \frac{\epsilon_i}{r_i^2} \left[\Phi e^{-\frac{r_i}{\lambda_S}} f_S(\cos \eta_i) + \rho F(\cos \theta_i, E) e^{-\frac{r_i}{\lambda_C}} f_C(\cos \eta_i) \right], \tag{5.3}$$

where ϵ_i is the quantum efficiency of the ith PMT, r_i is the distance to the ith PMT, Φ (ρ) is the
scintillation (Čerenkov) light strength, $\lambda_{S(C)}$ is the attenuation length for scintillation (Čerenkov)
light, $f_{S(C)}(\cos \eta_i)$ is the PMT response to scintillation (Čerenkov) light as a function of incidence
angle η_i, and $F(\cos \theta_i, E)$ is the angular distribution of Čerenkov light. This assumes that both the
scintillation and Čerenkov light come from the same effective vertex, which is a good approximation
in the case of relatively low amounts of scintillation light, as in MiniBooNE.

The charge likelihood, $P(q_i; \mu_i)$, is read from one of two look-up tables, for old (R1408) PMTs
and new (R5912) PMTs. As mentioned above, the timing likelihood takes into account the charge-
dependence of the PMTs. It has the form

$$P(t_i; (x_0, y_0, z_0, t_0), \mu_i^C, \mu_i^S) = \frac{\mu_i^C}{\mu_i^C + \mu_i^S} P_C(t_i; \mu_i^C) + \frac{\mu_i^S}{\mu_i^C + \mu_i^S} P_S(t_i; \mu_i^S) \tag{5.4}$$

where the Čerenkov probability is

$$\frac{1}{\sqrt{2\pi}\sigma(E, \mu_i^C)} \exp \frac{-\left[t_i^{corr} - T_0(E, \mu_i^C)\right]^2}{2\sigma^2(E, \mu_i^C)} \tag{5.5}$$

and the corrected time distribution mean (T_0) and width (σ) are both functions of the predicted amount of Čerenkov light and of the energy in the event. The scintillation probability is given by

$$\frac{1}{2\tau} \exp\left[\frac{\sigma^2(E, \mu_i^S)}{2\tau^2(E, \mu_i^S)} - \frac{t_i^{corr} - T_0(E, \mu_i^S)}{\tau(E, \mu_i^S)} \right] \text{Erfc}\left[\frac{\sigma(E, \mu_i^S)}{\sqrt{2}\tau(E, \mu_i^S)} - \frac{t_i^{corr} - T_0(E, \mu_i^S)}{\sigma(E, \mu_i^S)} \right], \quad (5.6)$$

which is a Gaussian with mean T_0 and width σ folded with an exponential exp(-t/τ), where τ is the time constant for scintillation light. Similar to the Čerenkov probability, these parameters also depend on the event energy and the amount of predicted scintillation light, μ_i^S.

This distribution is used as the likelihood function for the actual distribution of charge in the event. The full likelihood, which is the product of the time and charge likelihoods, is maximized for vertex position, time, and direction. In the first step, the Čerenkov and scintillation strengths (ρ, Φ) are held fixed while the energy determined in the fast fit is used to generate corrected time and angular charge distributions for the event. This first minimization determines a new 4-vertex and event direction. As in the fast fit, the event energy is inferred from the vertex position and distance from the optical barrier. Iterations are performed where event energies are recalculated based on the newly determined positions. The corrected time distribution and angular charge distribution is regenerated, and a second minimization is performed with respect to the Čerenkov and scintillation strengths, holding the 4-vertex and position fixed.

5.2.3 StancuPi0Fit

The Stancu π^0 fitter uses the vertex found by the full fit as its starting point. It assumes the event is a neutral current π^0 that has decayed to two γ's. In this case, it is not a good assumption to use a point-like light source as in the fast and full fits because each γ will travel some distance in the oil before converting to an electron-positron pair that produces Čerenkov light.

The model used for the neutral pion reconstruction is characterized by 14 variables:

- π^0 creation 4-vertex (x_0, y_0, z_0, t_0)

- Mean emission points of γ's from the π^0 vertex along γ directions (s_1, s_2)

- γ directions $(\phi_1, \theta_1, \phi_2, \theta_2)$

- γ Čerenkov light strengths (ρ_1, ρ_2)

- γ scintillation light strengths (Φ_1, Φ_2)

As it would take too much computing power and time to minimize all 14 variables at once for each event (and the minimization would be extremely sensitive to the chosen starting parameters), the minimization is performed in several steps. At each stage a few variables are minimized while the others remain fixed.

Assuming the FullFit result gives a direction that corresponds fairly closely to the direction of the ring from the most energetic gamma in the π^0 decay, the first step is to determine a good starting point for the ring from the second gamma. Since the vertex returned by the FullFit is typically shifted along the direction of the particle trajectory (and even more so if the particle is a gamma rather than the electron assumed by the FullFit), a parameterization of shift as a function of energy is used to extrapolate the vertex back along the γ direction to the π^0 vertex. The same shift value (where the gamma converts to a charged particle pair) is assumed for the second gamma in this step. An initial guess for the direction and energy of the second ring is found by searching for the area of strongest Čerenkov light in 110 equally-spaced solid angles relative to the direction of the first ring. The Čerenkov light strength is calculated by summing the total charge within the annulus $0.45 < \cos\theta < 0.85$ for each ring's direction. In the jth direction, this is given by

$$\rho_2^{(j)} = \frac{Q_{tot}^{(j)} - \rho_1\Omega_1}{\Omega_2^{(j)}} \tag{5.7}$$

where $Q_{tot}^{(j)}$ is the total recorded charge in the two Čerenkov regions, ρ_1 is the Čerenkov light strength of the first ring, Ω_1 is the total solid angle in the Čerenkov region of the first ring, and $\Omega_2^{(j)}$ is the total solid angle in the Čerenkov region of the jth direction. This effectively subtracts the expected light contribution from the first gamma. The direction with the highest Čerenkov light density is taken as the starting direction of the ring from the second gamma. The calculated Čerenkov strengths are then used to infer the energies of the two gammas.

The first minimization is a function of 11 variables:

- γ_1 mean emission 4-vertex (x_1, y_1, z_1, t_1): initial value taken as the reconstructed electron vertex from the FullFit

- γ_1 direction (ϕ_1, θ_1): initial value taken as the reconstructed electron direction from the FullFit

- Shift from γ_1 mean emission point back to π^0 creation vertex (s_1): initial value given by a parameterization $s(E_1)$

- γ_2 direction (ϕ_2, θ_2): initial value taken as the direction of the maximum $\rho_2^{(j)}$

- Shift from π^0 creation vertex to γ_2 mean emission point (s_2): initial value given by same parameterization $s(E_2)$ along direction of γ_2

- Fraction of Čerenkov light in first ring $(f_1 = \frac{\rho_1}{\rho_1 + \rho_2})$

The ratio of scintillation to Čerenkov light is fixed during this minimization. The total light strength in the event is also held fixed; it is set to be the ratio of total prompt charge to total solid angle, where prompt charge is defined as the first 85% of hits in the event. This results in a reduction from 14 to 11 variables, for a slow but manageable minimization.

The results of this minimization are used as initial values for the second minimization, which is only a function of 5 variables. As in the previous step, the ratio of scintillation to Čerenkov light is fixed and only prompt hits are used. In addition, the π^0 creation vertex and the direction and shift of the first (most energetic) gamma are fixed. This leaves 5 free variables:

- γ_2 direction (ϕ_2, θ_2)

- γ_2 shift (s_2)

- Čerenkov light strengths of the two gammas (ρ_1, ρ_2)

After the minimization is complete, the timing distributions and angular light distributions are re-calculated using the newly determined energies (which are proportional to the Čerenkov strengths).

The output of the second minimization is used as the starting point for the third step. The purpose of this step is only to determine the optimal values of the scintillation and Čerenkov strengths in each ring, meaning there are 4 free variables in the minimization. Unlike the first two steps, this iteration uses *all* of the hits in the event instead of only the prompt hits.

This fitter may be considered somewhat simplistic in that it forces each event to have two Čerenkov rings; an event with only 1 ring, such as a charged current quasi-elastic muon event, will be reconstructed with two rings. The advantage of the three-part algorithm, however, is that it allows reconstruction of the π^0 mass from the fitted energies of the gammas and the fitted angle between their reconstructed directions. Using the total 4-momentum of the two gammas from the π^0 decay

$$P_f = P_1 + P_2 = (E_1, \vec{p_1}) + (E_2, \vec{p_2}) = (E_1 + E_2, \vec{p_1} + \vec{p_2}), \tag{5.8}$$

conservation of 4-momentum results in

$$m_{\pi^0}{}^2 = E_1{}^2 + 2E_1 E_2 + E_2{}^2 - p_1{}^2 - 2\vec{p_1} \cdot \vec{p_2} - p_2{}^2 = 2E_1 E_2 (1 - \cos \theta_{12}). \tag{5.9}$$

For non-π^0 events with only one true ring, the algorithm typically reconstructs the event as two rings with a very small opening angle, as shown in Fig. 5.3 for events which pass the preselection criteria. For those CCQE events with $\cos \theta \geq 0.9$, the reconstructed mass is shown in Fig. 5.4. This demonstrates that single ring events passing the preselection are likely to have a reconstructed mass that is lower than the π^0 mass, allowing elimination of many of these events with a simple mass cut.

5.3 Further Event Selection

Due to the restrictions of blindness on potential ν_e oscillation signals, one further requirement is made once the string of reconstruction algorithms is complete. Events with reconstructed π^0 mass < 50 MeV/c^2 are eliminated from the sample because this is where ν_e oscillation events are expected to lie. This is not expected to reduce efficiency for the signal in this analysis.

Any events in the data stream which meet the requirements discussed above and in Section 5.1 are allowed into the "NC Pi0Tuple," which is an ntuple containing only the information that is output by the StancuPi0Fitter. The full set of preselection requirements are

- Event type = "beam"

- Pass latency filter
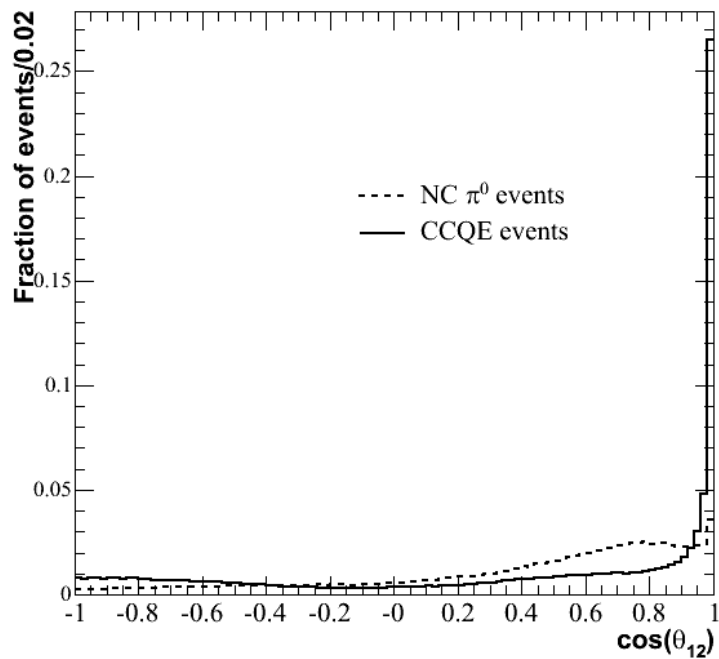
Figure 5.3: Cosine of the opening angle of the two rings found by the StancuPi0Fitter for charged current quasi-elastic events (solid line) and neutral current π^0 events (dashed line).

- Number of subevents = 1

- Number of veto hits in event < 6

- Number of tank hits in event > 200

- Reconstructed π^0 mass > 50 MeV/c^2

The purity of this sample, according to the Monte Carlo simulation, is rather low, with only $\sim 39\%$ NC single π^0 signal events after all preselection requirements. The fractions of the major event types after each preselection requirement is applied are shown in Table 5.2. In the original sample (no cuts), only 7.2% of the events are NC π^0 signal, but after all preselection requirements have been applied to the sample, the fraction of signal rises to 38.6%. The relative efficiency of each cut is shown in Table 5.3. For each entry in this table, the relative efficiency is defined as the number of events passing all criteria up to and including the selection cut for that row divided by the number of events passing all earlier selection cuts, that is,

$$\epsilon_{i^{th}\ row} = \frac{N_{i^{th}\ row}}{N_{(i-1)^{th}\ row}}. \tag{5.10}$$
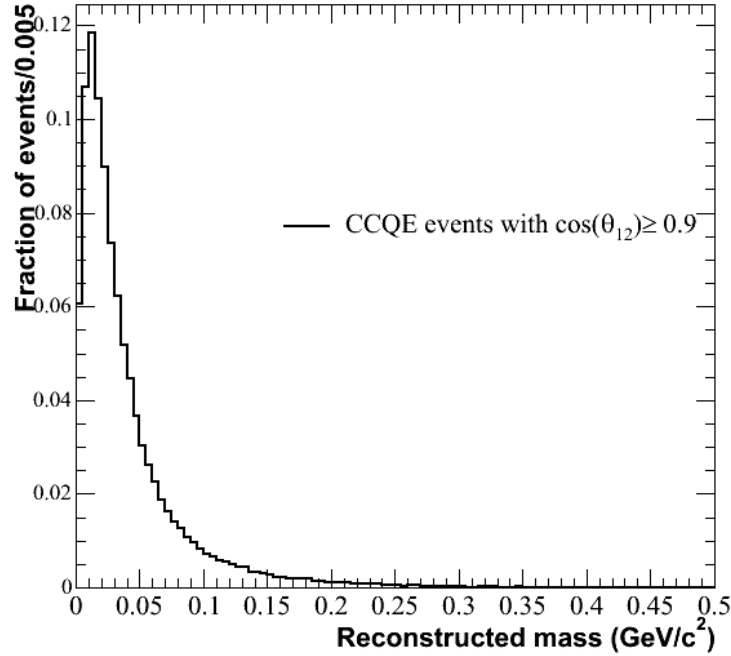
Figure 5.4: Reconstructed mass of the "two-ring" system found by the StancuPi0Fitter for charged current quasi-elastic events whose opening angle is very small.

5.3.1   Analysis Cuts

Events which pass all of the preselection criteria are further required to have reconstructed well. The first step to a good reconstruction is for each of the γ's from the π^0 decay to have a minimum of 40 MeV reconstructed energy. In addition, events are required to have reconstructed vertices within 500 cm of the center of the tank. As shown in Fig. 5.3, many of the background events reconstruct as overlapping (indistinguishable) rings $(\cos\theta_{\gamma\gamma} > 0.9)$. Although a relatively small fraction of events reconstruct with back-to-back gammas $(\cos\theta_{\gamma\gamma} < -0.9)$, background events tend to do so more often than signal events; requiring $\cos\theta_{\gamma\gamma} > -0.9$ has very little effect on the signal, but helps reduce the background in the sample. The final criterion for good reconstruction, based on these opening angle arguments, is the requirement that events have $-0.9 < \cos\theta_{\gamma\gamma} < 0.9$.

The relative efficiencies of each of these analysis-level event selection requirements are shown in Table 5.4. According to the Monte Carlo simulation, $\sim 54\%$ of the events which pass these cuts

Selection	NC Single π^0		Background				
	NC Res	NC Coh	CCQE	NCE	CC Res	NC Res	Other
No cuts	0.056	0.015	0.396	0.163	0.258	0.036	0.077
1 subevent	0.121	0.034	0.340	0.307	0.099	0.054	0.046
$N_{veto} < 6$	0.163	0.044	0.177	0.449	0.059	0.076	0.031
$N_{tank} > 200$	0.255	0.086	0.355	0.035	0.125	0.078	0.065
$m_{\pi^0} > 50\text{MeV/c}^2$	0.303	0.106	0.277	0.027	0.136	0.075	0.077

Table 5.2: Fraction of total sample for Monte Carlo event types after consecutive preselection requirements, organized by interaction type. Each consecutive selection cut includes all of the previous cuts. The sample consists of 3.2 million inclusive Nuance events generated in a 500 cm radius.

are NC single π^0 events (of which 39% are resonant and 15% are coherent). Approximately 13% of the non-NC π^0 events are CC quasi-elastic, 13% are CC $\pi^{\pm}$ production, and the rest are NC elastic, CC π^0, and events in which multiple pions are produced. Table 5.5 shows the fractions of each event type present in the sample after each analysis cut. For each row in the table, the selection cut is applied in addition to all previous selection cuts.

Selection	NC Single π^0		Background				
	NC Res	NC Coh	CCQE	NCE	CC Res	NC Res	Other
No cuts	1	1	1	1	1	1	1
1 subevent	0.747	0.769	0.297	0.651	0.133	0.521	0.206
$N_{veto} < 6$	0.882	0.864	0.342	0.960	0.392	0.930	0.447
$N_{tank} > 200$	0.701	0.868	0.893	0.035	0.946	0.459	0.927
$m_{\pi^0} > 50 \mathrm{MeV/c^2}$	0.855	0.886	0.486	0.510	0.758	0.694	0.875

Table 5.3: Relative efficiencies for consecutive preselection cuts on Monte Carlo events, organized by interaction type. Each consecutive selection cut includes all of the previous cuts. The sample consists of 3.2 million inclusive Nuance events generated in a 500 cm radius.

Selection	NC Single π^0		Background				
	NC Res	NC Coh	CCQE	NCE	CC Res	NC Res	Other
All pre-cuts	0.855	0.886	0.486	0.510	0.758	0.694	0.875
$r_{\pi^0} < 500$ cm	0.946	0.972	0.966	0.938	0.934	0.931	0.900
$E_1 > 40 \&\& E_2 > 40$ MeV	0.886	0.871	0.591	0.816	0.846	0.840	0.943
$-0.9 < \cos\theta_{12} < 0.9$	0.928	0.950	0.644	0.777	0.864	0.916	0.850

Table 5.4: Relative efficiencies of consecutive analysis cuts on Monte Carlo event types, organized by interaction type. Each consecutive selection cut includes all of the previous cuts. The sample consists of 3.2 million inclusive Nuance events generated in a 500 cm radius.

Selection	NC Single π^0		Background				
	NC Res	NC Coh	CCQE	NCE	CC Res	NC Res	Other
Pre-cuts	0.303	0.106	0.277	0.027	0.136	0.075	0.077
$r_{\pi^0} < 500$ cm	0.314	0.115	0.253	0.026	0.135	0.077	0.079
$E_1 > 40 \&\& E_2 > 40$ MeV	0.346	0.125	0.186	0.027	0.143	0.080	0.093
$-0.9 < \cos\theta_{12} < 0.9$	0.373	0.138	0.138	0.029	0.143	0.086	0.092
$m_{\pi^0} \leq 550$ MeV/c^2	0.391	0.145	0.134	0.031	0.133	0.089	0.077

Table 5.5: Event fractions after consecutive analysis cuts on Monte Carlo event types, organized by interaction type. Each consecutive selection cut includes all of the previous cuts. The sample consists of 3.2 million inclusive Nuance events generated in a 500 cm radius.

Chapter 6

Analysis

The analysis of NC π^0 events is performed using statistical fits to extract the number of signal events in the data sample. This is necessary because of the relatively low purity of the final sample (after all cuts). The fitting procedure and its validation will be described in the following sections, followed by a discussion of the cross section measurement method and its validation.

The interesting variables for NC π^0's, used throughout this chapter, are the reconstructed π^0 mass, momentum, angle relative to the neutrino beam, and center of mass (CM) angle (the angle between the direction of the π^0 in the lab frame and the decay axis of the two γ's in the CM frame, represented in Fig. 6.1). All of these variables are reconstructed using StancuPi0Fitter variables that contain information about the direction and amount of Čerenkov light for each γ.
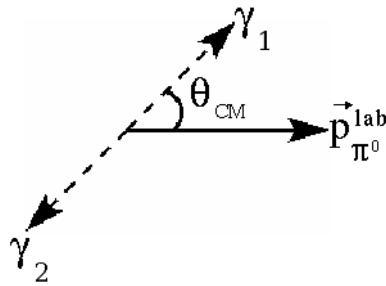
Figure 6.1: Schematic representation of π^0 center of mass angle.

As was shown in Sec. 5.2.3, the mass of an event which successfully passes through the StancuPi0Fitter is reconstructed using the energies of the two γ's and the angle between them:

$$m_{\pi^0} = \sqrt{2E_{\gamma_1}E_{\gamma_2}(1 - \cos\theta_{\gamma_1\gamma_2})} \qquad (6.1)$$

where c has been set to 1 for simplicity here and in the rest of the reconstructed quantities discussed below. Momentum is constructed directly from the directions and energies of the γ's:

$$\vec{p}_{\pi^0} = E_{\gamma_1}\hat{u}_{\gamma_1} + E_{\gamma_2}\hat{u}_{\gamma_2} = \vec{p}_{\gamma_1} + \vec{p}_{\gamma_2}. \tag{6.2}$$

The cosine of the angle of the π^0 relative to the neutrino beam (in coordinates where the neutrino beam is along the z-axis) is merely

$$\cos\theta_{\pi^0} = \frac{p_{z,\gamma_1} + p_{z,\gamma_2}}{|\vec{p}_{\pi^0}|}. \tag{6.3}$$

Finally, the center of mass angle is

$$\cos\theta_{CM} = \frac{1}{\beta}\frac{|E_{\gamma_1} - E_{\gamma_2}|}{E_{\gamma_1} + E_{\gamma_2}} \tag{6.4}$$

where $\beta = |\vec{p}_{\pi^0}|/E_{\pi^0}$.

6.1   Fit Procedure

As shown in Table 5.5, only $\sim 55\%$ of the events in the NC Pi0Tuple are due to NC resonant and coherent single π^0 production. In order to study the distributions of reconstructed signal events, it is necessary to obtain a more pure sample. This is achieved by fitting data distributions to determine what fractions of Monte Carlo-predicted signal and background are present in the data.

Two types of fits will be discussed below. The first is a 1-dimensional fit of the reconstructed mass distribution. The second, more powerful, type is a simultaneous fit of $\cos\theta_{\pi^0}$ *vs.* m_{π^0}. The 1-dimensional fit is used to extract the number of signal events in bins of the variables discussed above. The 2-dimensional fit requires high statistics for the fitting algorithm to converge. It is therefore only used in an inclusive fit to all of the data to extract the relative fractions of resonant and coherent π^0 events for a flux-averaged cross section measurement.

All fitting is performed with the ROOT class `TFractionFitter`[1], which fits Monte Carlo fractions to a data histogram. The fitting routine uses MINUIT to perform an adjusted log-likelihood maximization. It returns the best estimate of the fraction of each Monte Carlo distribution present in the data distribution.

---

[1]This is a direct C++ implementation of the HBOOK routine `HMCMLL`.

The power of the adjusted log-likelihood arises from the fact that the fit takes into account both data and Monte Carlo statistical uncertainties. Other techniques for fitting, such as a simple or weighted χ^2 fit, can be susceptible to bias if the fit sample has low statistics. This problem and its solution are discussed in detail in Ref. [110].

6.1.1 1D Fitting

The 1-dimensional fits are used to extract the fraction of signal (NC resonant and coherent π^0 events) in bins of the reconstructed variable of interest. As an example, we discuss the extraction procedure that is used to determine the distribution of π^0 momentum for signal events.

In both data and Monte Carlo, only events that pass the selection and analysis criteria discussed in Sections 5.3 and 5.3.1 are used in the fits. In the case that we are investigating the π^0 momentum distribution, the first step of the analysis is to bin each of the two samples (data and MC) according to π^0 momentum (from 0.0 to 0.8 GeV/c in steps of 0.1 GeV/c). This gives 16 subsamples: 8 in the data, and the corresponding 8 in the Monte Carlo. Each of the 8 Monte Carlo subsamples is then further divided into two categories:

- **Signal:** NC resonant π^0 production (`Nuance` channels 6 and 8) and NC coherent π^0 production (`Nuance` channel 96)

- **Background:** All other event types

Once this is complete, for each momentum bin, the reconstructed π^0 mass distribution in data is fit with the corresponding MC signal and background mass distributions. That is, for each π^0 momentum bin, i, the result of the fit should be

$$N_i^{\text{data}} = a N_i^{\text{MC sig}} + b N_i^{\text{MC bkgd}} \tag{6.5}$$

where a (b) is the fraction of Monte Carlo signal (background) present in the data distribution (times an overall normalization factor, if necessary). It may seem that the sum of the MC signal and background fractions should be constrained to 1, but this is not necessary in the maximum likelihood fits; it emerges automatically in the results [110].

At the completion of the mass fit for each momentum bin, a histogram is filled with the extracted yield of signal events in that bin. After all fits have completed, this extracted yield histogram is compared with the Monte Carlo prediction for the distribution of signal NC π^0 events.

Validation: Fitting MC with MC

As a visual example of the procedure discussed above and validation of its result, we fit a fake data sample using MC templates (MC signal and MC background) that consist of the same type of Monte Carlo events. The fake data sample contains a subset of the events found in the template (a randomly chosen 10% of the full statistics). The true fractions of signal and background are known for this sample, and this example is a tautology. In the fit, the fake data sample is treated as if it were MiniBooNE detector data, *i.e.*, no information about the event type (signal or background) is used in the fit.

The fake data mass distribution and fit results for the inclusive mass distribution (not divided into bins of p_{π^0}) are shown in Fig. 6.2. Notice that the fitted and true fractions of signal events match, indicating that the fitting algorithm behaves as it should in this closure test. The small peak in the background contribution near the nominal π^0 mass is expected since the definition of "signal" is extremely limited; the background does contain some events with a π^0 in them.

An extended closure test can be performed exactly as above, but with 8 separate fits to the mass distribution for each of the 8 momentum bins. Instead of showing each of the 8 fits, we now show the results of all 8 fits in the form of a histogram containing the extracted signal yield and the fit error for each momentum bin (Fig. 6.3). For comparison, the fraction of signal events predicted by the Monte Carlo simulation for each of the momentum bins is also shown on the plot. Again, the distributions are in good agreement, as expected.

6.1.2   2D Fitting

A simultaneous fit to $\cos\theta_{\pi^0}$ *vs.* m_{π^0} is a much more powerful method of extracting the amount of signal in the NC Pi0Tuple, since the background fraction is nicely constrained by the mass distribution, but the coherent fraction is more distinct in the angular distribution. The combined fit of the two distributions allows for extraction of not only the signal fraction as a whole, but instead
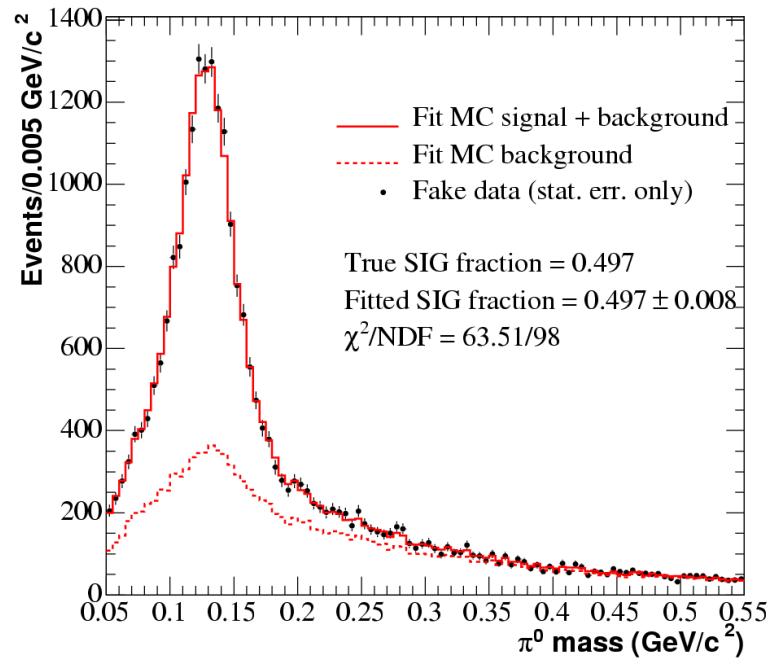
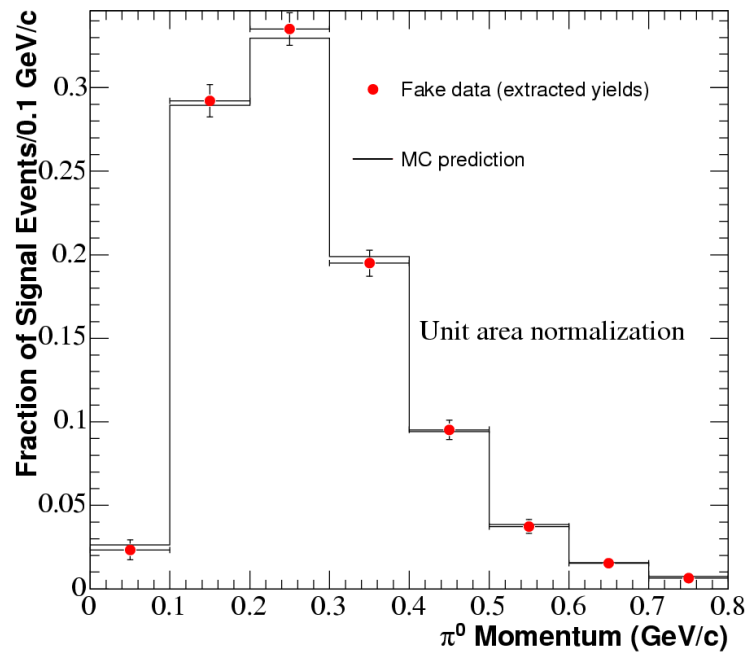Figure 6.2: Validation of the 1-dimensional fit procedure for reconstructed π^0 mass.

Figure 6.3: Validation of the 1-dimensional fit procedure for reconstructed π^0 mass in bins of reconstructed p_{π^0}

the signal fraction *separated* into its resonant and coherent contributions. As discussed in Chapter 2, π^0's which are produced coherently will tend to be more forward-going than resonantly produced π^0's. The result is that they can be distinguished from both resonant events and background events in the angular distribution. If only the angular distribution were used in a fit, the coherent portion would be easy to distinguish, but the resonant and background contributions would have similar shapes, making them indistinguishable. Fortunately, background events are distinct from signal events in the mass distribution (where now the coherent and resonant contributions have the same shape). A simultaneous fit of mass and angle combines the discriminating power of both distributions into one beautiful package.

In this procedure, the Monte Carlo is now divided into three separate categories (instead of just the two used in the 1-dimensional fits):

- **Resonant signal:** NC resonant π^0 production (`Nuance` channels 6 and 8)

- **Coherent signal:** NC coherent π^0 production (`Nuance` channel 96)

- **Background:** All other event types

Similar to the 1-dimensional fit, the data are projected into a histogram (this time 2-dimensional), and fit to find the best estimate of the fraction of each Monte Carlo category present in the data distribution.

Validation: Fitting MC with MC

As an example of the procedure and validation of its result, we again fit a fake data sample with MC templates containing the same type of events as in those the fake data sample. The fake data sample is constructed from a subset of the events found in the template (a randomly chosen 10% of the full statistics).

All of the preselection and analysis cuts are applied to the three MC categories. Each category of MC events is projected into a 2-dimensional histogram. The sum of these histograms constitutes the entire sample of Monte Carlo events passing all cuts. The events in the fake data sample, subject to the same preselection and analysis cuts, are also projected into a 2-dimensional histogram.

The fitting routine takes the three MC template histograms and the one data histogram, and maximizes the likelihood of the proportions of each MC template present in the data. The result of fitting a Monte Carlo sample with a higher-statistics MC template is shown in Fig. 6.4.

The top panel in the figure shows the 2-dimensional histogram of the fake data sample, $\cos\theta_{\pi^0}$ vs. m_{π^0}. Also shown on the top panel are the true fractions of each MC category that were present in the fake data sample, and the results of the fit with its estimated errors. The fitted fractions are within errors of the true fractions. The center panel shows the projection onto the x-axis for the fake data (black dots) and the fitted results (red histograms). Finally, the bottom panel of the figure shows the angular distribution of π^0 events relative to the beam direction. As discussed earlier in Sec. **??**, coherent π^0 events should be produced more in the forward direction than other π^0 events. This is clearly demonstrated by the dashed line in the bottom panel.

We see that the fit performs nicely for a fake data sample whose statistics are $\sim 10\%$ of the full template sample. The results of this fit, with the full Monte Carlo statistics in the templates (6 million events of all types), are shown in Table 6.1 for a fake data sample containing only the level of statistics available in the true MiniBooNE Pi0Tuple. Here we see that the fit has slightly underestimated the fraction of coherent π^0's present in the sample. The fit errors, with a discussion of the small bias seen here, will be addressed in Chapter 7.

	Resonant NC π^0	Coherent NC π^0	Background
True fraction	0.372	0.135	0.493
Fitted fraction	0.381 ± 0.010	0.121 ± 0.008	0.497 ± 0.008

Table 6.1: True and fitted fractions of resonant, coherent, and background events in a fake data sample that has the same level of statistics as the true MiniBooNE Pi0Tuple.

6.2 Flux-averaged cross section

This section will describe the method by which the flux-averaged cross section measurement is made. In general, a cross section is given by

$$\sigma = \frac{N_{\pi^0}}{\left(\int \Phi \, dE_\nu\right) N_{\text{POT}} \frac{N_A}{A} \rho V} \tag{6.6}$$
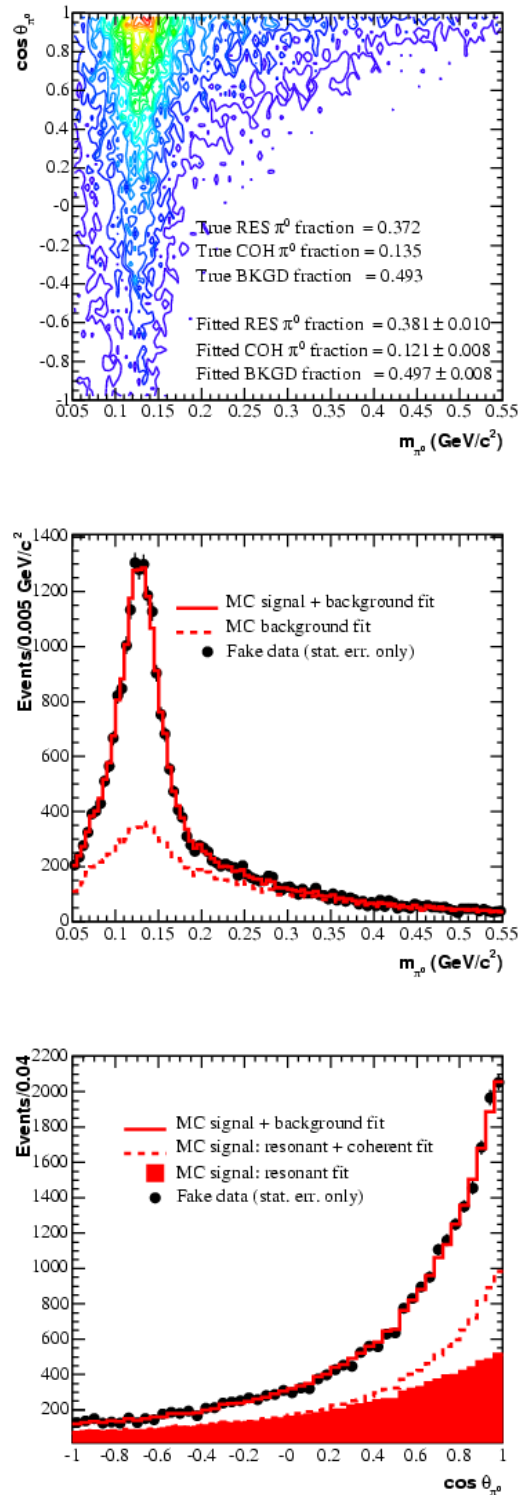
Figure 6.4: Result of simultaneous fit to mass and angle of all events passing NC π^0 preselection and analysis cuts. Fake data distribution (top), projection onto x-axis and result of fit (center), projection onto y-axis and result of fit (bottom).

where N_{π^0} is the efficiency-corrected number of NC π^0 events measured in the data, Φ is the flux (the number of neutrinos passing through a unit area), and N_{POT} is the number of protons on target corresponding to the measured number of events in the data. The factor $\frac{N_A}{A}\rho V$ accounts for the number of interaction targets present in the MiniBooNE oil, where N_A is Avogadro's number, A is the atomic number for the mineral oil ($CH_2 = 14$ g/mol), $\rho = 0.855$ g/cm^3 is the density of the oil, and V is the volume in which the events were detected.

6.2.1 Flux

The flux used in this measurement is measured from the CCQE data sample. This is the most robust and reliable flux estimate available for the MiniBooNE data; estimating fluxes from first principles introduces large uncertainties arising from not-so-well-known hadron production cross sections. It is also true that using the predicted (unoscillated) flux from the beam Monte Carlo simulation would be incorrect if a large $\nu_\mu \to \nu_s$ oscillation were present. That is, if ν_μ's were oscillating to ν_s's (which would not produce π^0 events in the detector), the simulated ν_μ flux would be an over-prediction. Further discussion of the method for determining the flux and details of the extraction may be found in Ref. [111]. Approximately 40% of the overall number of events are CCQE. The predicted rate of CCQE events is compared to that for the NC single π^0 resonant and coherent events in Fig. 6.5, showing that these two event samples have nearly the same mean neutrino energy and cover the same energy range.

Rather than measuring the NC π^0 cross section for the combined resonant and coherent events, the more correct thing to do is to measure the two cross sections separately. There are two reasons for this:

1. the preselection and analysis cut efficiencies are different for resonant and coherent NC single π^0 events, and

2. the average energy of neutrinos producing these events is also slightly different.

The average energy of resonant (coherent) events is found by

$$\langle E_{\nu,\text{RES(COH)}} \rangle = \frac{\int \Phi_\nu \cdot \sigma_{\text{RES(COH)}} \cdot E_\nu dE_\nu}{\int \Phi_\nu \cdot \sigma_{\text{RES(COH)}} dE_\nu}. \tag{6.7}$$
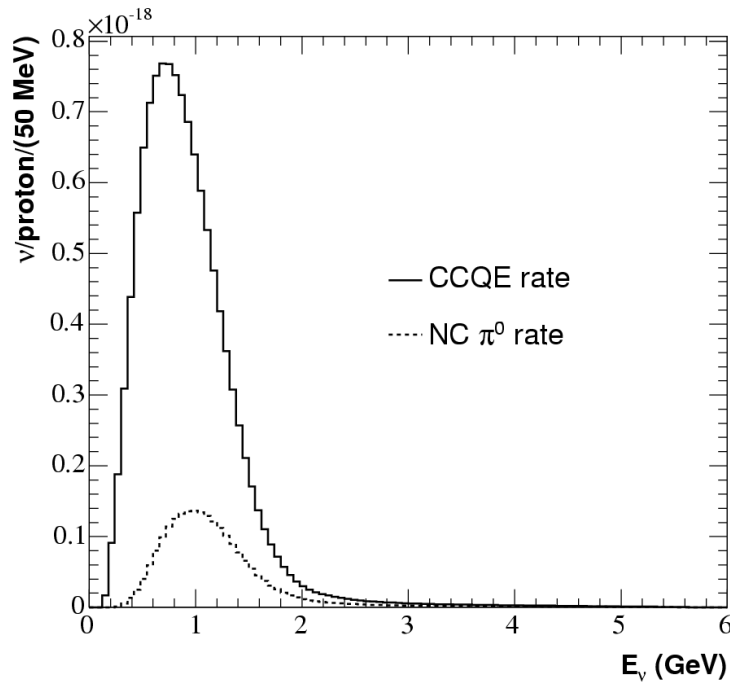
Figure 6.5: Predicted rates for CCQE events and NC π^0 events

The method does assume that the `Nuance` prediction for the cross section has the correct shape, but this assumption cannot be avoided, since we are unable to reconstruct neutrino energy for the neutral current events.

The portion of the flux that is relevant for NC π^0 events can be found by reweighting the flux with an "efficiency" curve whose shape is identical to the `Nuance` prediction for the NC π^0 cross section (resonant or coherent). The curve is normalized such that the efficiency is 1 in the energy bin containing the $< E_\nu >$ determined by Eq. 6.7. Other energy bins of this efficiency curve are set to the ratio of $\sigma_{E_\nu}/\sigma_{<E_\nu>}$. The integral of the "efficiency"-reweighted flux is then used in the denominator of Eq. 6.6.

6.2.2   Number of Protons on Target

The number of protons on target for the MiniBooNE data sample is calculated using hardware in the MiniBooNE beam line. Details of the calculations and discussion of systematic errors may be found in Refs. [112] and [113]. The estimated error on the number of protons on target is $\sim 2\%$.

6.2.3   Number of NC π^0 Events

Determination of the number of NC π^0 events is achieved by use of the 2-dimensional fitting method described in Sec. 6.1.2. The number of resonant (coherent) events extracted from the full NC Pi0Tuple data sample with the 2-dimensional fit is then corrected for the overall cut efficiency of resonant (coherent) events. The efficiency of preselection and analysis cuts for resonant events (as determined by MC simulations) is 19%, while the efficiency for the same cuts on coherent events is 24%.

6.2.4   Validation of the Procedure

A fake data sample is fit using the 2-dimensional fitting procedure described in Section 6.1.2 to determine the number of coherent and resonant events present in the sample. Each of these is then divided by its cut efficiency to give the "true" number of events.

Since this is a test using Monte Carlo events, the number of protons on target is known perfectly. Finally, the average energies of resonant and coherent events are calculated by the method in Section 6.2.1. The true (Monte Carlo) value of each cross section at its average energy is compared to the "measured" cross section for the fake data sample. Results are shown in Table 6.2.

	Average energy (GeV)	True cross section $(10^{-36}\ \mathrm{cm}^2)$	"Measured" cross section $(10^{-36}\ \mathrm{cm}^2)$
NC Resonant π^0	1.27	0.0137	0.0138 ± 0.0004
NC Coherent π^0	1.12	0.0026	0.0024 ± 0.0001

Table 6.2: Validation of the procedure used to extract the flux-averaged cross section for resonant and coherent events.

We see that the "measurement" of the resonant cross section was successful, but the coherent cross section is lower than the true value. This is a result of the bias seen earlier in the 2-dimensional fit, and will be discussed further in Chapter 7.

Chapter 7

Error Analysis

This chapter addresses error analysis for the NC π^0 cross section measurement.

7.1   2D Fit Bias

A better estimate of the inherent errors on the fractions due to the fitting algorithm is obtained by running 1000 toy Monte Carlo experiments in which the true fractions are known and the fake data has the same level of statistics as the MiniBooNE Pi0Tuple in each experiment. The distribution of fit results should be a Gaussian centered around the true fraction for each fitted fraction. This is shown in Fig. 7.1. The top (middle, bottom) panel shows the true and fitted fraction of resonant (coherent, background) events for the 1000 experiments. All panels of the figure show that the distribution of fitted fractions is wider than the true distribution, but the means of the two distributions coincide in each case.

For the study shown above, the fractions of resonant, coherent, and background events are identical or nearly identical to the fractions of those same categories in the fake data. A small bias in the fitting technique is found by changing the relative fractions in the fake data, but leaving the fit templates unchanged. This is shown in Fig. 7.2. In each of the 1000 experiments here, the fraction of coherent NC π^0 events in the *fake data* was reduced to half the original Monte Carlo fraction (resonant and background fractions were untouched). The relative amounts of resonant, coherent, and background in the *templates* remained unchanged. The bias is clearly shown in the
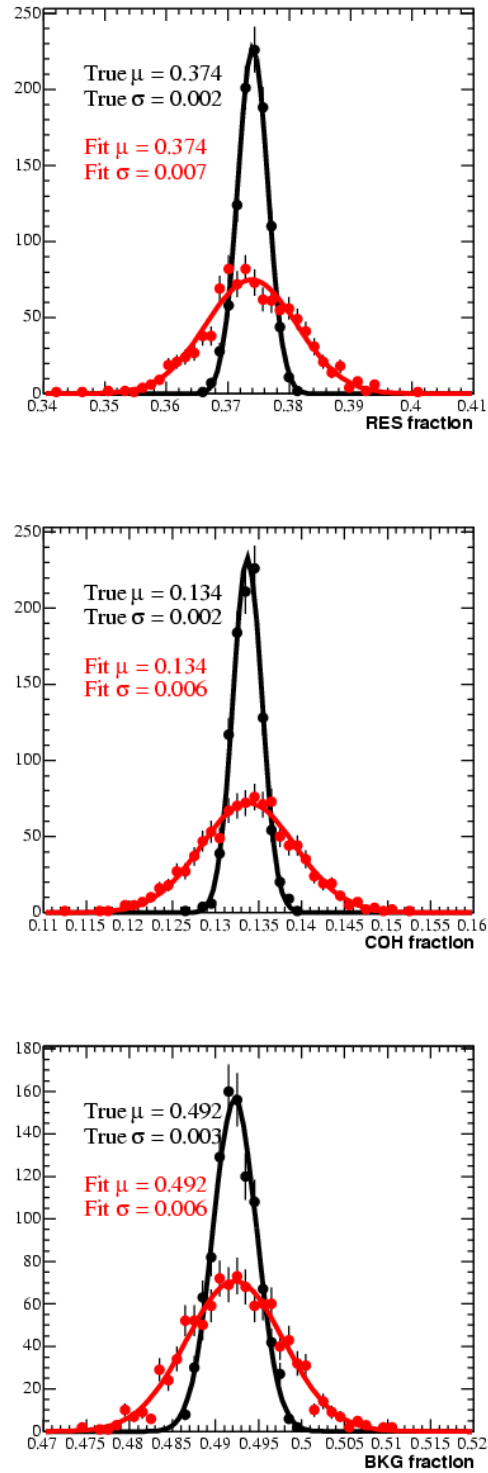
Figure 7.1: Results of 1000 toy MC experiments where the true and fitted fractions of resonant, coherent, and background events are plotted. True fractions are shown in black. Fitted fractions are shown in red.
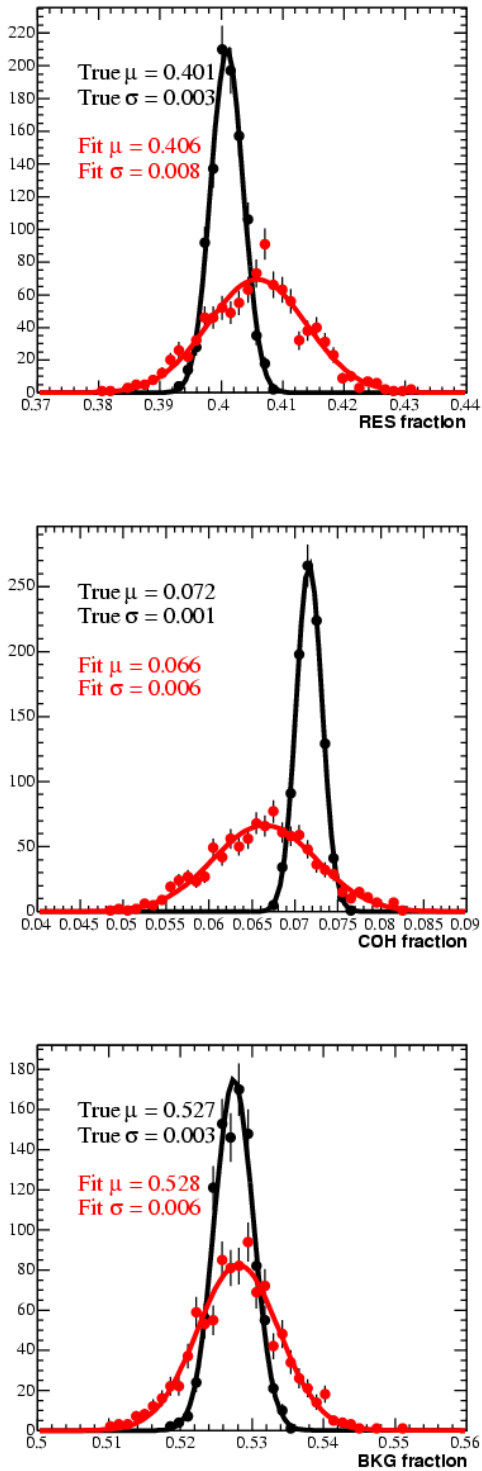
Figure 7.2: Results of 1000 toy MC experiments where the fake data in each experiment contains 50% fewer coherent events than the relative fraction in the template. The true (fitted) fractions of resonant, coherent, and background present in the fake data are shown in black (red).

figure. The 2-dimensional fit tends to over-predict the fraction of resonant and under-predict the fraction of coherent in the fake data sample, however the fitted mean is still within errors of the true mean in each case.

To account for this bias, a study was performed to determine the maximum bias of the fitting procedure. This was done by systematically changing the amount of each contribution (resonant, coherent, and background) in the fake data sample and re-fitting with unchanged MC templates. The results are shown in Fig. 7.3. Even in the worst case scenario (where the amount of background in the fake data is changed by nearly 100%), the fitted fraction of resonant is still only 10% off from the true fraction. This demonstrates that the fitting procedure is robust, even under extreme variations of the fitted sample. In truth, we need not take the full extrema (*i.e.*, 100% change in the fraction of background or resonant events) as the fit bias, since the largest backgrounds in the NC π^0 sample (CCQE and CC $\pi+$) are constrained by other MiniBooNE data samples (the aforementioned), and resonant production is constrained by information from other experiments.

7.2   Fiducial Volume Cut

To determine the systematic error associated with the fiducial volume cut, the distributions of data and Monte Carlo events passing all NC Pi0Tuple selection requirements *except* the fiducial volume cut are compared. The fractions of these events surviving all cuts including the fiducial volume cut are shown in Table 7.1. The systematic uncertainty is taken as 2.9%, the difference in the fractions of events passing the cut.

Fraction of events	Data	Cocktail+strobe Monte Carlo
All cuts *except* fiducial volume	1	1
All cuts *including* fiducial volume	0.845	0.816

Table 7.1: Fractions of data and Monte Carlo events surviving the fiducial volume cut.
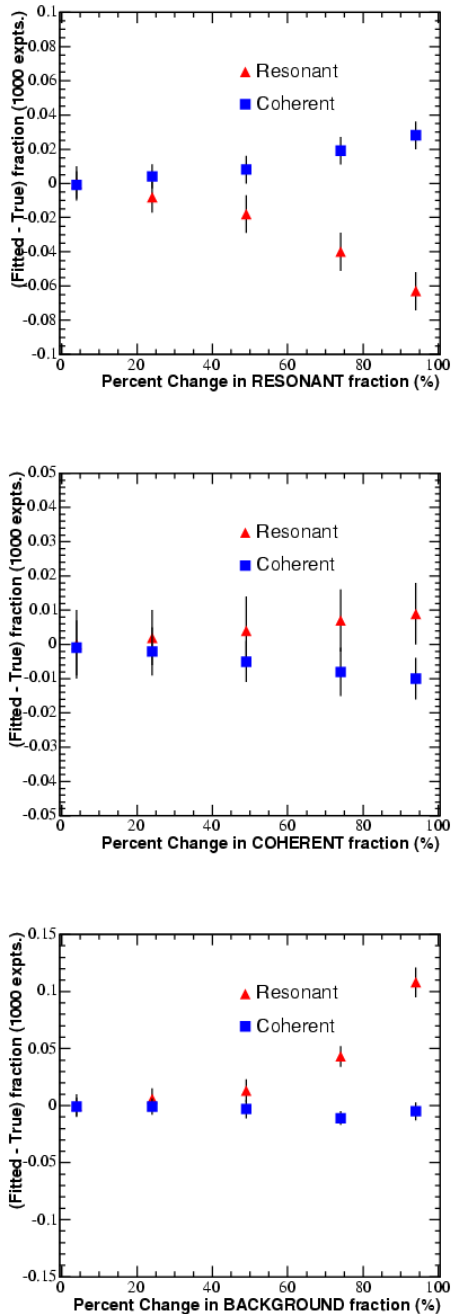
Figure 7.3: Results of toy MC experiments to determine the maximum fit bias in the 2-dimensional fitting procedure. The top (middle, bottom) panel shows the difference between the fitted and true fraction for resonant (blue) and coherent (red) events when the fraction of resonant (coherent, background) in the fake data sample was changed by the amount indicated on the abscissa. Each pair of resonant and coherent dots represents 1000 toy MC experiments, as in Fig. 7.2. Note that the vertical scales are different.

7.3   Model Systematic Uncertainties

Systematic errors due to uncertainties in model parameters are treated by varying the parameters within reasonable limits to see the effect on the cross section measurement. The models in question include various aspects of the detector optical model, as well as a number of cross section model parameters.

The model uncertainties are addressed by Monte Carlo simulations called "unisims" (where only one model parameter is changed per simulation). Each unisim is treated as if it were data, and the fitting procedure is performed to measure the flux-averaged cross section in each sample. The flux over which we average in each case is the flux from the unisim in question. This way, for a given parameter change, if the number of observed π^0 events changes in the same direction as the flux, the overall change in the cross section may be small compared to the change in the parameter itself.

The fractional error on the cross section for a change of parameter y in unisim j is then calculated as:

$$\left(\frac{\delta\sigma}{\sigma}\right)^2 = \left(\frac{\partial f}{\partial y_j}\right)^T [\delta y_j \delta y_k] \left(\frac{\partial f}{\partial y_k}\right) + \sum_j \left(\delta\frac{\partial f}{\partial y_j}\right)^2 (\delta y_j)^2 \tag{7.1}$$

where

$$\begin{aligned}
\frac{\partial f}{\partial y_j} &= \frac{1}{\varepsilon_{\text{central value}}} \frac{1}{y_j^{\text{unisim}} - y^{\text{central value}}} \left(\frac{N_{\text{unisim}j}^{\text{fitted}}}{N_{\text{unisim}j}^{\text{true}}} - \frac{N_{\text{central value}}^{\text{fitted}}}{N_{\text{central value}}^{\text{true}}},\right) \\
\delta\frac{\partial f}{\partial y_j} &= \left(\frac{\delta N_{\text{unisim}j}^{\text{fit}}}{\varepsilon_{\text{centralvalue}} N_{\text{unisim}j}^{\text{true}}} \frac{1}{\Delta y_j}\right),
\end{aligned} \tag{7.2}$$

and $[\delta y_j \delta y_k]$ will eventually be a matrix of correlated errors[1].

Variations in optical model parameters are being investigated. We expect the systematic errors due to optical model parameter variations to be small since MiniBooNE is calibrated using detected light; this provides constraints on the tunable parameters. In the absence of detector optical model unisims at this time, we use samples of cube data to estimate the overall energy scale uncertainty as 5% [114].

---

[1] At the time of this writing, the various working groups were in the process of assessing the correlations of various parameters. In the absence of this matrix, the unisim variations were taken as uncorrelated 1 σ deviations from the central value.

For the flux-averaged cross section measurement, the uncertainty in the flux measurement does not contribute as a single systematic error, since the flux measured in each unisim variation is used in the calculation of the cross section errors. That is, for each unisim i, the fractional systematic error on the flux-averaged cross section is calculated as

$$\frac{\delta\sigma_i}{\sigma_i} = \frac{\sigma_i - \sigma_0}{\sigma_0} \frac{1}{y_1 - y_0} \tag{7.3}$$

where y_1 and y_0 are the unisim and central value parameters, respectively.

The uncertainty in the flux shape does come into the estimation of errors for the distributions of reconstructed variables, however. The shapes of these distributions (like that shown in Fig. 6.3) are somewhat dependent on the shape of the predicted Monte Carlo flux. Therefore, unisim variations of beam Monte Carlo parameters were used to estimate the overall uncertainty in the flux shape for these distributions. The correlated errors arising from flux shape uncertainty are shown in Fig. 7.4. For the overall systematic uncertainty in the NC π^0 analysis reconstructed variables due to these flux shape variations we take 15%, as determined through discussions with the beam Monte Carlo working group [115].

7.4   Summary

A summary of the sources of systematic uncertainty is given in Table 7.2 for all model parameter variations. Including all of these errors, we find the total systematic uncertainty to be 33% on the resonant flux-averaged cross section measurement and 43% on the coherent flux-averaged cross section measurement.
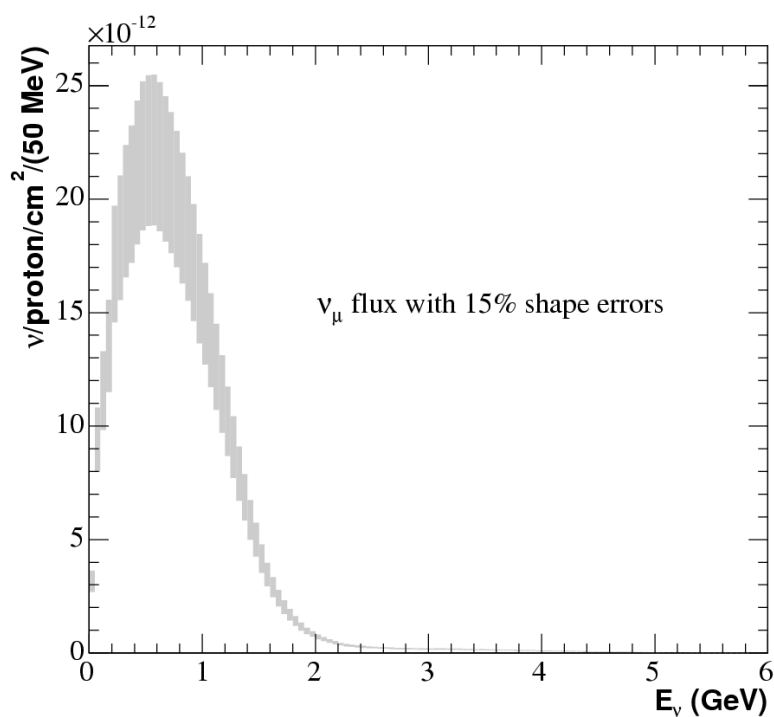
Figure 7.4: Systematic error arising from uncertainty in prediction of flux shape. The error bars represent the uncertainty in flux shape from 8 unisim variations of beam Monte Carlo parameters.

Source	Resonant Errors (%)	Coherent Errors (%)
(1) CROSS SECTION MODEL PARAMETERS		
m_A in quasi-elastic scattering($\pm 10\%$)	10.7	7.5
m_A in single pion production ($\pm 20\%$)	7.0	21.5
m_A in multiple pion production ($\pm 35\%$)	7.3	12.7
Fermi gas model ($p_F \pm 14\%, E_B \pm 100\%$)	14.3	6.4
Nucleon spin ($\Delta s \pm 10\%$)	6.4	11.5
Δ width ($\pm 4.2\%$)	10.7	7.4
nuclear effects for pions in ^{12}C (absorption, $\pm 25\%$)	8.0	16.8
nuclear effects for pions in ^{12}C (charge exchange, $\pm 30\%$)	11.5	13.3
pion-less Δ decay cross section ($\pm 50\%$)	16.4	21.2
(2) ENERGY SCALE		
detector energy scale uncertainty	5.0	5.0
(3) FIDUCIAL VOLUME		
fiducial volume cut	2.9	2.9
(4) 2D FIT BIAS		
background cross section ($\pm 30\%$)	2.0	2.0
resonant cross section ($\pm 30\%$)	1.0	1.0
coherent cross section ($\pm 100\%$)	1.0	1.0

Table 7.2: Summary of the systematic errors on the NC π^0 cross section measurements.

Chapter 8

Results

Having discussed the methods used to extract NC π^0 signal events from the (rather low purity) sample of NC Pi0Tuple events, and the systematic errors, we now perform the fits on MiniBooNE data. The data sample consists of runs taken between December, 2002, and January, 2005 (Run numbers 3,000 to 10,493). The number of candidate NC π^0 events in this sample (after preselection requirements only) is 38,550. Once the additional analysis requirements are applied, the sample contains 21,044 candidate events.

First, we present comparisons of the reconstructed variables p_{π^0}, $\cos\theta_{\pi^0}$, and $\cos\theta_{CM}$. The distribution of signal events extracted from data is compared to the Monte Carlo prediction in each case. The 1-dimensional fitting procedure introduced in Section 6.1.1 is used to produce the data signal distributions. Also presented here are the flux-averaged cross section measurements for NC resonant and coherent single π^0 production. These measurements are made using the 2-dimensional fitting procedure of Section 6.1.2.

8.1   Reconstructed Variables

Unit area normalized comparisons of the extracted signal as a function of the reconstructed variables are shown in Figs. 8.1, 8.2, and 8.3. Data points include statistical and fit errors. The dark grey boxes on the Monte Carlo prediction represent the systematic error associated with 1σ variations of cross section model parameters (as discussed in the previous chapter) added in quadrature with

the overall flux shape uncertainty (15%), the overall energy scale uncertainty (5%), and the fiducial volume cut uncertainty (2.9%). The light grey error bars show the amount of the overall error associated with only the cross section parameter variations.

Figure 8.1: Result of 1-dimensional fits to data mass distribution in bins of reconstructed π^0 momentum. Dark grey error bands represent total systematic and statistical error. Light grey error bands represent systematic errors from 1 σ cross section parameter variations.

8.2 Cross Section Measurement

Using the 2-dimensional fitting technique described above, the full set of data in the NC Pi0Tuple (corresponding to $\sim 3.2 \times 10^{20}$ protons on target) is fit using templates created from a cocktail+strobe Monte Carlo sample (as discussed in Section 4.4). The fitted fractions of resonant, coherent, and background events and the overall number of each type (determined from the fit fractions) are shown in Table 8.1. The results are shown in plot form in Fig. 8.4. The extracted numbers of resonant and coherent events correspond to the measured flux-averaged cross sections,
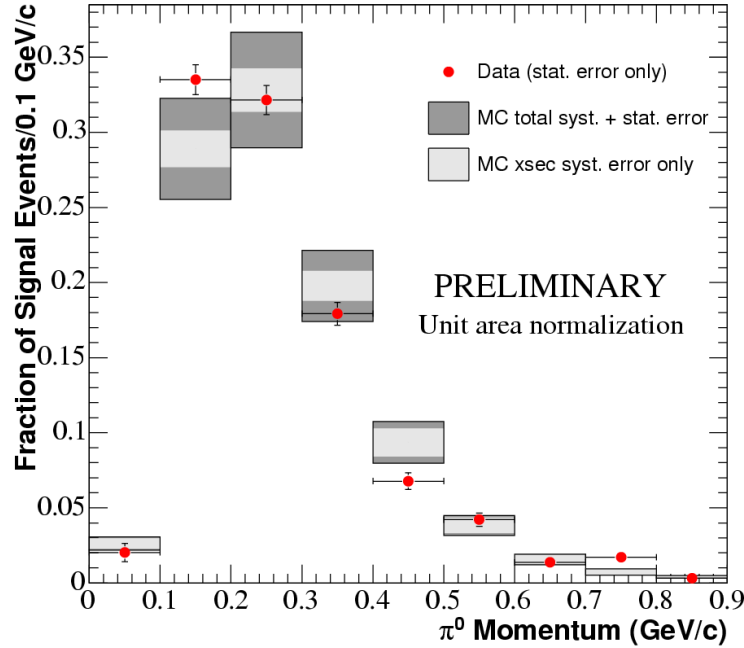
Figure 8.2: Result of 1-dimensional fits to data mass distribution in bins of reconstructed $\cos\theta_{\pi^0}$. Dark grey error bands represent total systematic and statistical error. Light grey error bands represent systematic errors from $1\ \sigma$ cross section parameter variations.

respectively:

$$\sigma(\nu_\mu\ \mathcal{N} \to \nu_\mu\ \mathcal{N}\ \pi^0) = (1.28 \pm 0.11\ (stat.) \pm 0.43\ (syst.)) \times 10^{-38}\ \mathrm{cm}^2/\mathrm{CH}_2$$

$$\sigma(\nu_\mu\ \mathcal{A} \to \nu_\mu\ \mathcal{A}\ \pi^0) = (7.7 \pm 1.6\ (stat.) \pm 3.6\ (syst.)) \times 10^{-40}\ \mathrm{cm}^2/\mathrm{CH}_2.$$

The mean neutrino energy of the resonant π^0 events is $E_\nu = 1.26 \pm 0.06$ GeV, and coherent π^0 events is $E_\nu = 1.12 \pm 0.06$ GeV. The results are shown in comparison with various theoretical model predictions and other existing world measurements in Figs. 8.5 and 8.6.
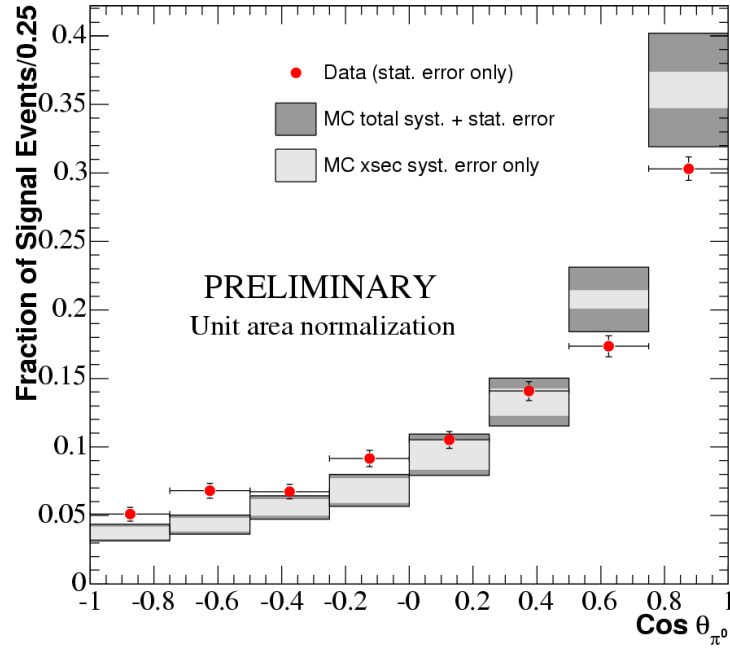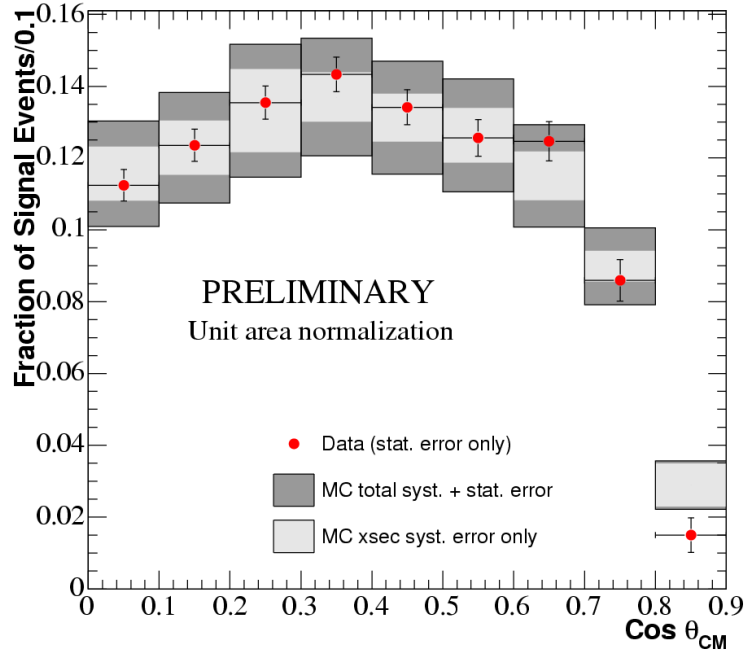
Figure 8.3: Result of 1-dimensional fits to data mass distribution in bins of reconstructed $\cos\theta_{CM}$. Dark grey error bands represent total systematic and statistical error. Light grey error bands represent systematic errors from 1 σ cross section parameter variations.

	Resonant NC π^0	Coherent NC π^0	Background
Fitted fraction	0.506 ± 0.012	0.058 ± 0.008	0.437 ± 0.009
Number of events	10639 ± 248	1216 ± 173	9187 ± 183

Table 8.1: Results of 2-dimensional fit to data (NC Pi0Tuple) using templates created from cocktail+strobe Monte Carlo. Results are reported as the fitted fractions of each category of events with errors. The overall number of each event category is determined by multiplying the number of entries in the Pi0Tuple (after all cuts) by the fitted fractions.
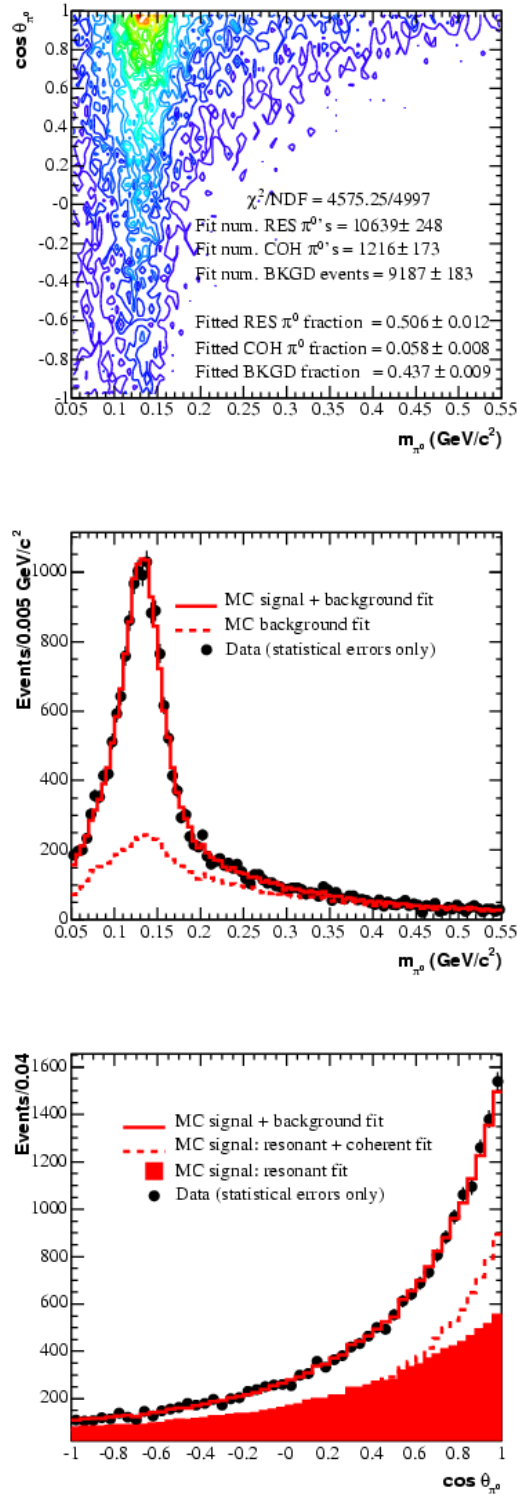
Figure 8.4: Result of simultaneous fit to mass and angle of all events passing NC π^0 preselection and analysis cuts. Data distribution (top), projection onto x-axis and result of fit (center), projection onto y-axis and result of fit (bottom).
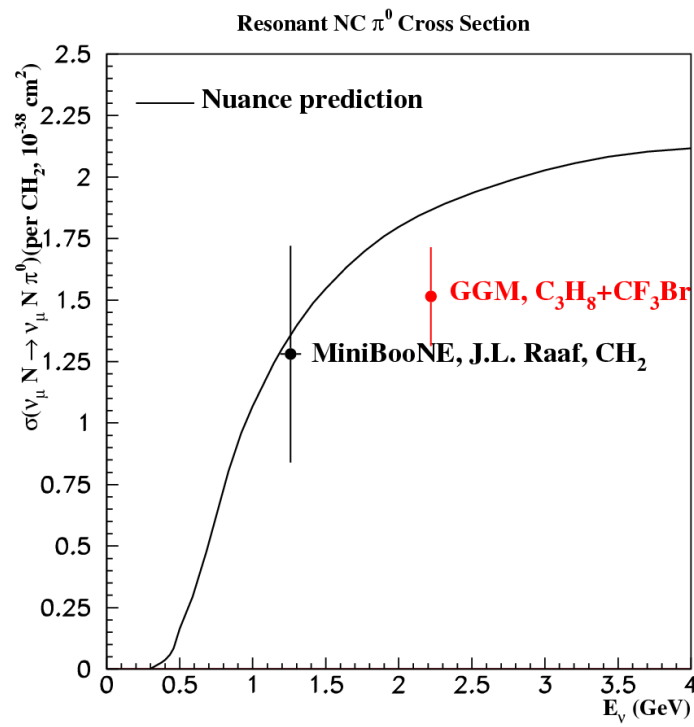
Figure 8.5: Result of the flux-averaged resonant single π^0 cross section measurement with `Nuance` theoretical model prediction for CH_2 and existing world data.
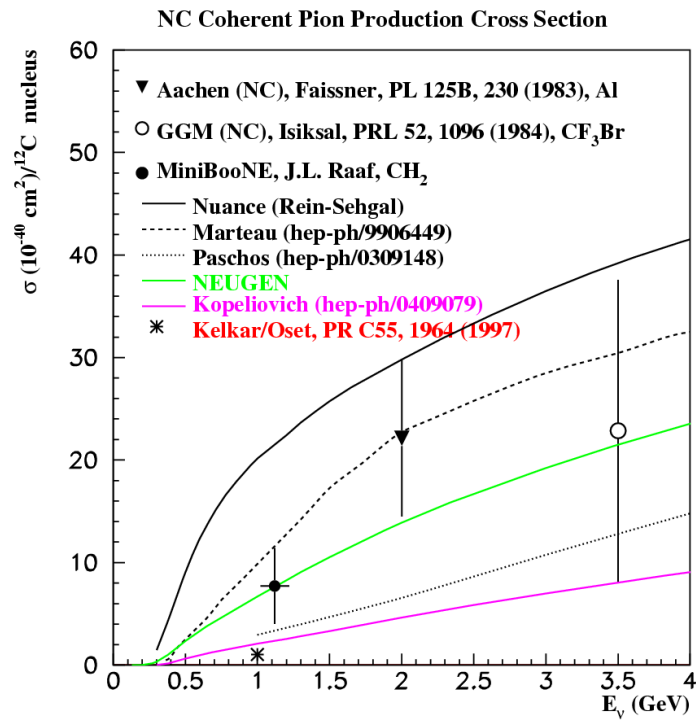
Figure 8.6: Result of the flux-averaged coherent single π^0 cross section measurement with various theoretical model predictions and existing world data at low neutrino energies.

Bibliography

[1] W. Pauli, *Letter to the Physical Society of Tubingen (1930), Reproduced in Brown, L. M. Physics Today,***31**,*(9):23* (1978).

[2] F. Reines and C. L. Cowan, Phys. Rev. **90**:492 (1953).

[3] G. Danby *et al.*, Phys. Rev. Lett. **9(1)**:36–44 (1962).

[4] [DONUT collaboration], K. Kodama *et al.*, Phys. Lett. **B 204**:218–224 (2001). [arXiv:hep-ex/0012035]

[5] [Particle Data Group collaboration], S. Eidelman *et al.*, Phys. Lett. **B 592**:1–1109, `http://pdg.lbl.gov` (2004).

[6] F. Boehm and P. Vogel, *Physics of Massive Neutrinos*, Cambridge University Press (1992).

[7] T. Yanagida, *Proceedings of the Workshop on Unified Theory and the Baryon Number of the Universe*, p. 95, KEK, Japan (1979).

[8] M. Gell-Mann, P. Ramond, and R. Slansky, *Supergravity*, North Holland, Amsterdam (1979).

[9] R. N. Mohapatra and G. Senjanović, Phys. Rev. Lett. **44**:912 (1980).

[10] N. Cabibbo, Phys. Rev. Lett. **10**:531 (1963).

[11] M. Kobayashi and T. Maskawa, Prog. Theo. Phys. **49**:652 (1973).

[12] R. Davis, Prog. Part. Nucl. Phys. **32**:13 (1994).

[13] [GALLEX collaboration], W. Hampel *et al.*, Phys. Lett. **B 447**:127–133 (1999).

[14] [GNO collaboration], M. Altmann *et al.*, Phys. Lett. **B 490**:16–26 (2000). [arXiv:hep-ex/0006034]

[15] [SAGE collaboration], J. N. Abdurashitov *et al.*, Sov. Phys.–JETP **95**:181 (2002). [arXiv:astro-ph/0204245]

[16] [Super-Kamiokande collaboration], S. Fukuda *et al.*, Phys. Rev. Lett. **86**:5656 (2001). [arXiv:hep-ex/0103033]

[17] [SNO collaboration], B. Aharmim *et al.* (2005). [arXiv:nucl-ex/0502021]

[18] [Kamiokande-II collaboration], K. S. Hirata *et al.*, Phys. Lett. **B 280**:146 (1992).

[19] [Super-Kamiokande collaboration], Y. Ashie *et al.* . [arXiv:hep-ex/0501064]

[20] [MACRO collaboration], A. Surdo *et al.*, Nucl. Phys. B (Proc. Suppl.) **110**:342 (2002).

[21] [K2K collaboration], M. H. Ahn *et al.*, Phys. Rev. Lett. **90** (2003). [arXiv:hep-ex/0212007]

[22] [Soudan-2 collaboration], W. W. M. Allison *et al.*, Phys. Lett. **B 449**:137 (1999). [arXiv:hep-ex/9901024]

[23] [CHOOZ collaboration], M. Apollonio *et al.*, Phys. Lett. **B 466**:415 (1999). [arXiv:hep-ex/9907037]

[24] [Palo Verde collaboration], F. Boehm *et al.*, Phys. Rev. **D 64**:112001 (2001). [arXiv:hep-ex/0107009]

[25] [KamLAND collaboration], K. Eguchi *et al.*, Phys. Rev. Lett. **90** (2003). [arXiv:hep-ph/0212021]

[26] [LSND collaboration], A. Aguilar *et al.*, Phys. Rev. **D 64** (2001). [arXiv:hep-ex/0104049]

[27] G. Barenboim and J. Lykken, Phys. Lett. **B 554**:73–80 (2003). [arXiv:hep-ph/0210411]

[28] G. Barenboim, L. Borissov, and J. Lykken (2002). [arXiv:hep-ph/0212116]

[29] [LSND collaboration], C. Athanassopoulos *et al.*, Nucl. Inst. & Meth. **A 388**:149–172 (1997).

[30] A. A. Aguilar-Arevalo *et al.*, *The MiniBooNE Run Plan*, `http://www-boone.fnal.gov/ publicpages/` (2003).

[31] D. Rein and L. M. Sehgal, Ann. Phys. (NY) **133**:79–153 (1981).

[32] R. P. Feynman, M. Kislinger, and F. Ravndal, Phys. Rev. **D 3(11)**:2706–2732 (1971).

[33] D. Rein, Z. Phys. **C 35**:43–64 (1987).

[34] D. Binosi and L. Theussl, Comp. Phys. Comm. **161**:76–86 (2004).

[35] B. Z. Kopeliovich and P. Marage, Phys. Rev. **C 55(4)**:1964–1971 (1997).

[36] D. Rein and L. M. Sehgal, Nucl. Phys. B **223**:29–44 (1983).

[37] E. A. Paschos and A. Kartavtsev, arXiv:hep-ph/0309148 (2003).

[38] A. A. Belkov and B. Z. Kopeliovich, Sov. J. Nucl. Phys. **46**:499 (1987).

[39] G. Kelkar, E. Oset, and P. Fernández de Córdoba, Phys. Rev. **C 55(4)**:1964–1971 (1997).

[40] J. Marteau *et al.*, arXiv:hep-ph/9906449 (1999).

[41] S. L. Adler, Phys. Rev. **B 135(4)**:963–966 (1964).

[42] M. Gell-Mann, Phys. Rev. **111**:362 (1958).

[43] M. L. Goldberger and S. B. Treiman, Phys. Rev. **109**:193 (1960).

[44] Y. Nambu, Phys. Rev. Lett. **4**:380 (1960).

[45] M. Gell-Mann and M. Levy, Nuovo Cimento **16**:705, and references listed within (1960).

[46] J. J. Sakurai, Phys. Rev. Lett. **22**:981–984 (1969).

[47] [BEBC WA59 collaboration], P. Marage *et al.*, Z. Phys. **C 49**:385–394 (1991).

[48] C. A. Piketty and L. Stodolsky, Nucl. Phys. B **15**:571–600 (1970).

[49] K. S. Lackner, Nucl. Phys. B **153**:526–545 (1979).

[50] R. D. Woods and D. S. Saxon, Phys. Rev. **95**:577–578 (1954).

[51] H. M. Gallagher and M. C. Goodman, Nucl. Phys. B (Proc. Suppl.) **112**:188–194, `http://www.hep.umn.edu/~gallag/neugen/` (2002).

[52] S. J. Barish *et al.*, Phys. Rev. Lett. **33**:448–451 (1974).

[53] M. Derrick, Phys. Rev. **D 23**:569–575 (1981).

[54] E. A. Hawker, submitted to NuInt'02 proceedings, to be published in Nucl. Phys. B Proc. Suppl.

[55] G. L. Fogli and G. Nardulli, Nucl. Phys. B **165**:162–184 (1980).

[56] W. Krenz *et al.*, Nucl. Phys. B **135**:45–65 (1978).

[57] W. Lee *et al.*, Phys. Rev. Lett. **38(5)**:202–204 (1977).

[58] P. J. Nienaber, *Single π^0 Production in Charged Current and Neutral Current Neutrino Interactions*, Ph.D. thesis, University of Illinois at Urbana-Champaign (1998).

[59] [K2K collaboration], S. Nakayama, C. Mauger, *et al.* (2004). [arXiv:hep-ex/0408134]

[60] [Aachen-Padova collaboration], H. Faissner *et al.*, Phys. Lett. **B 125(2,3)**:230–236 (1983).

[61] E. Isiksal, D. Rein, and J. G. Morfín, Phys. Rev. Lett. **52(13)**:1096–1099 (1984).

[62] [SKAT collaboration], H. J. Grabosch *et al.*, Z. Phys. **C 31**:203 (1986).

[63] C. Baltay *et al.*, Phys. Rev. Lett. **57**:2629 (1986).

[64] [E632 collaboration], S. Willocq *et al.*, Phys. Rev. **D 47(7)**:2661–2674 (1993).

[65] [CHARM collaboration], F. Bergsma *et al.*, Phys. Lett. **B 157**:469 (1985).

[66] I. Stancu *et al.*, *Technical Design Report for the 8 GeV Beam*, `http://www-boone.fnal.gov/publicpages/` (2001).

[67] T. Kobilarcik, J. DeVoy, and C. Moore, *Automatic Beamline Correction*, proceedings of the 2003 Particle Accelerator Conference (2003).

[68] L. Bartoszek, `http://www.bartoszekeng.com`, Bartoszek Engineering.

[69] *GEANT Detector Description and Simulation Tool*, CERN Program Library Long Writeup W5013 (1993).

[70] I. Stancu *et al.*, *Technical Design Report for the MiniBooNE Neutrino Beam*, `http://www-boone.fnal.gov/beam/` (2001).

[71] E. D. Zimmerman *et al.*, LMC Technical Design Report.

[72] M. Sorel, *Search for Sterile Neutrinos Using the MiniBooNE Beam*, Ph.D. thesis, Columbia University (2005).

[73] I. Stancu *et al.*, *The MiniBooNE Detector Technical Design Report*, `http://www-boone.fnal.gov/publicpages/` (2001).

[74] R. A. Johnson, *MiniBooNE Mineral Oil: Request for Proposal Information Outline*, `http://www.physics.uc.edu/~johnson/Boone/oil_page/RFP.html` (2001).

[75] R. A. Johnson, *MiniBooNE Mineral Oil: Technical Specification*, `http://www.physics.uc.edu/~johnson/Boone/oil_page/tech_specs.html`, unpublished (2001).

[76] H.-O. Meyer, *Index of Refraction of Marcol 7*, BooNE Technical Note 90 (2003).

[77] Hamamatsu, `http://www.hamamatsu.com`.

[78] B. T. Fleming, *Inner Structure and Outer Limits: Precision QCD and Electroweak Tests from Neutrino Experiments*, Ph.D. thesis, Columbia University (2002).

[79] B. T. Fleming *et al.*, IEEE Trans. Nucl. Sci. **49**:984–988 (2002).

[80] J. A. Green, `http://www-boone.fnal.gov/software_and_analysis/current_framework/doc/index.html`, for a full description of the latency filter, see the Analysis Framework user manual.

[81] A. A. Aguilar-Arevalo *et al.*, *The NuMI Event Trigger Design*, MiniBooNE Technical Note 155 (2005).

[82] R. Imlay, W. Metcalf, M. Sung, and M. O. Wascko, *The Calibration Systems for the MiniBooNE Experiment*, MiniBooNE Technical Note (2004).

[83] R. B. Patterson, *The PMT Charge Calculation*, BooNE Technical Note 83 (2003).

[84] R. M. Sternheimer, Phys. Rev. **117**:485 (1960).

[85] J. B. Birks, *The Theory and Practice of Scintillation Counting*, Macmillan, New York (1964).

[86] R. L. Craun and D. L. Smith, Nucl. Inst. & Meth. **80**:239 (1970).

[87] R. Imlay, W. Metcalf, M. Sung, and M. O. Wascko, *Light Scattering with Bare Fiber Events*, BooNE Technical Note 101 (2003).

[88] A. O. Bazarko, P. D. Meyers, R. B. Patterson, and H. A. Tanaka, *Studies of Scattering in Marcol 7 Mineral Oil*, BooNE Technical Note 144 (2004).

[89] B. C. Brown, S. Maza, A. Pla-Dalmau, and H. A. Tanaka, *Studies of the Optical Properties of Marcol 7 Mineral Oil*, BooNE Technical Note 145 (2004).

[90] D. Toptygin, *Time Resolved Fluorescence of MiniBooNE Mineral Oil*, report Nos. 1-8 (2004).

[91] S. Breitzmann and H. O. Meyer, *Solubility of O_2, N_2, and Ar in Mineral Oil*, BooNE Technical Note 65 (2002).

[92] N. Suwonjandee and R. A. Johnson, *Scintillation Chamber Index*, `http://www.physics.uc.edu/~johnson/Boone/oil_page/scintillation/` (2001).

[93] E. Hawker, G. Garvey, S. Freudenstein, A. Lathrop, and G. Mills, *Oil Attenuation Measurements with the 'Bama Oil Tester*, BooNE Technical Note 31 (2001).

[94] B. C. Brown *et al.*, *Study of Scintillation, Fluorescence and Scattering in Mineral Oil for the MiniBooNE Neutrino Detector*, IEEE Nuclear Science Symposium Conference Record (2003).

[95] D. Casper, Nucl. Phys. B (Proc. Suppl.) **112**:161–170, `http://nuint.ps.uci.edu/nuance/` (2002).

[96] [GEANT4 collaboration], S. Agostinelli *et al.*, Nucl. Inst. & Meth. **A 506**:250, `http://wwwasd.web.cern.ch/wwwasd/geant4/G4UsersDocuments/Overview/html/` (2003).

[97] [FINeSSE collaboration] `http://www-finesse.fnal.gov/`.

[98] [MINERνA collaboration] `http://www.pas.rochester.edu/~ksmcf/minerva/`.

[99] [NOνA collaboration] `http://www-nova.fnal.gov/`.

[100] [T2K collaboration] `http://neutrino.kek.jp/jhfnu/`.

[101] [UNO collaboration] `http://ale.physics.sunysb.edu/uno/`.

[102] C. H. Llewellyn Smith, Phys. Rep. **3C**:261–379 (1972).

[103] A. Bodek, I. Park, and U. k. Yang, Nucl. Phys. B (Proc. Suppl.) **139**:113 (2005). [arXiv:hep-ph/0411202]

[104] R. A. Smith and E. J. Moniz, Nucl. Phys. B **43**:605, Erratum-ibid. **B101**:547 (1975) (1972).

[105] R. B. Patterson, private communication (2005).

[106] J. A. Green, private communication (2005).

[107] P. Kasper, `http://www-boone.fnal.gov/software_and_analysis/current_framework/doc/index.html`, for a full description of the SplitEvent algorithm, see the Analysis Framework user manual.

[108] I. Stancu, *Maximum Likelihood Event Reconstruction Algorithms in BooNE*, BooNE Technical Notes 5,6,18,21,36,50 (1998-2002).

[109] F. James and M. Roos, *"MINUIT," A System For Function Minimization and Analysis of the Parameter Errors and Correlations* (1975).

[110] R. Barlow and C. Beeston, Comp. Phys. Comm. **77**:219–228 (1993).

[111] J. Monroe and M. Shaevitz, *Estimating the Uncertainty on the ν_e Background from Intrinsic Beam μ Decay Using the Charged Current Quasi-Elastic Data Set*, MiniBooNE Technical Note 146 (2004).

[112] J. Monroe, D. Finley, T. Kobilarcik, and H.-O. Meyer, *Measuring Protons on Target at MiniBooNE*, MiniBooNE Technical Note 87 (2003).

[113] G. McGregor, *Neutrinos Per Proton on Target*, MiniBooNE Technical Note 136 (2004).

[114] M. O. Wascko, private communication (2005).

[115] J. Monroe, private communication (2005).

Appendix A

Trigger Windows and Holdoffs

This appendix describes the configurations for the various trigger windows in operation at the time of this writing. Tables A.1 and A.2 list the available windows from which event triggers are constructed. Event triggers are shown in Tables A.3 and A.4.

Name	Abbrev.	Definition	Explanation
"Beam holdoff"	BH	$T(E1) \leq 20$	Hold off all other triggers during beam event
"Michel window"	MW	$3 \leq T(DET4 \text{ AND } VETO1) \leq 15$	Look for Michel electrons. A cosmic ray candidate has occurred in a window.
"Laser holdoff"	LH	$T(CALIB\_LASER) \leq 0.2$	No laser event 200 ns prior.
"Supernova holdoff"	SNH	$LH \text{ OR } T(DET4 \text{ OR } VETO1) \leq 15$	A cosmic ray or calibration laser event has occurred in recent past. Holdoff SN triggers.
"Gamma/Beta holdoff"	BNH	$T(DET2 \text{ AND } VETO2) \leq 15$	A cosmic ray has occurred in recent past. Holdoff Gamma and Beta triggers.
"Beam ν candidate"	BNC	$3.6 \leq T(DET2) \leq 8.6$ within Beam event with respect to event origin	A ν candidate in beam window. Use for beta/gamma windows.
"Strobe ν candidate"	SNC	$3.6 \leq T(DET2) \leq 8.6$ within Strobe with respect to event origin	A ν candidate in strobe window. Use for beta/gamma window accidentals.

Table A.1: Trigger windows and holdoffs created using the internal and external trigger bits described in Sec. 3.4 and appropriate logic within the trigger code. T(...) indicates time since this activity in the trigger in μs.

Name	Abbrev.	Definition	Explanation
"Beam gamma window"	BGW	$54 < \mathrm{T(BNC)} \leq 1000$	Gamma after beam ν candidate.
"Beam gamma zero-bias window"	BZBW	$\mathrm{T(BNC)} \leq 54$	Activates zero-bias follower events to follow immediately after beam event with activity in beam timing window (BNC).
"Strobe gamma window"	SGW	$54 \leq \mathrm{T(SNC)} \leq 1000$	Gamma after strobe ν candidate.
"Strobe gamma zero-bias window"	SZBW	$\mathrm{T(SNC)} \leq 54$	Activates zero-bias follower events to follow immediately after strobe event with activity in strobe timing window (SNC).
"Beam beta window"	BBW	$1000 \leq \mathrm{T(BNC)} \leq 30000$	Beta after a beam ν candidate
"Strobe beta window"	SBW	$1000 \leq \mathrm{T(BNC)} \leq 30000$	Beta after strobe ν candidate
"Calibration cube window"	CCW	$0.4 \leq \mathrm{T(CALIB\_CUBE)} \leq 0.8$	Account for time delay between cube trigger (real time) and associated DET/VETO activity (sum PMT takes 6 cycles to compute detector sum.

Table A.2: More trigger windows and holdoffs created using the internal and external trigger bits described in Sec. 3.4 and appropriate logic within the trigger code. T(...) indicates time since this activity in the trigger in μs.

Trigger Name	Logical Conditions	#TSAs	Explanation
beam	!BH && E1	192	Neutrino beam on target signal.
strobe	!BH && STROBE	192	Arrives 5μs before beam on target.
		192	Pulser signal
Michel	!BH && MW && !VETO1 && DET2	192	Electrons from muon decay.
			TSA window large enough to contain parent muon.
Supernova	!BH && !SNH && !VETO1 && DET5	32	Supernova candidate
tank	!BH && DET1	192	Minimum bias tank PMT trigger.
veto	!BH && VETO1	192	Minimum bias vet PMT trigger.
calibration: laser	!BH && CALIB_LASER	96	Laser event
calibration: laser	!BH && CALIB_BEAM	96	Laser in time with non-MiniBooNE
beam			Booster shot.
calibration: cube	!BH && CCW && DET4	128	Cube in time with DET4 tank hits.
calibration: tracker	!BH && CALIB_TRACKER	128	Muon tracker 4-plane coincidence (+ cube). See Table 3.5.

Table A.3: Event triggers listed in order of precedence.

Trigger Name	Logical Conditions	#TSAs	Explanation
beam gamma	!GBH && BGW && DET1 && !DET4 && !VETO2	32	Gamma candidate following beam ν candidate
beam beta	!GBH && BBW && DET2 && !VETO2	32	Beta candidate following beam ν candidate
strobe gamma	!GBH && SGW && DET1 && !DET4 && !VETO2	32	Gamma candidate following strobe ν candidate
strobe beta	!GBH && SBW && DET2 && !VETO2	32	Beta candidate following strobe ν candidate
big nu	!LH && DET3 && !VETO1	192	Tank hits> 200, no veto, no laser, no beam. Used for debuncher events, high-energy ν's from environment, and veto efficiency.
beam gamma zero-bias	BZBW && FOLLOWER	192	Immediately follows beam event in time. Configurable number of events produced for every beam event containing activity in the ν candidate window.
strobe gamma zero-bias	SZBW && FOLLOWER	192	Immediately follows strobe event in time. Configurable number of events produced for every strobe event containing activity in the ν candidate window. Used for measuring backgrounds.

Table A.4: More event triggers listed in order of precedence.

Appendix B

Oil Tests with the 1.6 Meter "Cincinnati Tester"

B.1 Attenuation Test Setup

The 1.6 meter oil attenuation test setup consists of a monochromator with deuterium light source, two EMI 9813 photomultiplier tubes (PMTs), two lenses, and a light-tight box containing an oil sample tube. A schematic diagram of the setup is shown in figure B.1. The monochromator selects light of a particular wavelength and directs it to an optics box where the beam is split by a borosilicate glass window. Approximately 10 percent of the light is directed to PMT2, the reference PMT, while the other 90 percent is directed toward the oil sample and PMT1. The oil sample is held in a 160 cm long cylindrical lucite tube with borosilicate glass ends. This sample tube is placed in a light-tight box.
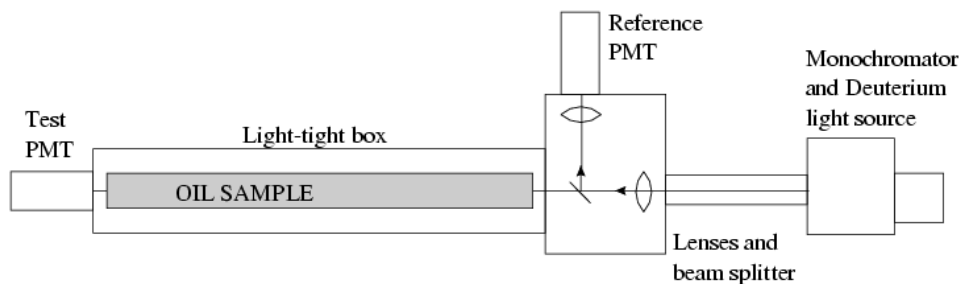

Figure B.1: A schematic diagram of the 1.6 meter oil attenuation tester.

The outputs of the photomultiplier tubes are fed into a LeCroy Model 612 amplifier, followed

by a LeCroy 821 discriminator, and finally to a LeCroy 2551 scaler. The data are read to a PC via CAMAC. Data consist of recorded scaler counts for PMT1 and PMT2 wavelengths covering the range from 3000 to 5000 Angstroms in steps of 10 Angstroms.

The testing procedure is detailed as follows. The lucite sample tube is filled with an oil and allowed to rest overnight in the light-tight box to allow any contaminants in the oil to settle. After the oil has settled, 3 or 4 consecutive runs of that oil are taken without turning off the high voltage or the deuterium lamp. The high voltage is then turned off so that the oil may be emptied from the sample tube; the tube is then returned to the light-tight box for an "empty tube" run. Finally, a run with no tube in the box is taken. Using this procedure, 3 or 4 runs with oil, 1 run with an empty sample tube, and 1 run with no sample tube are obtained on each day of testing.

Data from these runs are plotted as the ratio of light transmitted through the oil sample to the light in the reference beam versus the wavelength. This ratio is divided by the same ratio for a run taken with no oil sample in the light-tight box. For runs taken with an empty sample tube, we expect to see at most only 82 percent of the light transmitted to PMT1 due to the four glass interfaces through which the light must travel (the two faces of each borosilicate glass end on the sample tube). The percentage of light transmitted through the sample tube when it contains oil should be no more than 91 percent, due to two interfaces it must traverse.

A composite drawing of all oils measured during the selection process is shown in Fig. B.2. The oil chosen for the MiniBooNE detector is Marcol 7, denoted by the dark grey dashed line on the plot.
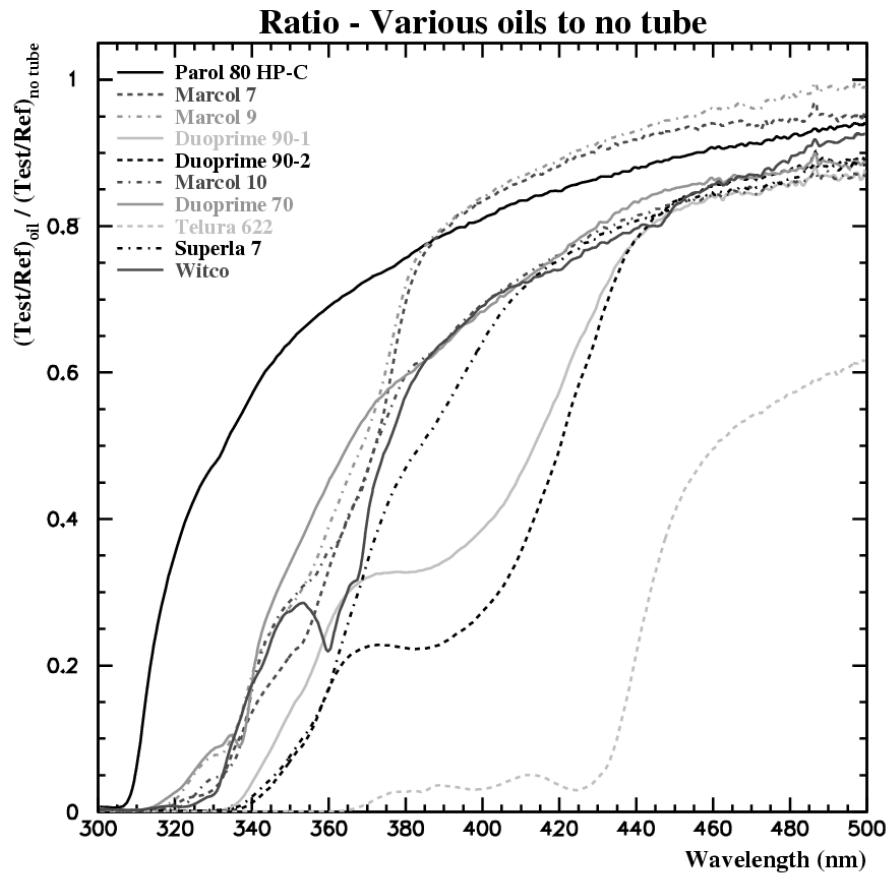
Figure B.2: A relative measure of light transmitted through the 1.6 m tester for various mineral oils.

Appendix C

Coherent π^0 Production and Anti-neutrinos

C.1 Parity Conservation in Coherent π^0 Production

One interesting consequence of the fact that parity is effectively conserved in coherent π^0 production is that the cross section for neutrinos is the same as that for anti-neutrinos. This is not the case for resonant production, where the anti-neutrino cross section is approximately half the neutrino cross section. Because of this, there are interesting measurements that can be made with experiments that can run with both neutrinos and anti-neutrinos.

Theoretical models for coherent π^0 production at low neutrino energy can vary by up to an order of magnitude in their predictions [36–40]. A better experimental constraint can be placed on coherent production relative to resonant production by studying both neutrino and anti-neutrino events. Since the resonant π^0 cross section is suppressed for anti-neutrinos, but the coherent π^0 cross section stays the same, the relative amount of coherent production is effectively enhanced for anti-neutrinos. This is demonstrated in Fig. C.1, where the absolutely normalized π^0 angular distributions of resonant and coherent π^0's are plotted for neutrinos (top) and anti-neutrinos (bottom). In neutrino-scattering mode, it is clear that although the coherent π^0's are more forward-peaked, the *number* of coherent π^0's is overwhelmed by the number of resonant π^0's. This is not the case in anti-neutrino-scattering mode, where the ratio of resonant to coherent π^0's is much smaller,

allowing the coherent π^0 angular distribution to present itself far more dramatically. Experiments that are able to run in both neutrino and anti-neutrino mode can (and should!) take advantage of this difference to make a better measurement of the coherent π^0 cross section.
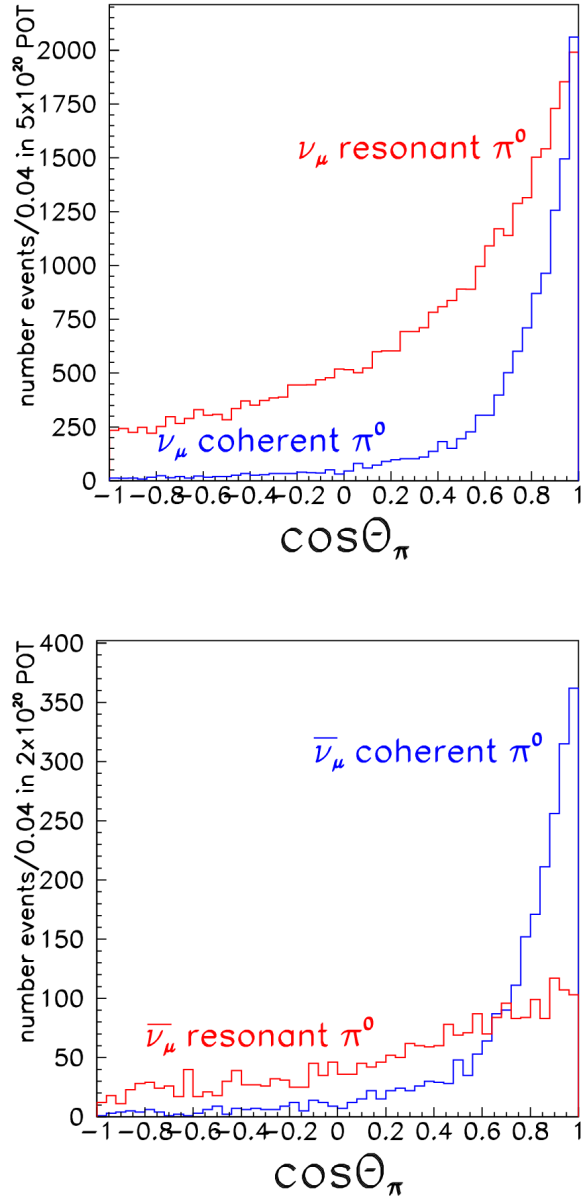

Figure C.1: Generated π^0 angular distributions for NC ν and $\bar{\nu}$ π^0 production.

Appendix D

Nuance Event Generator Interactions

Code	CC / NC	Reaction	Category
1	CC	$\overset{(-)}{\nu}_\mu\, n \to \mu^{-(+)}p$	CCQE
2	NC	$\overset{(-)}{\nu}_\mu\, n \to \overset{(-)}{\nu}_\mu\, n$ $\overset{(-)}{\nu}_\mu\, p \to \overset{(-)}{\nu}_\mu\, p$	NC Elastic
3	CC	$\nu_\mu p \to \mu^- p\pi^+$	Resonant Single π
4	CC	$\nu_\mu n \to \mu^- p\pi^0$	Resonant Single π
5	CC	$\nu_\mu n \to \mu^- n\pi^0$	Resonant Single π
6	NC	$\nu_\mu p \to \nu_\mu p\pi^0$	Resonant Single π
7	NC	$\nu_\mu p \to \nu_\mu n\pi^+$	Resonant Single π
8	NC	$\nu_\mu n \to \nu_\mu n\pi^0$	Resonant Single π
9	NC	$\nu_\mu n \to \nu_\mu p\pi^-$	Resonant Single π
10 — 16		Corresponding $\bar{\nu}_\mu$ processes	
17	CC	$\nu_\mu p \to \mu^- \Delta^+\pi^+$	Resonant Multiple π (Δ)
18	CC	$\nu_\mu p \to \mu^- \Delta^{++}\pi^0$	Resonant Multiple π (Δ)
19	CC	$\nu_\mu n \to \mu^- \Delta^+\pi^0$	Resonant Multiple π (Δ)
20	CC	$\nu_\mu n \to \mu^- \Delta^0\pi^+$	Resonant Multiple π (Δ)

Code	CC / NC	Reaction	Category
21	CC	$\nu_\mu n \to \mu^- \Delta^{++} \pi^-$	Resonant Multiple π (Δ)
22	NC	$\nu_\mu p \to \mu^- \Delta^+ \pi^0$	Resonant Multiple π (Δ)
23	NC	$\nu_\mu p \to \nu_\mu \Delta^0 \pi^+$	Resonant Multiple π (Δ)
24	NC	$\nu_\mu p \to \nu_\mu \Delta^{++} \pi^-$	Resonant Multiple π (Δ)
25	NC	$\nu_\mu n \to \nu_\mu \Delta^+ \pi^-$	Resonant Multiple π (Δ)
26	NC	$\nu_\mu n \to \nu_\mu \Delta^0 \pi^0$	Resonant Multiple π (Δ)
27 — 38		Corresponding $\bar{\nu}_\mu$ processes	
39	CC	$\nu_\mu p \to \mu^- p \rho^+$	Resonant Multiple π (ρ)
40	CC	$\nu_\mu n \to \mu^- p \rho^0$	Resonant Multiple π (ρ)
41	CC	$\nu_\mu n \to \mu^- n \rho^+$	Resonant Multiple π (ρ)
42	NC	$\nu_\mu p \to \nu_\mu p \rho^0$	Resonant Multiple π (ρ)
43	NC	$\nu_\mu p \to \nu_\mu n \rho^+$	Resonant Multiple π (ρ)
44	NC	$\nu_\mu n \to \nu_\mu n \rho^0$	Resonant Multiple π (ρ)
45	NC	$\nu_\mu n \to \nu_\mu p \rho^-$	Resonant Multiple π (ρ)
46 — 52		Corresponding $\bar{\nu}_\mu$ processes	
53	CC	$\nu_\mu p \to \mu^- \Sigma^+ K^+$	Resonant Multiple π (ΣK)
54	CC	$\nu_\mu n \to \mu^- \Sigma^0 K^+$	Resonant Multiple π (ΣK)
55	CC	$\nu_\mu n \to \mu^- \Sigma^+ K^0$	Resonant Multiple π (ΣK)
56	NC	$\nu_\mu p \to \nu_\mu \Sigma^0 K^+$	Resonant Multiple π (ΣK)
57	NC	$\nu_\mu p \to \nu_\mu \Sigma^+ K^0$	Resonant Multiple π (ΣK)
58	NC	$\nu_\mu n \to \nu_\mu \Sigma^0 K^0$	Resonant Multiple π (ΣK)
59	NC	$\nu_\mu n \to \nu_\mu \Sigma^- K^+$	Resonant Multiple π (ΣK)
60 — 66		Corresponding $\bar{\nu}_\mu$ processes	
67	CC	$\nu_\mu n \to \mu^- p \eta$	Resonant Multiple π (η)
68	NC	$\nu_\mu p \to \nu_\mu p \eta$	Resonant Multiple π (η)
69	NC	$\nu_\mu n \to \nu_\mu n \eta$	Resonant Multiple π (η)

continued on next page

Code	CC / NC	Reaction	Category
70 — 72		Corresponding $\bar{\nu}_\mu$ processes	
73	CC	$\nu_\mu n \to \mu^- K^+ \Lambda$	Resonant Multiple π (ΛK)
74	NC	$\nu_\mu n \to \nu_\mu K^+ \Lambda$	Resonant Multiple π (ΛK)
75	NC	$\nu_\mu n \to \nu_\mu K^0 \Lambda$	Resonant Multiple π (ΛK)
76 — 78		Corresponding $\bar{\nu}_\mu$ processes	
79	CC	$\nu_\mu n \to \mu^- p \pi^+ \pi^-$	Resonant Multiple π $(\pi\pi)$
80	CC	$\nu_\mu n \to \mu^- p \pi^0 \pi^0$	Resonant Multiple π $(\pi\pi)$
81	NC	$\nu_\mu p \to \nu_\mu p \pi^+ \pi^-$	Resonant Multiple π $(\pi\pi)$
82	NC	$\nu_\mu p \to \nu_\mu p \pi^0 \pi^0$	Resonant Multiple π $(\pi\pi)$
83	NC	$\nu_\mu n \to \nu_\mu n \pi^+ \pi^-$	Resonant Multiple π $(\pi\pi)$
84	NC	$\nu_\mu n \to \nu_\mu n \pi^0 \pi^0$	Resonant Multiple π $(\pi\pi)$
85 — 90		Corresponding $\bar{\nu}_\mu$ processes	
91	CC	$\nu_\mu \mathcal{N} \to \mu^- X$	Deep Inelastic Scattering
92	NC	$\nu_\mu \mathcal{N} \to \nu_\mu X$	Deep Inelastic Scattering
93 — 94		Unused	
95	CC	$\bar{\nu}_\mu p \to \mu^+ \Lambda$ $\bar{\nu}_\mu n \to \mu^+ \Sigma^-$ $\bar{\nu}_\mu p \to \mu^+ \Sigma^0$	Cabibbo-suppressed QE hyperon production
96	NC	$\overset{(-)}{\nu}_\mu \mathcal{A} \to \overset{(-)}{\nu}_\mu \mathcal{A} \pi^0$	Coherent/diffractive π
97	CC	$\overset{(-)}{\nu}_\mu \mathcal{A} \to \mu^{-(+)} \mathcal{A} \pi^{+(-)}$	Coherent/diffractive π
98	NC	$\overset{(-)}{\nu}_\mu e \to \overset{(-)}{\nu}_\mu e$	$\nu - e$ Elastic Scattering
99	CC	$\nu_\mu e \to \mu^- e$	$\nu - e$ Inverse μ Decay

Table D.1: `Nuance` reaction codes.